Projecte de Fi de Carrera

Enginyer Industrial

Transferències des de la Terra a Órbites de Libració usant Impuls Feble amb Restricció en la Direcció de Propulsió

MEMÒRIA

Autor : **Pedro Fernando Di Donato**

Director : **Josep J. Masdemont**

Convocatòria : **Juny 2006**

Escola Tècnica Superior

d'Enginyeria Industrial de Barcelona

Resum

Degut a les seves característiques úniques, les òrbites de libració han rebut molta atenció en els darrers 25 anys. Actualment, els entorns dels punts de Lagrange 1 i 2 tenen molta importància per a uns certs tipus de missions espacials científiques. De fa uns anys, l'estudi i disseny d'aquest tipus de missions s'ha basat en la Teoria de Sistemes Dinàmics com a alternativa als mètodes clàssics d'optimització de transferències. La utilització de varietats invariants ha obert grans possibilitats, no només pel disseny de transferències més eficients, sinó també per a una millor comprensió de tot el problema en general.

D'altra banda, l'increment de càrregues útils ha motivat la recerca en nous mètodes de propulsió incidint sobretot en la seva eficiència. Entre aquestes idees, l'impuls feble elèctric produït per energia solar es presenta com una de les tecnologies amb més promesa de ser usades en un futur proper.

Per tot aixo, l'objectiu principal d'aquest projecte ha estat un primer estudi de les transferències, des d'òrbites baixes al voltant de la Terra, a òrbites de libració tipus halo combinant impuls feble y la Teoria dels Sistemes Dinàmics. Per això s'ha considerat l'us de les varietats estables de possibles òrbites objectiu i s'han considerat com a transfers interessants els que comencen amb órbites de parking d'excentricitat i inclinació petites.

En el projecte ens restringim a l'estudi de les òrbites halo als entorns dels punts de libració 1 i 2 del sistema Sol-Terra/Lluna. La magnitud de l'impuls s'ha considerat constant des del moment de la sortida de l'òrbita de parking fins la trobada del satel.lit amb la varietat estable. A més, la direcció de l'impuls s'ha restringit a la que proporciona un augment més gran del semieix major de l'òrbita.

L'estudi s'ha dut a terme usant una sèrie de models de complexitat creixent començcant per un problema restringit circular. A partir del problema restringit s'han trobat un conjunt de paràmetres que defineixen transferències interessants. Seguidament s'ha modificat el problema restringit, incorporant-hi les principals pertorbacions al potencial Newtonià quan ens trobem propers a la Terra, a fi de veure l'impacte que poden tenir aquestes en les òrbites que s'han trobat inicialment.

En el darrer pas usem el model basat en les efemèrides JPL, incloent la influencia de tots els cossos principals del Sistema Solar així com les pertorbacions més importants al voltant de la Terra. Amb aquest model s'aconsegueixen obtenir trajectòries de transferència precises que podríen ser emprades en missions reals.

Abstract

Due to their unique characteristics, the libration points have been receiving much attention in the last 25 years. Nowadays, the Lagrange relative positions known as point 1 and 2 of the Sun-Earth and Earth-Moon system present the most practical applications for astronomical and lunar related observatories. The study and design of missions related to them is usually based in the Dynamical Systems Theory which allows a alternative approach to the optimum transfer method. The use of invariant manifolds opens great possibilities not only to the design of more efficient transfers, but also to the better general understanding of the problem.

By other hand, the increasing weight of payloads has encouraged the search for new propulsion methods, aiming in more efficiency. Between the new ideas, the use of solar electric low thrust thruster has been employed with success and figures as one of the most promising technologies to be widely used in the near future.

Considering this, the main objective of this project was the determination and study of transfers from low Earth orbits to others around the libration points by mean of low thrust and using the Dynamic System theory, and, in particular, the stable manifolds associated to the target orbits. The interesting transfers were the ones that start in low eccentricity and low inclination parking orbits.

In this project we restrict our study to the halo orbits around the libration points 1 and 2 of the Sun-Earth/Moon system. The thrust magnitude was considered constant from the starting orbit till the link with the manifold. Moreover, its direction was constrained for the one which provides the greater increase in the semi-major axis of the orbit.

The study was conducted with a series of increasing complexity models. Starting from the simple circular restricted three body problem. We found several set of parameters that define interesting transfers. The next step was the development of model for the near Earth perturbation forces that was integrated to the previous model. This new model was used to test the previously found interesting orbits and the impact of the perturbations on them could be determined.

Finally the last step was using the results in a model based in the JPL Ephemerides model, taken into account all the main bodies of the solar system with the near Earth perturbations integrated to it. With this model we could determine precisely transfers that could be applied in real missions.

Contents

1 Introduction

As a natural step of the advance of the human explorations, the limits of low-Earth and geostationary orbits are being exceeded. The libration points, in special, are one of the most promising candidates of being part of future missions, receiving great attention in the lasts 25 years [4].

They are defined as the equilibrium points of the Restricted Three Body Problem, which models, in a synodical frame, the behavior of a particle of very small mass under the influence of two other massive bodies (*primaries*). There are five libration points. Two of them, which are located collinearly, in a synodical frame, with the primaries have been receiving most attention since they generate and control many trajectories with interesting applications to space missions [4].

The study of orbits around the librations points was greatly improved with the use of the Dynamical System Theory, in special, the determination of invariant manifolds. Essentially they are sets of orbits which moves from and towards the libration points orbits, providing a fast and cheap way of transfer spacecraft from a vicinity of the Earth to the libration points.

The use of the invariant manifolds until now was restricted to impulsive missions, i.e, using a high-thrust chemical propulsion system, the spacecraft is inserted in the manifold in a quick maneuver. The future missions, moreover, tend to involve increasing cargos which requires new forms of propulsion, since the use of this kind of propulsion system is limited by its low efficiency.

The alternative is the use of low-thrust propulsion systems which are based in the idea of applying thrust of very small magnitude for long time periods. The main consequence is a long time but efficient maneuver allowing large payloads to be delivered to deep space regions.

Nevertheless, since the low thrust thrusters cannot provide enough thrust to place a spacecraft on an Earth orbit, missions which apply them always have as a starting point a previous orbit reached by a typical chemical launcher [18]. Technical and commercial constrains of the existing launch vehicles, allied with the main satellites applications, led to the great majority of used orbits to be near-circular with altitudes between 300 and 1500km, which are commonly named as *Low-Earth Orbits* (LEO) [15].

The objective of this project was, therefore, to find and study low-thrust trajectories from low-Earth to libration point orbits. This was accomplished by the use of the invariant manifolds obtained by the method proposed by Masdemont [13], being the project itself an application of these results.

2 The Restricted Three-Body Problem and the Libration Points

The first step when attacking a problem of dynamics is to choose a model of the system to work with. Modeling can be a very difficult task since, in the ”real world”, there are always several forces acting in every system. Most of them can be neglected since their contribution to the system behavior is very small. However, the option to include/exclude one of them in the development of a model is always a difficult choice.

One of the simplest models that can represent the dynamics of spacecrafts located far from the Earth, more precisely near the libration points, is the *restricted three-body problem*.

The first part of this work was developed entirely based on this model. However, since there are several modifications and nomenclature in literature to describe it, a better description of the model used in this work would be: *the three-dimensional circular restricted three-body problem*. Only this type was used in the work, thus the simple symbol CRTBP will be used when refering to it, without risk of misunderstanding.

A complete development of the system equations together with a small historical review is presented in appendix B, which also provides the references used in the deduction.

The main objective of this section is to present the CRTBP equations, the libration points and its invariant manifolds characteristics and applications in future space missions.

2.1 Statement of the Problem and Equations of the Motion

As cited in the section 1, the CRTBP basically models the motion of a particle with a very small mass under the influence of the newtonian gravitational force exerted by two other massive mass, named primaries, which are considered to be revolving circular orbits around their center of mass.

The term *restricted* in the name of the model is due to the assumption that the particle mass is small enough to influence the motion of the primaries. This hypothesis is really true if the particle mass is exactly zero, but is crucial to make the study of the system behavior possible. Moreover, since todays spacecrafts masses are really insignificant if compared to celestial bodies mass as the Earth and the Sun, there are more applications of the CRTBP than to the three-body problem.

Some modifications of the restricted three-body problem assumes elliptic motion of the primaries. This is the reason for the use of the *circular* term in the model's name.

The equations of the motion of the CRTBP in dimensionless coordinates can be expressed by (equation B.12, reference [15])

$$\begin{aligned} \ddot{x} - 2\dot{y} &= \frac{\partial \Omega}{\partial x} \\ \ddot{y} + 2\dot{x} &= \frac{\partial \Omega}{\partial y} \\ \ddot{z} &= \frac{\partial \Omega}{\partial z} \end{aligned} \tag{2.1}$$

where Ω is given by (equation B.14)

$$\Omega\left(x, y, z\right) = \frac{1}{2}\left(x^2 + y^2\right) + \frac{1-\mu}{r_1} + \frac{\mu}{r_2} + \frac{1}{2}\mu(1-\mu) \tag{2.2}$$

and r_1 and r_2 by (equation B.15)

$$\begin{aligned} r_1^2 &= \left(x-\mu\right)^2 + y^2 + z^2 \\ r_2^2 &= \left(x-\mu+1\right)^2 + y^2 + z^2 \end{aligned} \tag{2.3}$$

The parameter μ is called the mass parameter of the CRTBP and is defined by (equation B.11)

$$\mu = \frac{m_2}{M} = \frac{m_2}{m_1 + m_2} \tag{2.4}$$

where m_1 and m_2 are the masses of the big and the small primaries respectively.

The coordinates x, y and z are with respect to the synodic coordinate system, which has the origin in the primaries center of mass and the $x-y$ fundamental plane equal to the primaries plane of motion. Moreover, it rotates with the primaries, having them always aligned in the x-axis.

2.2 Libration Points and Applications

The Lagrange libration points are the equilibrium solutions of the set of equations 2.1. Their position is known since the studies of Euler and Lagrange [4] in the late 1700s.

The equations 2.1, at the points of *singularity of the manifold* of the equations of the motion, give $\ddot{x} = \ddot{y} = \ddot{z} = 0$ for which reason this points are also called *equilibrium points*. It can be proved that all derivatives with respect to time are zero at this points [15]. Therefore, if the

third particle is placed at an equilibrium point with zero velocity it will stay there forever. This consequence is responsible for other names for this points: *stationary points*, *Lagrangian points* and *libration points*.

Then, as it has been said, one way to obtain the libration points is solving the system of equations (see [15])

$$\begin{array}{lll} \dot{x} = 0, & \dot{y} = 0, & \dot{z} = 0, \\ \dfrac{\partial \Omega}{\partial x} = 0, & \dfrac{\partial \Omega}{\partial y} = 0, & \dfrac{\partial \Omega}{\partial z} = 0. \end{array} \tag{2.5}$$

The last one can be expanded as

$$\frac{\partial \Omega}{\partial z} = -z \left(\frac{1-\mu}{r_1^3} + \frac{\mu}{r_2^3} \right) = 0 \tag{2.6}$$

where the second factor is positive for all finite values of r_1 and r_2. Therefore, the equilibrium points are all located at the fundamental plane, the plane of the motion of the primaries.

The other two equations involving Ω in expanded form become

$$x - \frac{(1-\mu)(x-\mu)}{r_1^3} - \frac{\mu(x+1-\mu)}{r_2^3} = 0 \tag{2.7}$$

$$y \left(1 - \frac{1-\mu}{r_1^3} - \frac{\mu}{r_2^3} \right) = 0 \tag{2.8}$$

The solution of these two equations results in five points. Two of them are given by $r_1 = r_2 = 1$ which results in the points $x = \mu - \frac{1}{2}$ and $y = \pm \frac{\sqrt{3}}{2}$. This solution is an arrangement of an equilateral triangle with the three bodies located at its vertices and rotating around the primaries center of mass. Traditionally the plus sign correspond to the libration point L_4 and the minus with the L_5, both are usually called triangular or equilateral solutions.

The other three points are located on the x axis, corresponding to arrangements in which the three bodies are aligned. The computation of their location is done by replacing $y = 0$ and $z = 0$ in equation 2.7 and solving the resulting quintic polynomial equation numerically. The location of the points with respect to the primaries, however, is always the same: one between both of them (L_1), one behind the small primary (L_2) and other behind the big one (L_3). Figure 2.1 presents an example of the five libration points in the synodic reference frame.

In the Sun-Earth/Moon system, where the small primary (also called *secondary*) is the Earth-Moon system, the value of μ is tabled in appendix D. Table 2.1 present the position of the libration points and their distance from the Earth in kilometers calculated using this value.

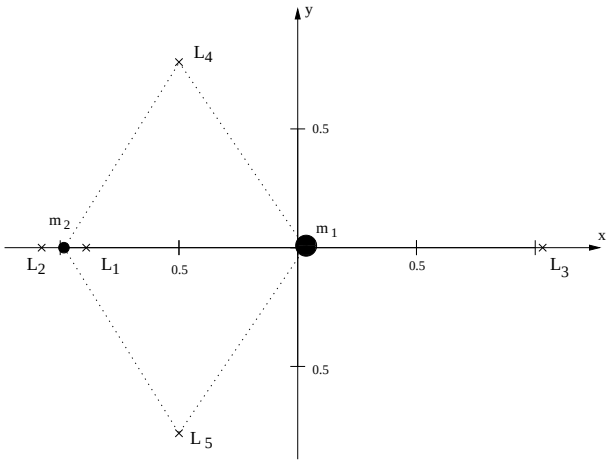

Figure 2.1: The Lagrangian points position in the usual CRTBP synodic reference system

Table 2.1: Coordinates of the libration points in the Sun-Earth/Moon system

Point	Coord. Synodic System		Distance from
	X [CRTBP units]	Y [CRTBP units]	Earth [millions of km]
L_1	-0.989985982	0.000000000	1.5077
L_2	-1.010075200	0.000000000	1.4976
L_3	+1.000001267	0.000000000	299.1957
L_4	-0.499999696	+0.866025404	149.5979
L_5	-0.499999696	-0.866025404	149.5979

2.3 Libration Point Orbits and Invariant Manifolds

Much study has been applied in understanding the dynamics around the collinear libration points (L_1, L_2 and L_3). The main goal is to give a global description of of the different kind of possible solutions.

In a first approximation, the motion around the vicinity of a libration point can be seen as the composition of two oscillators and some hyperbolic behavior. This means that the oscillations are not stable and that small deviations from the in the orbit will be amplified as time increases.

One of the oscillations takes place in the plane of the motion of the primaries while the other is orthogonal to this plane. When only one oscillation is present (the amplitude of the other is zero) the resulting orbits are named *planar and vertical Lyapunov orbits*. Lyapunov orbits are periodic. Moreover, the dynamics of three Lyapunov orbits bound the dynamics of other libration point orbits contained in the region.

Since the dynamics is non-linear, both frequencies of oscillation vary with their amplitudes.

Considering a fixed Jacobi constant (see appendix B), for one specific amplitude both frequencies are equal, and the resulting periodic orbit is called *Halo orbit*. Figure 2.2 illustrates the positions of the Halo orbits with respect to the Earth and the Sun.

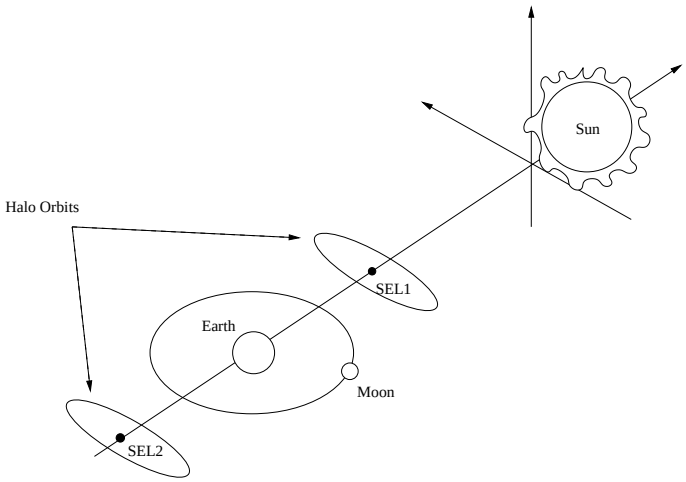

Figure 2.2: Halo orbit positions with respect to the Earth and the Sun

In the case that both frequencies distinguished we have a Lissajours orbit. For the particular case of the frequencies being commensurable[1], the resulting motion is periodic.

Invariant manifolds are surfaces in the trajectory design space consisting of global families of trajectories that wind on and off periodic orbits as halo orbits [4]. If the orbits of an invariant manifold tend to a periodic orbit when times increases, this manifold is named *stable*, otherwise, if the orbits tend to periodic one when time decreases it is named *unstable*. Figure 2.3 presents an example of the three projections of a halo orbit around SEL1 and its stable manifolds.

This means that once a spacecraft is set on a stable manifold, it will exhibits exponential approach to the target periodic orbit. Otherwise, if it is placed on an unstable one, it would departure from the origin orbit exponentially as well. Therefore, the invariant manifolds represent a fast and cheap way to transfer a spacecraft from the vicinity of the Earth to a libration point orbit and vice versa (see [8]). Moreover, it permits low-cost transfers throughout the solar system and played an important role in its evolution [4].

The use of invariant manifolds in trajectory design is one of the bases of this work. The detailed explanation of how it was done, however, is let to section 4.

[1] Two real numbers a and b are commensurable if, and only if, the ratio a/b is a rational number

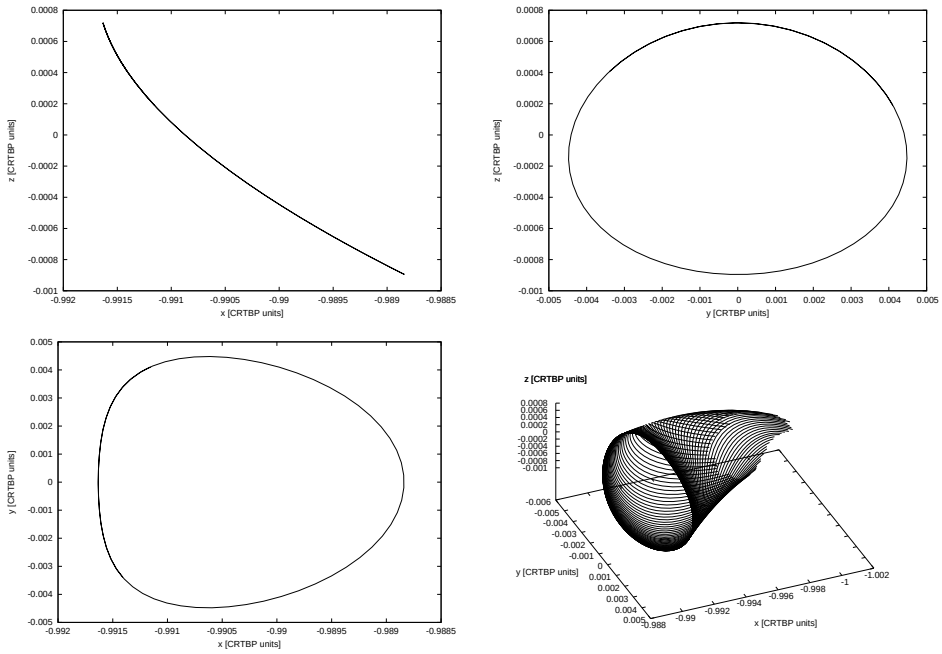

Figure 2.3: Projections of a SEL1 Halo orbit and its stable manifolds

2.4 Determination of the Invariant Manifold

In order to use an invariant manifold to do the trajectory design, as it was done in this project, the first step is determine this manifold. This was done using the method developed by Masdemont presented in reference [13].

Details of the method are beyond the focus of this project. Therefore, the objective of this subsection is just explain the basic idea necessary to a understanding of the studies done in this project.

If the linear part of the equations of the motion are separated in the left side, and the Legendre polynomials, $P_n(t) = \frac{1}{2^n n!}\frac{d^n}{dt^n}\left[\left(t^2-1\right)^n\right]$ are used to expand the inverse of r_1 and r_2, the CRTBP equations 2.1 about a collinear libration point can be rewritten as

$$\begin{aligned} \ddot{x} - 2\dot{y} - (1-2c_2)x &= \frac{\partial}{\partial x}\sum_{n\geq 3} c_n \rho^n P_n\left(\frac{x}{\rho}\right) \\ \ddot{y} + 2\dot{x} + (c_2-1)y &= \frac{\partial}{\partial y}\sum_{n\geq 3} c_n \rho^n P_n\left(\frac{x}{\rho}\right) \\ \ddot{x} - 2\dot{y} + c_2 z &= \frac{\partial}{\partial z}\sum_{n\geq 3} c_n \rho^n P_n\left(\frac{x}{\rho}\right) \end{aligned} \tag{2.9}$$

where $\rho^2 = x^2 + y^2 + z^2$, and c_n are constants that depend only on the model and the selected

equilibrium point.

The general solution of the linear part can be expressed by

$$\begin{aligned} x(t) &= \alpha_1 e^{\lambda_0 t} + \alpha_2 e^{-\lambda_0 t} + \alpha_3 \cos(\omega_0 t + \phi_1) \\ y(t) &= \bar{k}_2 \alpha_1 e^{\lambda_0 t} + \bar{k}_2 \alpha_2 e^{-\lambda_0 t} + \bar{k}_1 \alpha_3 \sin(\omega_0 t + \phi_1) \\ z(t) &= \alpha_4 \cos(\nu_0 t + \phi_2) \end{aligned} \tag{2.10}$$

where α_i and ϕ_i are arbitrated values (amplitudes and phases) and $\bar{k}_i$, ω_0, λ_0 and ν_0 are positive constants depending on c_2 only.

In this set of equations it is easy to observe the characteristics of the behavior near the libration points explained before. The values of α_3, α_4, ϕ_1 and ϕ_2 are the amplitudes and phases of the in-plane and out-of-plane oscillations respectively. Taking $\alpha_1 = 0$ and $\alpha_2 \neq 0$ we have orbits that tends to Lissajous orbits when time increases, i.e., orbits in the stable manifold. Doing the opposite, i.e, taking $\alpha_1 \neq 0$ and $\alpha_2 = 0$ the resulting orbits tend to the Lissajous orbits when time decreases and are part of the unstable manifold.

In order to keep the meaning of all the α amplitudes, a Lindstedt-Poincaré expansion is used to express the global solution including the nonlinear terms

$$\begin{aligned} x(t) &= \sum e^{(i-j)\theta_3} \left[x_{ijkm}^{pq} \cos(p\theta_1 + q\theta_2) + \bar{x}_{ijkm}^{pq} \sin(p\theta_1 + q\theta_2) \right] \alpha_1^i \alpha_2^j \alpha_3^k \alpha_4^m \\ y(t) &= \sum e^{(i-j)\theta_3} \left[y_{ijkm}^{pq} \cos(p\theta_1 + q\theta_2) + \bar{y}_{ijkm}^{pq} \sin(p\theta_1 + q\theta_2) \right] \alpha_1^i \alpha_2^j \alpha_3^k \alpha_4^m \qquad (2.11) \\ z(t) &= \sum e^{(i-j)\theta_3} \left[z_{ijkm}^{pq} \cos(p\theta_1 + q\theta_2) + \bar{z}_{ijkm}^{pq} \sin(p\theta_1 + q\theta_2) \right] \alpha_1^i \alpha_2^j \alpha_3^k \alpha_4^m \end{aligned}$$

(2.12)

with

$$\theta_1 = \omega t + \phi_1 \qquad \theta_2 = \nu t + \phi_2 \qquad \theta_3 = \lambda t \tag{2.13}$$

$$\omega = \sum \omega_{ijkm} \alpha_1^i \alpha_2^j \alpha_3^k \alpha_4^m \qquad \nu = \sum \nu_{ijkm} \alpha_1^i \alpha_2^j \alpha_3^k \alpha_4^m \qquad \lambda = \sum \lambda_{ijkm} \alpha_1^i \alpha_2^j \alpha_3^k \alpha_4^m \tag{2.14}$$

Therefore, the values of the pairs $\left(x_{ijkm}^{pq}, \bar{x}_{ijkm}^{pq}\right)$, $\left(z_{ijkm}^{pq}, \bar{z}_{ijkm}^{pq}\right)$ and $\left(z_{ijkm}^{pq}, \bar{z}_{ijkm}^{pq}\right)$ and of the coefficients ω_{ijkm}, ν_{ijkm} and λ_{ijkm} must be determined. This is done following the method presented in reference [13].

In the case of halo orbits, the initial approximation taken is modified to

$$\begin{aligned} x(t) &= \alpha_1 e^{\lambda_0 t} + \alpha_2 e^{-\lambda_0 t} + \alpha_3 \cos(\omega_0 t + \phi_1) \\ y(t) &= \bar{k}_2 \alpha_1 e^{\lambda_0 t} + \bar{k}_2 \alpha_2 e^{-\lambda_0 t} + \bar{k}_1 \alpha_3 \sin(\omega_0 t + \phi_1) \\ z(t) &= \alpha_4 \cos(\omega_0 t + \phi_2) \end{aligned} \tag{2.15}$$

where it can be noted that the in-plane and out-of-plane frequencies are equal. This, however, is not a solution of the linear part of equations 2.9. Due to that, we add the residual in the right-hand side of this equations adding the term Δz where $\Delta = c_2 - \omega_0^2$.

The expansions take the form

$$\begin{aligned} x(t) &= \sum e^{(i-j)\theta_3} \left[x^p_{ijkm} \cos(p\theta_1) + \bar{x}^p_{ijkm} \sin(p\theta_1) \right] \alpha_1^i \alpha_2^j \alpha_3^k \alpha_4^m \\ y(t) &= \sum e^{(i-j)\theta_3} \left[y^p_{ijkm} \cos(p\theta_1) + \bar{y}^p_{ijkm} \sin(p\theta_1) \right] \alpha_1^i \alpha_2^j \alpha_3^k \alpha_4^m \qquad (2.16) \\ z(t) &= \sum e^{(i-j)\theta_3} \left[z^p_{ijkm} \cos(p\theta_1) + \bar{z}^p_{ijkm} \sin(p\theta_1) \right] \alpha_1^i \alpha_2^j \alpha_3^k \alpha_4^m \end{aligned}$$

(2.17)

where θ_1, θ_3, ω, λ are defined as in equations 2.13, and $\Delta = \sum d_{ijkm} \alpha_1^i \alpha_2^j \alpha_3^k \alpha_4^m$.

In order to make this expansion be a solution of the set of motion equations, we further impose that $\Delta(\alpha_1^i \alpha_2^j \alpha_3^k \alpha_4^m) = 0$. Therefore, given the values of α_1, α_2 and of α_3 (α_4) we calculate the value of α_4 ($\alpha 3$). Again, the details of how determine the coefficients is given in reference [13].

2.5 Mission Applications

The points L_4 and L_5 lay in large practically stable regions. A spacecraft placed on them would not need station keeping maneuvers (or very small ones) and, therefore, are suitable for parking regions. Some science fiction writers and futurists already suggested the construction of permanent colonies at these points [4].

The libration points L_1 and L_2 are nowadays more interesting from the application point of view since they generate and control many trajectories with interesting applications to space missions and planetary science. Some of their characteristics of the which are useful are listed below, for both systems Sun-Earth (SE) and Earth-Moon (ME)

- They are easy and inexpensive to reach from Earth;
- The SEL1 provides good observations sites to the Sun;
- Orbit around SEL2 provides a continuous view of half of the celestial sphere since the Earth, the Moon and the Sun are always behind it;
- Even the points of the SE system are not very far from the Earth (around 1.5 millions km) which implies in easy communication system designs;

- The SEL2 is highly favorable for missions that requires great thermal stability;
- The EML2 to establish a permanent communication link between the Earth and the hidden part of the Moon;
- Orbits around them can provide ballistic planetary captures;
- Orbits around them can provide interplanetary transport;
- They make possible formation flights with a rigid shape;
- They provide good Earth transfer and return trajectory, one characteristic that will be used in this project.

Between several missions accomplished and planned using the libration points we can cite

ISEE-3 The International Sun-Earth Explorer 3 was launched in August 12, 1978 [4], with the objective of studying the Earth-Sun interactions. It was the first libration point mission, and orbited a halo orbit around the SEL1 for nearly 4 years;

SOHO The Solar Heliospheric Observatory was launched in December 2, 1995, and was the second mission to the SEL1. Its operational lifetime was planned to be of 2-years, and even with difficults until today it provides images and data [23];

Genesis Launched in August 28, 2001, the Genesis mission was the first designed with modern Dynamical Systems Theory. It was send to the SEL1 to collect solar wind and in April 2004 started the return leg which included a pass close to the SEL2 point.

NGST The Next Generation Space Telescope (or James Webb Space Telescope JWST, as it was renamed in 2002) is planned to be the successor of the Hubble Space Telescope. Its launch is planned to not before 2013 [22] and it will be placed in an orbit around SEL2.

For a more complete list see [4].

3 Low Thrust Propulsion and Launchers

In order to move a spacecraft between different orbits, a change in its motion is needed. This is the objective of its propulsion system. There are several propulsion technologies, with different applications. Between these technologies, the *low thrust propulsion* has been recently applied and stands as a important candidate to be widely used specially in future deep-space missions.

When speaking about low-thrust, the *electric propulsion systems* are distinguished as the most important due to their performance characteristics. They will be the focus of the discussion of the first part of this section, which has the objective of presenting the basic characteristics of low-thrust propulsion and their nowadays applications to space missions.

One important characteristic of the low thrust propulsion is that it can not be used to launch an spacecraft from Earth. Therefore it is important to define a low Earth orbit as a mission starting orbit. The spacecraft will be set in this LEO by a common chemical launcher which presents payload limitations. Therefore, the second part of this section, specifically subsection 3.7 deals with the basic performance parameters of modern launchers.

Finally, the last two subsections 3.8 and 3.9 are dedicated to present the thrust model used in this project and the ranges of its parameters tested throughout the work.

3.1 An Overview about Spacecraft Propulsion

Spacecraft propulsion is completely involved with rockets. Rocket propulsion is characterized by producing *thrust* by expelling stored matter which is called *propellant*. In order to eject the propellant with enough velocity, an energy source is needed. Several rocket propulsion technologies available are presented below (see [10]).

Cold gas. In this case, the energy is pre-stored in the form of pressure of the propellant. The basic idea is expand it throughout a nozzle, decreasing its pressure while increasing its velocity.

Liquid. The liquid rocket propulsion systems (LRPS) are a type of the called *chemical propulsion systems*. The stored propellant in the liquid state feeds a combustion chamber in which the energy is released from the same propellant by a chemical reaction. The energy heats the propellant which are converted into hot gases which are accelerated in a

convergent/divergent nozzle. Usually they are divided in monopropellant and bipropellant systems.

Solid. The basic idea is similar to the liquid one, but in this case the propellant is stored in the solid state directly in the combustion chamber. Therefore, once the reaction is started its is very difficult to stop it.

Hybrid. Hybrid rocket propulsion system combines solid and liquid chemical propulsion. Usually the propellant is stored in the solid state in the combustion chamber while the oxidant is stored liquid in a separated tank and continuously inserted into the combustion chamber. The resulting hot gases are also accelerated by a nozzle before ejected.

Nuclear. The nuclear systems are similar to the liquids ones, but in this case the energy does not come from the propellant, but from a nuclear fission reaction that provides it heat. Usually the used propellant is hydrogen.

Electrical. The basic idea is to use electricity to add energy to the propellant. This electricity can be provided by different ways such as batteries (chemical), solar or nuclear systems. There are different kinds of electric rockets such as *electrothermal*, *electrostatic* and *electromagnetic*. Their differences will be explained later.

3.2 Basic Propulsion Parameters and Equations

The thrust generated by a rocket propulsion system is based in the principle of conservation of momentum. Considering an inertial reference system which moves with a constant velocity equal to the spacecraft's initial velocity, its initial momentum is conserved if a small mass dm is ejected without the use of any external forces. Therefore, we can write

$$(m - dm)\, dv = -dm v_e \quad \Rightarrow \quad \int_0^{\Delta v} dv = -v_e \int_{m_i}^{m_f} \frac{dm}{m} \tag{3.1}$$

where m_i is the spacecraft initial mass, m_f is its mass after the ejection and v_e is the velocity of the ejected particle in relation to the spacecraft. It was also considered that $dvdm \approx 0$. Thus

$$\Delta v = -v_e \ln\left(\frac{m_f}{m_i}\right) \tag{3.2}$$

which is known as the *ideal rocket equation*, where Δv is the resultant change of the spacecraft velocity.

Considering m_p the mass of consumed propellant, we can write

$$m_p = m_i - m_f \tag{3.3}$$

and the equation 3.2 can be rearranged as

$$m_p = m_i \left(1 - e^{-\frac{\Delta v}{v_e}}\right) = m_f \left(e^{-\frac{\Delta v}{v_e}} - 1\right). \tag{3.4}$$

Before going further, the definition of three important rocket performance parameters must be given. The *specific impulse* (I_{sp})is the total impulse per unit weight of propellant, mathematically

$$I_{sp} = \frac{\int_{t_0}^{t} F dt}{g_0 \int_{t_0}^{t} \dot{m} dt} = \frac{F}{g_0 \dot{m}} \tag{3.5}$$

where F is the thrust, g_0 is the constant gravity acceleration at sea-level and $\dot{m}$ is the propellant mass flux. The second equality is valid if we consider that the thrust and the mass flux are constant. It is interesting to note that the I_{sp} has the dimension of time.

Although most of the thrust generated by a rocket came from the momentum conservation, some can be caused by the different pressure between the exhausting propellant and the external environment. This fact motivates the creation of a concept named *effective exhaust velocity* (c), which satisfies the equation

$$F = \dot{m} c \tag{3.6}$$

Thus, the effect of the pressure force can be accounted in the rocket equation 3.2 if the term v_e is replaced by c.

Combining equations 3.5 and 3.6, the basic relation between the specifc impulse and effective exhaust velocity is obtained

$$I_{sp} = \frac{c}{g_0} \tag{3.7}$$

Therefore, the equation 3.4 can be rewritten as

$$m_p = m_i \left(1 - e^{-\frac{\Delta v}{I_{sp} g_0}}\right) = m_f \left(e^{-\frac{\Delta v}{I_{sp} g_0}} - 1\right) \tag{3.8}$$

3.3 Electric Propulsion: Applications, Advantages and Disadvantages

Table 3.1 presents a comparison about the performance parameters of the major rocket systems.

From table 3.1 it is clear that the electric propulsion systems can provide much higher values of specific impulse then chemical systems, but with lower accelerations.

Table 3.1: Comparison of Space Propulsion Performance Parameters (copied from reference [10])

Type	**Specific Impulse** [s]	**Thrust/Weight**	**Thrust Duration**
Chemical	200-465	1-10	minutes
Nuclear (thermal)	750-1500	1-5	hours
Electrothermal	300-1500	$< 10^{-3}$	years (intermittent)
			months (steady)
Electromagnetic	1000-10000	$< 10^{-4}$	years (intermittent)
			months (steady)
Electrostatic	2000-100,000+	$< 10^{-4} - 10^{-6}$	months - years (steady)

From equation 3.8, higher values of specific impulse results in less propellant mass needed to archive a given Δv, i.e., to accomplish a given mission [2]. This is the bigger advantage of the use of electric propulsion systems.

Nevertheless, the low thrust provided by electric propulsion restricts its use. Its major consequence is that electric propulsion systems cannot be used to overthrow strong gravitational fields, i.e., they can not be used to launch an spacecraft from the Earth. Thus, a mission with electric propulsion always begins with the spacecraft already in space, launched priorly by a conventional chemical rocket.

This low-thrust also implies in completely different orbital maneuvers done by the spacecraft. While in missions with chemical rockets the burning time is very small, as can be seen in table 3.1, the electric propulsion systems must work for weeks and even months to archive the same Δv. This results in a spiral orbit trajectory in contrast with the simpler and quicker conical arcs resulting from chemical propulsion as illustrated in figure 3.1.

These spiral trajectories result in performance losses in comparison with a Hohmann transfer, since the thrust vector is not applied singularly at the optimum points of the trajectory, but in all them in a continuous way. Nevertheless, the gain due to the highest specific impulse compensates these losses resulting in a higher performance.

Moreover, the maneuver time needed when low-thrust propulsion is used is usually greater. Since the acceleration is slower, more time is needed to archieve the same value of Δv. However, low thrust thrusters can provide higher Δv with the same propellant mass, which results, in some cases, in less maneuver time [10].

[2] An important observation must be made that the value of Δv is usually greater when using low-thrust for a same mission, due to inefficient resulting from the continuous thrust. Therefore, a more detailed study must be done in order to choose the best propulsion system. Nevertheless, the low-thrust always allows bigger payload when large Δv are required.

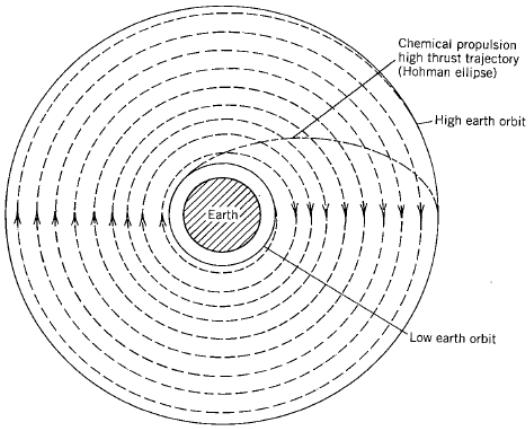

Figure 3.1: Comparison between impulsive and low-thrust maneuvers (from reference [18])

3.4 Electric Propulsion Systems

An electric propulsion system consists in basic four elements (see [10]): the propellant handling system, the electric power system, the thermal management system and the electrical thruster system. The first three will be briefly discussed in this section. Due to the different types and characteristics, the thruster system will be discussed in the next subsection.

3.4.1 Propellant Handling and Thermal Management Systems

The propellant handling system includes the propellant storage (tanks) and their control devices such as sensors, valves and temperature control. It is also present in chemical rockets with the difference that, in electric propulsion systems, they are very smaller and their weight is not very considerable.

Since heat is produced from different parts of the propulsion system, a control must be performed by the thermal management system. It basically comprises controls, coolers and radiators. Waste heat is produced by the power generation, in the power conversion and in the thruster.

3.4.2 Electric Power System

The existence of this system is probably the major difference between the electric propulsion system and the chemical ones. It involves the generation and conversion of energy, two actions

that, when chemical systems are used, are done at the Earth, since the propellant loaded already contain, in its chemical structure, the energy that will be released in its the combustion.

The power source to the electric system can be basically two: radiant or nuclear. The use of nuclear energy involves not only environmental questions but it is also political problems and have been postponed into the indefinite future [10]. Radiant energy can be of two forms: solar and beamed. The second one consists in emitting energy from the Earth in form of microwave or laser to the spacecraft, and has not been fully developed.

Therefore, the only real option nowadays is the use of solar arrays, which has as advantages their long lifetimes (around 10 years [18]) and their extensive use. Due to the fact that the spacecraft can be in eclipse conditions, rechargeable batteries are needed to provide power to the thrust during these periods.

The power conditioning equipment is the responsible for the needed energy conversions. For example, a typical output voltage for solar cells is between 28 and 100 V, while an ion thruster needs at least 1000 V to work. Usually it is considered a complex ”black box” with hundreds of parts and consumes between 10 to 20% of the incoming power [18].

The power system is usually much heavier than the thrusters being the dominant factor in the propulsion system total weight. Its estimation is done considering it a function of its power, using the parameters specific power (α) or specific mass (β) defined by (see [10])

$$m_{inert} = \beta P_S = \frac{P_S}{\alpha} \tag{3.9}$$

where P_S is the system required electric power.

The weight and available power of the electric power system limits all the propulsion system, since higher thrusts usually requires higher electric power. In some missions, however, the same electrical power system can be used by both the propulsion system and the payload, if both are not used simultaneously. This increases the advantages of the use of electric propulsion specially to raise the orbits of telecommunications satellites from LEO to GEO.

3.5 Electric Thruster System

As the heart of the propulsion system, it is the responsible for providing energy to the propellant and expelling it to generate thrust. Several electric thrusters technologies exists, and a small introduction about each one and special details of the ion-thrusters, which are the most

indicated to the mission discussed in this project, will be presented here.

3.5.1 Electrothermal Thrusters

In this kind of thrusters, the propellant is heated electrically. This results in its expansion and the resulting hot gases are accelerated to supersonic speeds through a nozzle. Thus, this kind of thrusters is the most similar to the chemical ones.

Two kind of electrothermal thrusters exists and they are differenced by the way used to heat the propellant. In the *resistojet*, a surface which is in contact to the propellant is electrically heated. The other form is to heat the propellant flow directly by creating a voltaic arc inside it, which is the principle of the *arcjet*.

The major disadvantage of electrothermal thrusters is that they provide low I_{sp} in relation to other electric thrusters. Between their advantages, the resistojets are simple devices, easy to control and have flown several time in satellites to station-keeping missions (see [18]). The arcjet however, even providing a high potential thrust, needs very high electric input power, and is still being developed.

3.5.2 Electromagnetic Thrusters

Electromagnetic thrusters work based in the *Lorentz force* which acts on a gas that carries current in a magnetic field

$$\vec{F}_m = \vec{j} \times \vec{B} \tag{3.10}$$

where $\vec{F}_m$ is the resulting Lorentz force per unit of volume, $\vec{j}$ is the electric current density passing through the gas and $\vec{B}$ is the magnetic induced field in gas. Therefore, the resulting force in perpendicular to the current flow inside the gas.

Electromagnetic propulsion includes various devices which are usually divided between unsteady vs. steady and self-field vs. applied field. Between the most important are the the *pulsed-plasma micro-thruster*, the *magnetoplasmadynamic thruster* (MPD) and the *Hall effect thruster*.

The first one uses pulsed discharges through a block of Teflon propellant to transform a small part of it in plasma, which is accelerated by an magnetic field. This kind of thrusters have been used in stationkeeping with great success.

The MDP thrusters are examples of steady electromagnetic thrusters that can be used for deep-space missions. They can also be self-field or applied field. The first one closely resembles an arcjet, while the second allows higher voltages.

The Hall effect thrusters actually present characteristics of both electromagnetic and electrostatic thrusters. They combine a static radial applied magnetic field with an axial electric field to operate as electrostatic accelerators without grids.

3.5.3 Electrostatic Thrusters

Electrostatic thrusters use the simplest notion of an electric rocket engine: the particles are accelerated by an electrical field.

The basic difference between the electrostatic forces concerns the kind of particle used, and how it is generated. Electrons would be our first idea to candidates for ejected particles since they can be easily generated and accelerated. However, their extremely low mass results in very low momentum even with high velocities.

Therefore, the particles used are positive ions, which are approximately 240,000 times heavier than an electron, or charged colloids, usually small liquid droplets 10,000 times heavier than positive ions. The experiments with colloids were performed specially by european countries. The ion thrusters are the most developed and will be the focus of this discussion.

Several types of ions sources have been developed, but the principal technique presently used is the electron bombardment plasma source [10]. Figure 3.2 presents the basic arrangement of an ion thruster.

Their work can be described in the following steps

1. The propellant vapor is inserted inside the ionization chamber maintained at a low pressure.
2. A thermal filament serves as central cathode emitting electrons, which are attracted towards the cylindrical anode but also influenced by a weak axial magnetic field. The result is a spiral axially motion of the electrons until they collide with a propellant atom and ionize it.
3. The positive ions are attracted by a strong electrical field of the first screen and pass

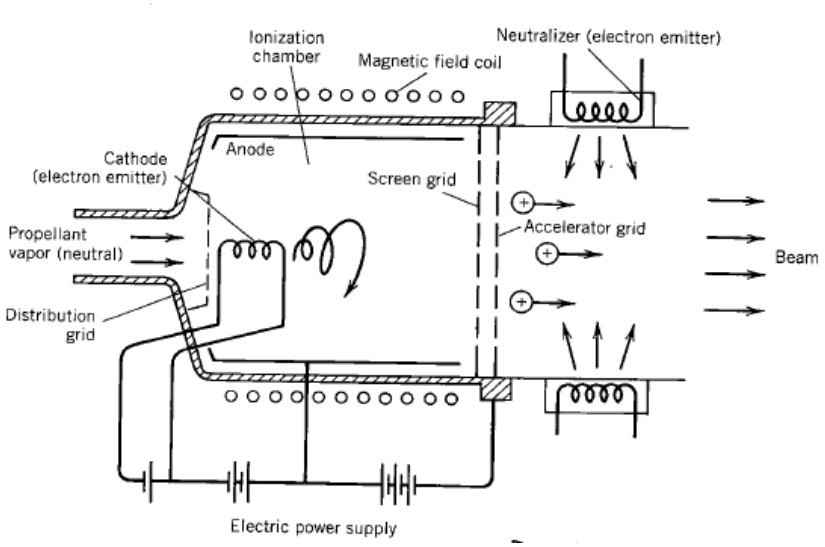

Figure 3.2: Simplified schematic diagram of electron bombardment ion thruster (copied from reference [18]).

through its openings.

4. Thus the ion enters in the acceleration region between the grids where the strong electrical field accelerates and ejects them with a high velocity. Typical values for the voltage between the grids are between 1000 and 2000kV generating an specific impulse from 2000 to 4000s [7].

5. Finally another emitter cathode emits electrons to neutralize the exhaust beam, keeping the spacecraft neutral.

The first works with ion thrusters used cesium and mercury as propellants [18]. They were abandoned because for several reasons including that they are hazardous and leave condensates on spacecraft surface. Nowadays the most used propellant is xenon due to its high mass and low ionization potential.

3.6 Mission Applications and Data of Ion Thrusters

The Deep Space 1 spacecraft, launched on October 28, 1998, was the first spacecraft to use solar-electric propulsion on a deep-space mission [3]. Its propulsion systems consisted in singles xenon-ion engine, provided by the NASA Solar electric propulsion Technology Applications Readiness (NSTAR).

The engine proved to be able to provide the required Δv of 4.5 km/s for the June 29, 1999

flyby of the asteroid Braille with only 81kg of propellant. The result was the validation of the ion propulsion as a credible propulsion option for future deep-space missions.

In order to illustrate the basic characteristics of an ion propulsion system, table 3.2 shows the basic data of NSTAR system.

Table 3.2: Basic characteristics of NSTAR system (all data from reference [3]).

Parameter	Value	Parameter	Value
Thrust		Solar Array Voltage	
Minimum	20 mN	Minimum	80 V
Maximum	92 mN	Maximum	160 V
Specific Impulse		Thruster Efficiency (electrical to kinetic energy)	$\geq$ 99.6%
Minimum	1950 s	Masses	
Maximum	3100 s	Ion Engine	8.33 kg
Thruster Input Power Range		Power Processing Unit	15.03 kg
Minimum	500 W	Xenon Feed System	20.47 kg
Maximum	2300 W	Digital Control and Interface System	2.47 kg
Thruster Diameter	30 cm	Power Processing Unit to Ion Engine Cable	1.70 kg
Accelerating Grid Voltage	1280 V	Total (without the power generating system)	48.00 kg
Engine-design life	8000 h	Solar Array Power (@1 AU solar range)	2500 W

Although the NSTAR was a great success, it still lacks sufficient performance parameters for many of the more challenge space science missions. Recently, the NASA's Evolutionary Xenon Thruster (NEXT) was chosen to be developed by the Next Generation Ion (NGI) NASA Research Announcement (NRA). The key improvements over the NSTAR are higher power and lower specific mass, and to a lesser extent higher specific impulse. NEXT is being developed for operation with input powers from 1kW up to 10kW and thrusts up to 364 mN. Its lifetime should not be less than 300 kg of propellant if not more. Form more details see reference [16].

As cited before, the power systems limits restricts the electric propulsion systems. Researches are being developed aiming power systems able to supply from kilowatts to megawatts of power to the electric thrusters, which could be possible with advance nuclear systems. An alternative approach to reach higher I_{sp} values (more than 6000s) would be the use of krypton or argon as propellants requiring voltages from 2kV to 10kV or more. To increase thrust power at a given I_{sp}, however, larger thruster diameters maintaining a uniform small intergrid spacing are needed, which presents an structural challenge, particularly when launch vibrations are considered. Detailed information about these advanced studies with ion and other electric thrusters can be obtained from reference [7].

3.7 Launchers

This subsection is dedicated to present performance data of current launcher vehicles which are capable of delivering a medium/large payload mass to a low-earth parking orbit. From this orbit, the low-thrust thrusters are activated to conduce the spacecraft until the invariant manifold of a libration point orbit.

The launchers present restrictions not only on maximum payload but also on eccentricity and inclination of the parking orbit. These limits are related to the launcher design and also to the launch base.

Informations presented in this section are totally based in references [1] and [17], the launchers user's manuals which have large amount of details about each one of the launchers.

Performance data presented in this references are not optimized because they do not take into account the specificity of the mission. However they can be used for a preliminary performance assessments which is more than sufficient for this project, where we only want to have idea of accessible low earth parking orbits.

3.7.1 Ariane 5

In 1973, the European Ministers made a bold decision to develop the Ariane launch system. The main purpose was to secure to Europe its own access to space. The first flight of Ariane 1 took place on the 24th December 1979. The need of increasing payload capacity lead to more powerfull derivatives: Ariane 2, 3 and 4 with payload capacities of 2,200, 2,700 and 4,480 kg to a GTO. The development of Ariane 5 was approved by the European Ministers in 1987, and was based on a rather different architecture. Today, Arianespace, the Ariane company, has a experience of more then 250 launch contracts, 163 flights and 214 satellites successfully launched.

The Ariane 5 launcher is basically a two-stage-vehicle with solid strap-on boosters. These two boosters provide 90% of the launcher thrust during lift-off. A cryogenic core stage ignited and checked on ground provides thrust for the first part of the flight up to upper stage ignition. Finally, a cryogenic upper stage further enhance the total lift capacity.

The launch preparation and launch are carried out from the Guiana Space Center (CSG), the European spaceport operational since 1968 in French Guiana. It is located at $5^o13'56''$N

and $52^o46'32''$W and governed under an agreement between France and the European Space Agency. The CSG used to accommodate only the Ariane 5 launch facilities, but was recently extended to cover Soyuz and Vega installations.

The performance computations presented in reference [1] are expressed in payload mass. However, this mass includes the mass of not only the spacecraft but also from:

- the dual launch system (if used) which mass can be from 425kg to 830kg;
- the adaptors and dispensers;
- the raising cylindrical structure (if used), which mass can be from 180kg (500mm) to 305kg (2000mm).

Moreover, they are based in the following assumptions:

- cryogenic main core and upper stage carrying sufficient propellant to reach the target orbit with the specified probability of 99% except otherwise specified;
- aerothermal flux at fairing jettison and second aerothermal flux less or equal to 1135 W/m^2;
- altitude values given with respect to a spherical earth radius of 6378km;
- launching from the CSG taking into account the relevant safety requirements;
- medium fairing.

Low Earth Circular Orbit

Reference [1] just cite the possible use of the Ariane 5 as a Automated Transfer Vehicle to serve the International Space Station. This kind of orbit can be described by:

altitude range:	between 200 and 400km
eccentricity:	0 (circular)
inclination:	51.6 degrees

Elliptical Orbit Mission

For comparing purposes, the reference [1] provides the Ariane performance in an injection towards the L2 lagrangian point of the Sun/Earth system:

apogee altitude:	1,300,000 km
perigee altitude:	320 km
inclination:	14 degrees
argument of perigee:	208 degrees
performance:	6.6t

3.7.2 Soyuz

The Soyuz/ST is the most recent launch vehicle from the most frequently launched family of rockets in the world. The first satellite and the first man into space were launched with vehicles of the same family which accumulates more then 1650 launches to date. Soyuz launch vehicles continue to be mass-produced in Russia in an uninterrupted production at an average rate of 10 to 15 vehicle per year.

The reference [17] even been the newest manual, is from 2001 and reports that the first flight of the Soyuz/ST would take place in the second half of 2002. According to the STARSEM web-page [21], the actual version of Soyuz is the Soyuz 2-1a, which had its first flight in November 8th 2004, and was equipped with a digital control system that was one of the difference from Soyuz to Soyuz/ST described in reference [17]. The ST fairing upgrade is still a next step of the Soyuz evolution program.

The Soyuz and Soyuz/ST consists primarily of the following components:

- a lower composite consisting of four liquid-fueled boosters (first stage), a core (second) stage, and a third stage;
- a restartable Fregat upper stage (fourth stage);
- a payload fairing and interstage section;
- a payload adapter/dispenser with separation systems.

The Soyuz and Soyuz/ST launch vehicles take off from the Baikonur Cosmodrome, located at Kazakhstan. A international agreement forged between Russian and Kazakhstan allows its use until 2020. Its coordinates are 45.59^o N and 63.33^o E. Due to its location, far from free areas as oceans, the launch azimuth direction for the vehicle ascent trajectory is very constrained by ground-path safety rules as well as by the limited number of authorized drop-zone locations for the expended stages.

Table 3.3 presents the allowed azimuths and the correspondent orbit inclination. These are the only authorized initial parking-orbit planes to which the three first stages can be directed to. A change of ± 5 degrees can be carried out during the third-stage flight. Any remaining inclination change is performed by the Fregat and other calculations must be done. That is why the curves presented in this section can not be interpolated.

Table 3.3: Approved launch Azimuths from Baikonur Cosmodrome [17]

Launch Azimuth	Correspondent Reference Orbit Inclination (Direct Ascent Trajectory)
60.70	51.80
34.80	64.90
25.90	70.40
-10.90	95.40

The assumptions made to the performance calculations presented here were the same as for the Ariane. Moreover, the performance is also expressed in overall payload mass which means that adaptors and dispensers masses must be subtracted from the presented values.

Circular Orbits

Depending on the required inclination of the final orbit, two different Fregat flight profiles can be chosen. One is a three-burn profile that optimize performance and the other, a two-burn profile that minimizes the mission time. The data presented here are all based in a Fregat three-burn flight profile.

Figure 3.3 present the general performance of Soyuz for low circular orbits. As explained before, only curves related to the authorized launch inclinations are presented. The right side of figure 3.3 presents an estimation of the impact in the performance if a different inclination is required.

Low Elliptical Orbits

As for the case of circular orbits, two Fregat flight profiles can be chosen depending on the perigee altitude and the inclination of the final orbit. The performance for a perigee altitude of 200km and a two-Fregat-burn mission profile is presented in figure 3.4.

Injection Accuracy

The accuracy of the Soyuz and Soyuz/ST configurations is determined by the performance of the Fregat upperstage. The table 3.4 presents, as an example, the accuracy for a 1000km

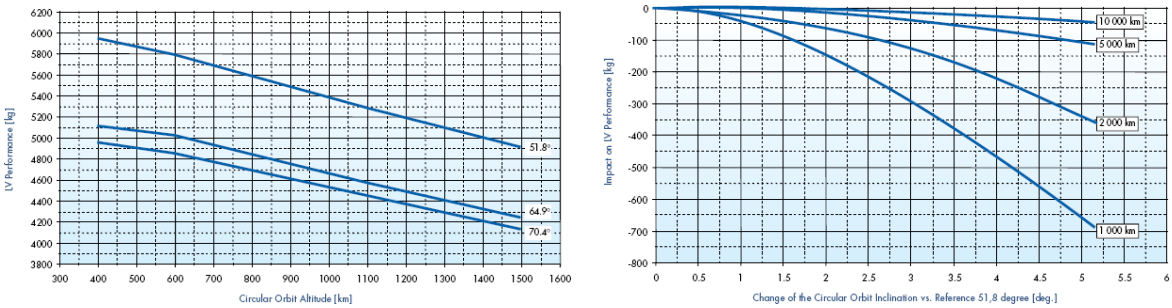

Figure 3.3: Soyuz Performance for Low Circular Orbits (right) and Typical impact on Soyuz Performance for Changes of Inclination for Circular Orbits with Reference Value of 51.8 degrees (left) (Copied from reference [17]).

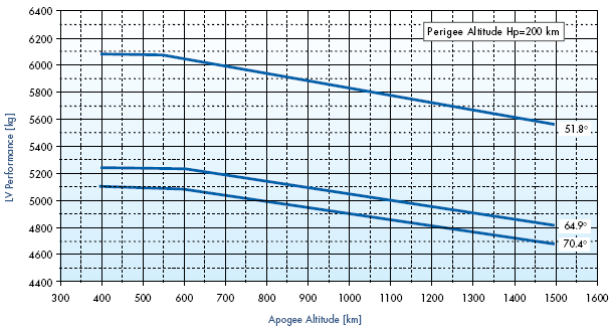

Figure 3.4: Soyuz Performance for Low Circular Orbits (Reference [17]).

circular orbit altitude.

Table 3.4: Injection Accuracy for Soyuz with Fregat Upper Stage [17]

Orbital Parameter	Accuracy
Semi-major axis (km)	$\pm$ 10
Eccentricity	$\pm$ 0.002
Inclination (ang min)	$\pm$ 6
Period (sec)	$\pm$ 12
Right Ascension of the Ascending Node (ang min)	$\pm$ 9

3.8 Model of the Low-Thrust

The objective of this project was to study transfers from low-Earth to libration point orbits using the invariant manifolds and low-thrust. The work was concentrated in the use of the simplest possible thrust, i.e., a constant thrust with a constrained direction from the starting orbit until the invariant manifold is reached. This section is devoted to explain the hypotheses adopted and to present the mathematical model used.

The thrust magnitude F_T was one of the simulation parameters and although we refer to it was constant, it can also assume the zero value during coast periods. Therefore, it can be mathematically expressed as

$$F_T(t) = \begin{cases} F_T & \text{if} \quad t \in I_t \\ 0 & \text{if} \quad t \in I_c \end{cases} \tag{3.11}$$

where I_t and I_c are the thrust and coast time intervals, respectively.

The thrust direction vector, however, may be more deeply discussed. According to the reference [12] the variation of the semi-major axis of the orbit is maximized if the thrust direction is taken to be aligned with the velocity of the spacecraft respect to the Earth in the inertial frame. This was the first idea followed in this work, its results and a analysis of small changes to it are lately discussed.

Following, we present the derivation of the analytical expression of this thrust model, using the same symbology as in the derivation of the circular restricted three body problem (CRTBP) when possible.

Let $\vec{r}$ and $\vec{r}_i$ be the position's coordinate vectors of the spacecraft in the dimensionless CRTBP and sidereal frames, respectively (see appendix B). The relation between the two coordinate frames was already shown in equation B.7

$$\vec{r}_i = \mathbf{A}\vec{r} \quad , \quad \mathbf{A} = \begin{pmatrix} \cos t & -\sin t & 0 \\ \sin t & \cos t & 0 \\ 0 & 0 & 1 \end{pmatrix} \tag{3.12}$$

Where $t = nt^*$ is the time span in CRTBP units. Then,

$$\dot{\vec{r}}_i = \dot{\mathbf{A}}\vec{r} + \mathbf{A}\dot{\vec{r}} \quad \text{and} \quad \dot{\vec{r}} = \dot{\mathbf{A}}^T\vec{r}_i + \mathbf{A}^T\dot{\vec{r}}_i \tag{3.13}$$

From now on, the subscripts 's' and 'E' will denote *spacecraft* and *Earth* respectively. Then, the relative position and velocity of the spacecraft with respect to the Earth in the CRTBP frame is

$$\vec{r}_{sE} = \vec{r}_s - \vec{r}_E \quad \text{and} \quad \dot{\vec{r}}_{sE} = \dot{\vec{r}}_s - \dot{\vec{r}}_E \tag{3.14}$$

From the definition of the CRTBP reference system, we have that $\dot{\vec{x}}_E = 0$. Therefore, from

equations 3.13 and 3.14, the relative position and velocity in the inertial frame is given by the expression

$$\dot{\vec{r}}_{i_{sE}} = \dot{\mathbf{A}}\vec{r}_{sE} + \mathbf{A}\dot{\vec{r}}_{sE} \tag{3.15}$$

As we use the CRTBP reference system to integrate the system equations, the last step is transform the equation 3.15 using the matrix shown as equation 3.12, therefore

$$\mathbf{A}^T\dot{\vec{r}}_{i_{sE}} = \mathbf{A}^T\dot{\mathbf{A}}\vec{r}_{sE} + \mathbf{A}^T\mathbf{A}\dot{\vec{r}}_{sE} = \hat{\mathbf{A}}\vec{r}_{sE} + \dot{\vec{r}}_{sE} \tag{3.16}$$

where

$$\hat{\mathbf{A}} = \mathbf{A}^T\dot{\mathbf{A}} = \begin{pmatrix} 0 & -1 & 0 \\ 1 & 0 & 0 \\ 0 & 0 & 0 \end{pmatrix} \tag{3.17}$$

Recording the symbology used in appendix B, $\vec{r}_s = (x, y, z)$, therefore, using equations 3.16 and 3.17 we got the following expression for the thrust direction $\vec{a}_T = (a_{Tx}, a_{Ty}, a_{Tz})$

$$\vec{a_T} = (a_{Tx}, a_{Ty}, a_{Tz}) = (\dot{x} - y, \dot{y} + x + 1 - \mu, \dot{z}) \tag{3.18}$$

This thrust direction must be normalized before used with the thrust magnitude. Hence, the CRTBP perturbed model by this kind of thrust becomes

$$\begin{aligned} \ddot{x} - 2\dot{y} &= \frac{\partial\Omega(x,y,z)}{\partial x} + F_T(t)\frac{a_{Tx}}{||\vec{a}_T||} \\ \ddot{y} + 2\dot{x} &= \frac{\partial\Omega(x,y,z)}{\partial y} + F_T(t)\frac{a_{Ty}}{||\vec{a}_T||} \\ \ddot{z} &= \frac{\partial\Omega(x,y,z)}{\partial z} + F_T(t)\frac{a_{Tz}}{||\vec{a}_T||} \end{aligned} \tag{3.19}$$

with $T(t)$ as expressed in equation 3.11.

3.9 Parameters Defining the Model

From the discussion presented in all the above subsection, we can define the basic ranges of parameters to be used in the simulations performed in this project.

First dealing with the starting low Earth orbits. Rigorously speaking, they are not input parameters since the simulations are conducted backwards in time as will be explained in the next

section. Nevertheless, it is important to establish limit values for the acceptable derparture orbits.

As presented in subsection 3.7, the use of low eccentricity orbits provides the larger launch efficiencies in payload mass, thus this will be our first goal when performing the simulations. With respect to the inclination of the orbit, using Ariane for low inclination orbits would certainly allows larger payload deliveries, but we have no precise data about it, since reference [1] just discusses the launches to the ISS orbit inclination. Soyuz has the big problem of the limited launch angles, but, since more data is available in its user's manual, a better estimation of the payload could be done. Considering this, low inclinations are aimed, but middle ones are also acceptable.

With respect to the true anomaly, right ascension of the ascending node and argument of perigee, no restriction was determined. The last one has very low importance for low eccentricity orbits and the first ones can be settled by proper choosing of the launch window.

The more difficult parameter to be settled is the mean orbital altitude. The higher is the orbit altitude less payload is available by the launcher and more by the low thrust propulsion system. A detailed study should be performed to choose the best altitude to start the low thrust propulsion. This study, however is outside the scope of this project and has low influence in the main trajectory design as shown by the small tests performed in this project. Therefore, the reference altitude to start the low thrust propulsion was settled in 1000 km. In this altitude Soyuz can deploy a 5400 kg spacecraft at the 51.8° inclination low eccentricity orbit. The performance of Ariane 5 should be very higher since for 400 km altitude it can delivery a 19000 kg payload, however, precise data is not available.

Concerning the low thrust magnitude propulsion, the input parameter to the simulation programs was not the thrust itself but the thrust to mass ratio, or simply the acceleration in units of m/s^2. Several tests were performed throughout the work to study the influence of this parameter. In real mission design several configurations of thruster types and number can be tested, and the decision is highly dependent of specific mission characteristics.

The starting value for the simulations, however, was established based in the order of magnitude presented in table 3.1 and in the thrust to weight ratio of Deep Space 1 which was approximately 10^{-4}. Ratios from 10^{-3} to 10^{-5} have been used in the simulations.

4 Results from the CRTBP modeling with low-thrust

This section is devoted to present a detailed explanation of the methodology used to calculate the possible transfer trajectories and the results obtained with the simplest model, consisting of the CRTBP perturbed by a low-thrust propulsion.

4.1 The Dynamical Systems Approach

When stable manifolds are used in a transfer trajectory design, the method is known in literature as the *dynamical systems approach to the transfer problem*. Reference [4] details the proceedings to find impulsive transfers through this approach.

In the case studied in this project, however, we are interested in low thrust trajectories, and, therefore, the methodology used was a little different than those explained in [4] and is presented below.

One important observation is that the trajectories aimed in this project were the simplest possible, i.e, we look for trajectories that starts in a LEO, proceeds in a spiral path during the action of a constant magnitude low thrust force and then follows an invariant manifold. No transfer with intercalate thrust and coast arcs was studied.

The Low Thrust Dynamical Systems Approach

The modified Dynamical Systems Approach for a low-thrust transfer can be described by the following steps

1. An target orbit is defined, this includes the definition of the aimed libration point, the type of orbit and its amplitudes and frequencies;

2. A local approximation of the stable manifold at a certain point of this orbit is taken using the method derived by Masdemont and explained in section 2.4. This includes the choice of a starting phase. Moreover, it is necessary to choose the manifolds which goes towards your objective (in this case the Earth) and not in the other direction. The result is the determination of a line in the phase space based in a nominal point of the orbit;

3. With this starting state known, it is numerically integrated backwards in time for a defined period called t_{coast}, whose value is a chosen parameter. This integration is done with

thrust magnitude equal to zero, i.e, only considering the CRTBP equations, thus we are going through the line determined in the phase space;

4. After t_{coast} the vectorfield is changed including the low thrust, and the integration proceeds backwards in time until a determined altitude with respect to the Earth is reached.

5. The last state obtained is used to calculate the orbital elements of the parking orbit.

This method is used since launchers can put spacecrafts in different low-Earth orbits with not big penalties in payload if their eccentricities and inclinations are small as seen is section 3.7. The invariant manifolds, however, requires more precision in the state of the spacecraft due to the hyperbolic behavior of orbits near the libration points.

Libration points orbits chosen in this project has been restricted to halo orbits around the L_1 and L_2 points of the Sun-Earth/Moon system (SEL1 and SEL2). The expansion of the work to Lissajours orbits around these and other libration points are further planned steps as presented in section 6.4.3.

4.2 Halo Orbits around SEL1

4.2.1 Values of the Parameters

As discussed in section 2.4 a Halo orbit has equal in-plane and out-of-plane frequencies. Therefore, only one of the associated amplitudes is needed to define it, while the other is calculated by a given relation that must be fulfilled (see [4]). The amplitude used as the input one has been the out-of-plane amplitude denoted by α_4, and from now on it will be reffered as *halo orbit amplitude* without risk of misunderstanding. Its unit used in the project is dimensionless and its relation with dimensional units is presented in appendix E.

Remembering equations 2.15, since we look for stable manifolds, the amplitude α_2 must also be chosen, while $\alpha_1 = 0$. The value adopted was $\alpha_2 = 10^{-3}$, according to previous tests of the manifold determination function studied in [4]. The positive sign is needed to calculate the manifolds which move towards the Earth and the impact of changes in this magnitude was also studied and will be discussed later.

Moreover, a last parameter must be specified to the determination of the manifold, which is the phase of the halo orbit ϕ associated with it. All possible values, from 0 to 2π, were tested, since

in practical applications this value is not so important (once the spacecraft is in the halo orbit, after one period, it will pass through all possible phases).

In order to completely determine the total trajectories, two other parameters must be given: the time of coast t_{coast} and the thrust magnitude F_T. Various values for both parameters were tested and will be discussed later in this section.

The reference altitude to stop the backwards integration is set to 1000km with respect to the equatorial radius of the Earth. Changes in this value only influences significantly the maneuver time, as will be presented later.

As explained before the Sun-Earth/Moon system has been used. The constants associated with it and implemented in the programs are presented in appendix D, together with their respectively sources.

4.2.2 Behavior of the Manifold

Before discussing the proper results, it is interesting to present some of the characteristics of the stable invariant manifolds associated with halo orbits around the libration point.

Figure 4.1 presents the altitudes in kilometers as function of the time for all stable manifolds of an SEL1 halo orbit with $\alpha_4 = 0.08$. The time span chosen finishes after $t = 5.50$ CRTBP units, i.e, approximately 320 days, since we are not interested in very long transfers.

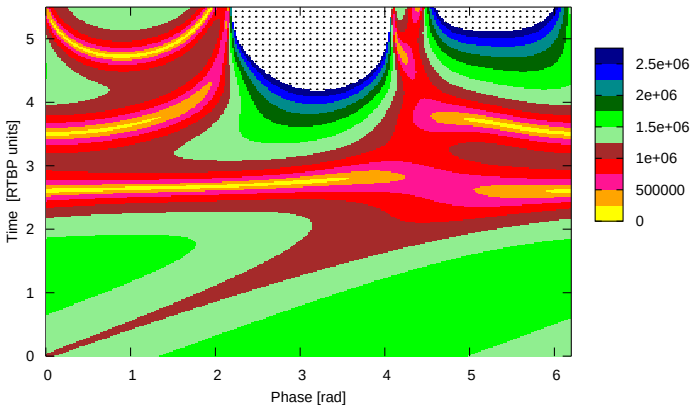

Figure 4.1: Altitudes (in km) of stable manifolds of SEL1 halo orbit with amplitude 0.08 (CRTBP units).

The points not colored correspond to altitudes greater than 2.5 millions of kilometers. Observing these results, the possible behaviors of the manifolds can be essentially divided in four groups. Table 4.1 presents the approximate intervals of values of ϕ with their respectively behavior.

Table 4.1: Manifold behavior for different phase starting values.

Phase interval [rad]	Manifold behavior for $t < 5.0$ [CRTBP units]
$\phi \leq 1.0$ and $\phi \geq 6.0$	Three passages near the Earth
$1.0 \leq \phi \leq 4.1$	One passage near the Earth and then moves away
$4.1 \leq \phi \leq 4.5$	The manifold keeps itself near the Earth
$4.5 \leq \phi \leq 6.0$	Two passages near the Earth and then moves away

These behaviors can be better understood by observing figure 4.2 where one orbit of each set is represented by its projection in the fundamental plane. These results will be fundamental to the discussion of the transfers trajectories below.

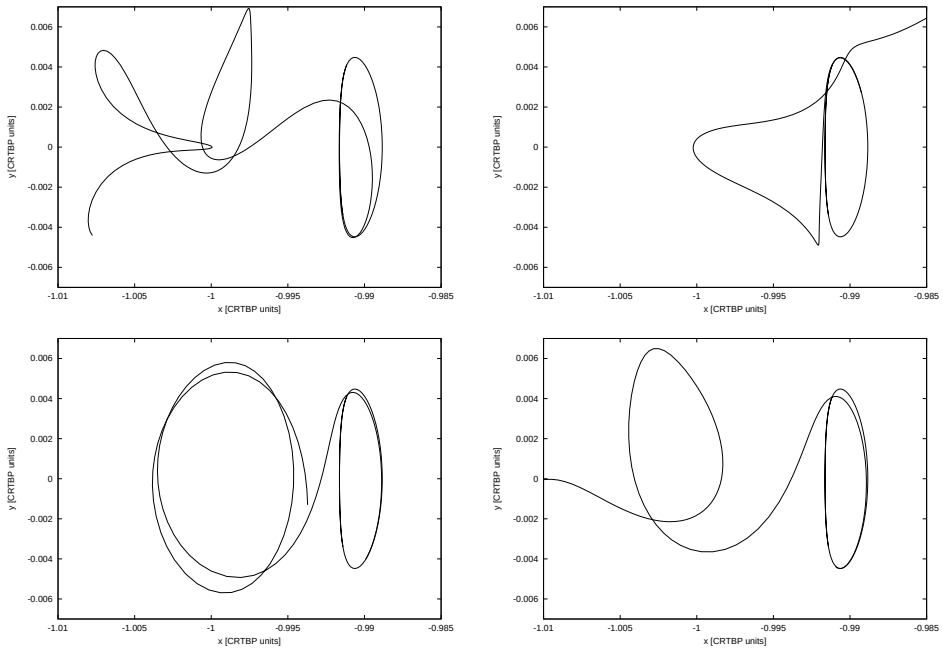

Figure 4.2: Manifold behaviors. From left to right and from top to down: $\phi = 0.50$ rad, $\phi = 2.50$ rad, $\phi = 4.30$ rad, $\phi = 5.00$ rad. All relative to a halo orbit with out-of-plane amplitude of $\alpha_4 = 0.08$.

These same behaviors were also observed for other values of halo orbit amplitude α_4, with very small modifications in the phase limits and altitude values.

Another parameter than could be modified is the α_2 amplitude. Reducing its magnitude means to choose a manifold local approximation closer to the halo orbit. In order to study the consequences of this change, figure 4.3 presents the analogous graphic of figure 4.1 but for

$\alpha_2 = 10^{-4}$. At the right hand side plot, three manifold orbits are compared.

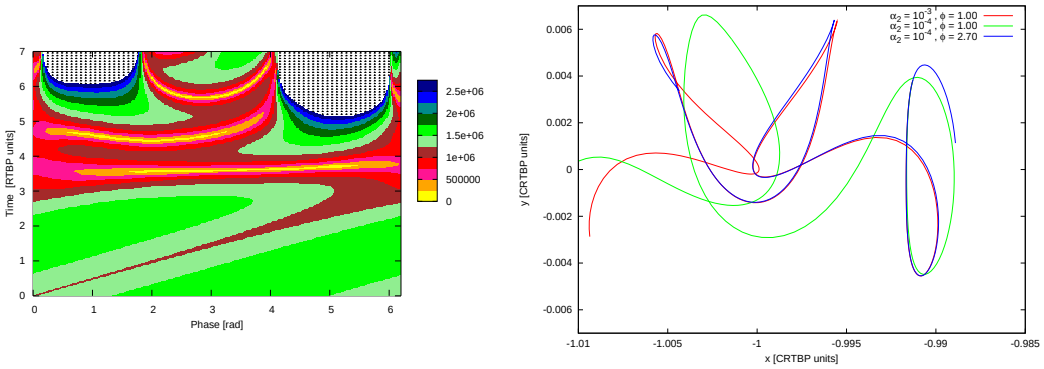

Figure 4.3: (Left) Altitudes as a function of the phase and time obtained setting to $\alpha_2 = 10^{-4}$. (Right) Comparison of different manifolds behaviors.

Comparing figure 4.1 with the left hand side of figure 4.3 two consequences of the change in the value of α_2 are evident. The map seams to be moved up (more time is needed to the manifolds to arrive near to the Earth) [3], and right (phase change). The reason for these shifts is illustrated at the right side of figure 4.3. Observe that a lower value of α_2 results in a manifold which is more time close to the halo orbit. This explains the longer time to arrive near the Earth and the phase change. Also from this figure it can be observed that the phase change is approximately of 1.90 radians positive when α_2 is decreased from 10^{-3} to 10^{-4}.

These observations have two important implications in the results presented later. The first one is the low information included in the parameter t_{coast}. Due to the asymptotic character of the approach, the time needed to a spacecraft to arrive to a halo orbit is not well defined. A manifold may be close enough to the target orbit to be considered already *the* target orbit.

The main conclusion is that the value of the phase and coast time only are meaningful if used together with a value of α_2. However, the changes produced by changing the value of this last parameter are simple dislocations of all the colored map to the right or to the left, therefore it does not affect qualitatively the results. Throughout this work, if not specified, the value of ϕ are always relative to $\alpha_2 = 10^{-3}$.

4.2.3 First Results

The first study accomplished consisted in computing trajectories for various values of phase ϕ and coast time t_{coast} for a given thrust magnitude F_T. The eccentricities of the departure orbits

[3] Observe that the time limit was expanded to 7.0 CRTBP units in figure 4.3

were then calculated and compared, since our objective was set as finding low eccentricity parking orbits.

Figure 4.4 is an example of the result of this study. The colors presented for each pair $(\phi; t_{coast})$ are related to the eccentricity of the parking orbit. The thrust for this test is set as $F_T = 1.00{\cdot}10^{-4}$ ms^{-2}, and the target halo orbit is of amplitude $\alpha_4 = 0.08$.

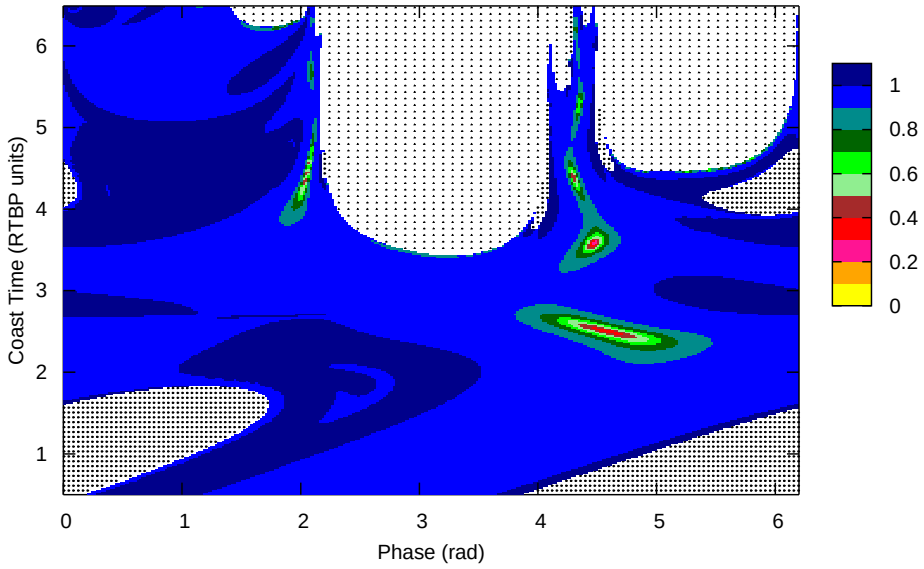

Figure 4.4: Eccentricities of the departure orbit for $F_T = 1.00 \cdot 10^{-4}[ms^{-2}]$ and $\alpha_4 = 0.08$.

Some zones of this map are not colored, but filled with two different point like patterns. The first one, on the upper side of the figure and less dense, represents the orbits that does not reach the reference altitude in a limit time which is also a parameter of the simulations. This time was usually set to $t_{lim} = 15$ CRTBP units, which corresponds approximately to 2.4 years or 870 days.

The actual algorithm to stop the simulation consists in computing the eccentricity of the orbit when this limit time is reached and, if it is not less than 0.5, abort the simulation. This was done in order to avoid aborting orbits with long spiral paths of low thrust and it proved to be efficient.

If we compare figures 4.1 and 4.4 it is clear that the points where this behavior is observed are the ones associated with manifolds that move away from the Earth. Since the thrust has a low magnitude, it would need much more time to carry the spacecraft till manifold that are far away

from the Earth.

The other region of figure 4.4 has a more complex explanation. In this regions, during the numerical integration, the spacecraft velocity with respect to the Earth in the sidereal system vanishes. The consequence is that the direction of the thrust vector becomes undetermined since it is defined by this vector as explained in section 3.8.

The first idea was that it was only a numerical problem, and solutions based in vanishing the thrust magnitude for small periods of time when this situation happened were tried. Nevertheless, it was later discovered that some of these orbits converge to new equilibrium situations that exists when the thrust is added to the CRTBP model.

These transfers were further studied looking for solutions. Finally it was understood that they were not of interest of the project and a small subroutine was set to abort the simulation in case the velocity with respect to the Earth became too small.

Observing the colored regions of the figure 4.4 it is notable the big blue areas corresponding to high eccentricities and the small regions were the parking orbits present low eccentricity values. This last regions are the ones we are interested in and seem to have a kind of convex and simple shape. In order to facilitate reading, from now on we refer as low eccentricity zones or regions these areas of the halo orbit phase - coast time surface where the parking orbit has low eccentricity.

Before discussing these regions more deeply, it is interesting to study the influence of the thrust on them. Figure 4.5 present the same study of figure 4.4 but for a lower and a higher thrust magnitudes.

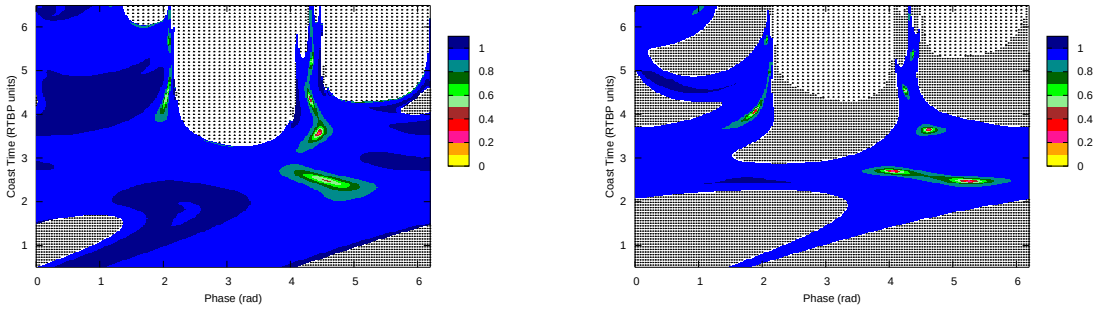

Figure 4.5: Same study presented in figure 4.5 with $F_T = 8.00 \cdot 10^{-5}[ms^-2]$ (left) and $F_T = 3.00 \cdot 10^{-4}[ms^{-2}]$ (right).

Comparing the three results from these two figures we can observe that the low-eccentricity regions evolve when changing the thrust magnitude but not dramatically. This is important since it means that a small deviation of the thrust magnitude are acceptable and it will still allow a successful transfer. Besides, it facilitates our studies.

Also from this comparison, we note that the regions associated with the thrust vector problem described above increase with the thrust magnitude. This fact, however, is not very important for our considerations, since they do not get close to the interesting low eccentricity zones.

In order to analyze these interesting zones more deeply, they were separated and numbered. Their number and basic characteristics are presented below

Zone 1 The biggest zone located approximately in the ranges determined by $4.0 \leq \phi \leq 5.0$ and $2.0 \leq t_{coast} \leq 3.0$ CRTBP units. For higher thrust magnitudes, the region splits in two ones named from now on as Z1A and Z1B respectively.

Zone 2 The second bigger zone, located above the Zone 1. This is, for the same values of phase ϕ, but bigger coast times. It has a very round shape.

Zone 3 Located at lower values of ϕ, near the value of 2 radians and coast time about 4CRTBP units. It has a very different shape compared with the previous two. Being very stretched. With the increase in the thrust magnitude it moves towards lower t_{coast} and phase values.

Zone 4 Also relative to the same values of phase as zones 1 and 2, but even higher coast time.

Other zones Very small zones can be noted above zones 3 and 4, and at other values of ϕ and t_{coast} for specific values of thrust, none of them proved to be of much interest.

It is interesting to present examples of transfer trajectories associated with each one of these zones. Figure 4.6 presents this for the thrust magnitude $F_T = 3.00 \cdot 10^{-4} ms^{-2}$. The filled circles in each transfer trajectory mark the end of the low-thrust arc and the beginning of the coast trajectory.

From this figure, it is observed the close relation between the zones 1, 2 and 3. All them are related to the third manifold type discussed above, which keeps close to the Earth describing circles around it. Zone 1 are the trajectories which meet the manifold in their first passage near the Earth, zone 2 meet in its second one and zone 4 in its third one.

However, orbits of zone 3 are completely different. The low-thrust spiral meets the manifold in its second approach to Earth. The manifold, in this case, gets closer to the Earth, but in a more

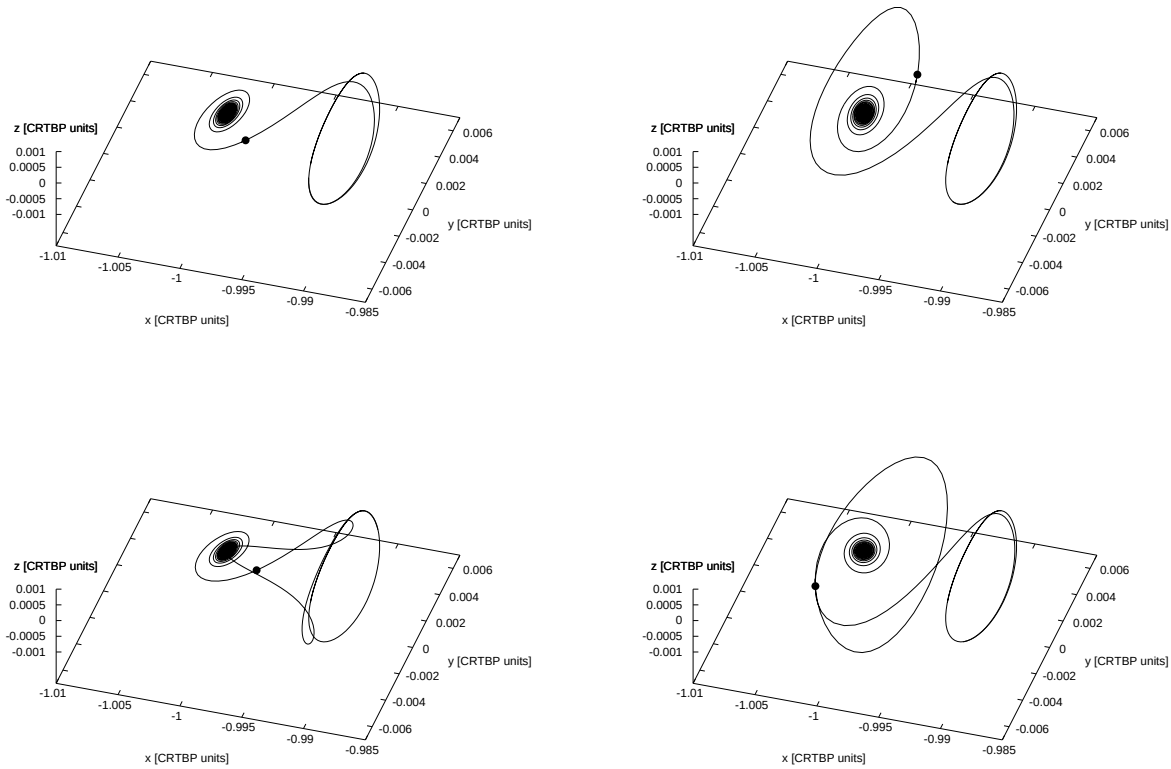

Figure 4.6: Examples of trajectories with low-eccentricity parking orbits. All of them calculated with $F_T = 3.00 \cdot 10^{-4}[ms^{-2}]$ and $\alpha_4 = 0.08$. From left to right and from top to bottom: Z1 $\phi = 4.0626$ $t_{coast} = 2.7050$ [CRTBP units], Z2 $\phi = 4.6190$ $t_{coast} = 3.6500$ [CRTBP units], Z3 $\phi = 1.8910$ $t_{coast} = 4.0700$ [CRTBP units], Z4 $\phi = 4.2470$ $t_{coast} = 4.5650$ [CRTBP units].

eccentric way when compared with the ones of other zones.

The since the goal is finding simple transfer trajectories from the Earth to libration point, the main candidates are orbits from the zone 1, since they seems to be the fastest and simplest ones. Orbits from zone 3, however, can also provide easy control due to its format.

Nevertheless, in the following discussions we keep into account all types of transfers, in order to compare them according to other factors.

4.2.4 Evolution and Size of the Low Eccentricity Zones

Once the low eccentricity zones described above were defined, simulations are performed around them with smaller steps in phase ϕ and coast time t_{coast}. The objective is to observe

the real format of the zones and how they evolve when changes in the halo orbit amplitude α_4 and thrust magnitude F_T are performed. Figure 4.7 illustrates this study.

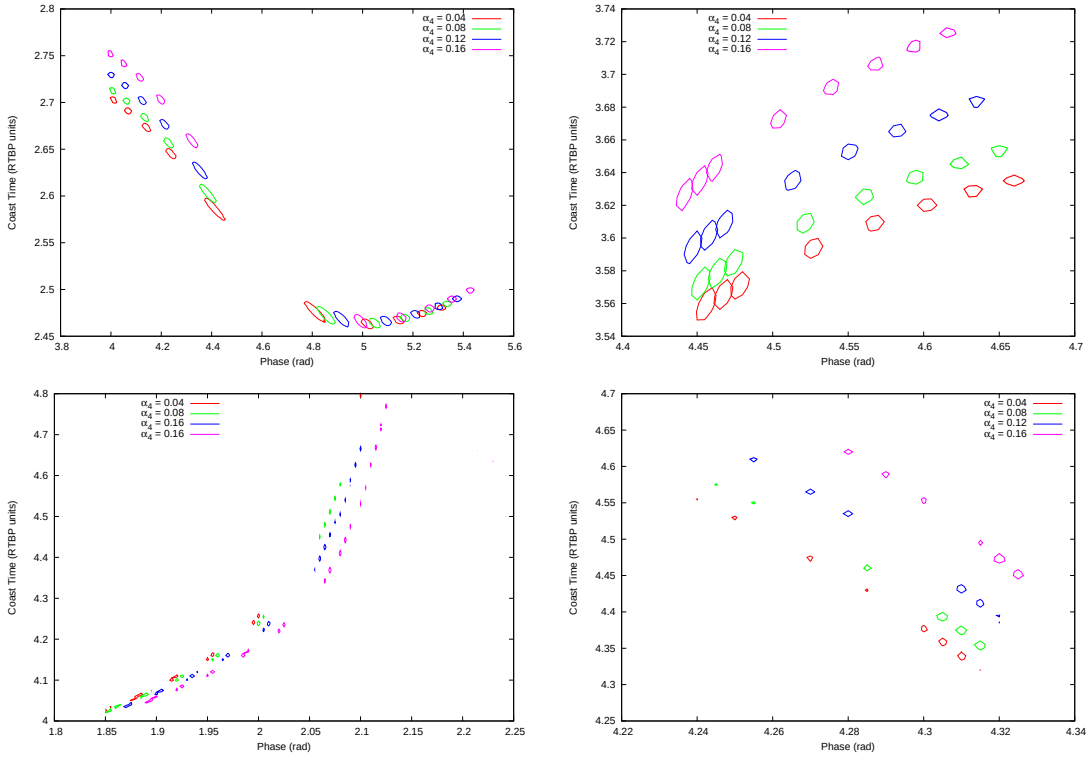

Figure 4.7: Evolution of the low eccentricity zones with changes in α_4 and F_T. From left to right and from top to bottom: zone 1, zone 2, zone 3 and zone 4.

Each graph in this figure shows the limits of the zones were the parking orbits present eccentricity below 0.1. The increase in the halo orbit phase is represented by the different colors of the lines and the increase in thrust magnitude by the increase in the width of the lines.

In the case of zone 1, near circular parking orbits are observed only when the thrust magnitude is equal or greater than $1.5 \cdot 10^{-4}$, and two separated regions of them exist as explained above. In zone 2 near circular transfers are possible for all halo amplitudes and thrust magnitudes tested, and for all of them only one continue zone is obtained.

Zone 3 presents its low-eccentricity zones split in various small zones, all scattered around a big range of parameters. This fact makes difficult to be analyzed the influence of the halo amplitude and thrust magnitude.

Finally zone 4 presents the sets in an organized way as zone 2, but the low-eccentricity orbits tend to disappear for high values of the thrust magnitude.

With respect to the size of the interesting zones, besides these figures, which can be a little tricky since the ranges are different, we can have a look at the sixth column of the tables presented in appendix F.

This column shows the number of calculated transfers inside each zone which have a parking orbit whose eccentricity is below 0.05. In order to give a meaning to this value, we must say that the simulations were done with intervals of 0.005 in both phase (rad) and coast time (CRTBP units). Thus, if the number presented is zero, we can say that if there are any transfer in this zone with parking orbit has a eccentricity lower then 0.005, then the area these transfers spread in the surface is slower than $2.5 \cdot 10^{-5}$ in the units used in the surface.

Although these units are difficult to compare with another known dimension (the coast time interval is approximately of 6 hours), the main objective in this study was to compare the zones between themselves, and this method is enough for it.

Comparing different zones we can say that zone 1 presents more interesting transfers than the others. Interestingly, for values of thrust lower than $1.5 \cdot 10^{-4} [ms^{-2}]$ no transfer with a near circular parking orbit was found, and for higher values than $3.0 \cdot 10^{-4} [ms^{-2}]$ only few ones were observed. A relation between the number of interesting transfers and the halo amplitude was not found.

In the case of zone 2, however, lower values of thrust magnitude seem to allow more interesting transfers. For zone 3 no specific behavior was noted, and, in zone 4, no transfer with this characteristics were found for the halo amplitude of 0.04.

Since the study was totally based in tests, we cannot affirm that no transfer orbit with near circular parking orbit is possible for a determined zone with associated halo amplitude and thrust magnitude. However, many tests were done accuratelly refining the grid of simulations in each zone. Figure 4.8 is an example.

As it can be seen, for this case no transfer with parking orbit eccentricity even less than 0.4 are found. Therefore we are impelled to say that for some combinations of halo amplitude and thrust magnitude, some zones do not present any transfer with near circular parking orbit. It is interesting to point out that this behavior is only noted for low thrust magnitudes in the zone 1 of the phase-coast time surface. In the other zones, for all the cases analyzed, even if no transfer with parking orbit eccentricity lower then 0.05 is found, many of them are only a little higher than this.

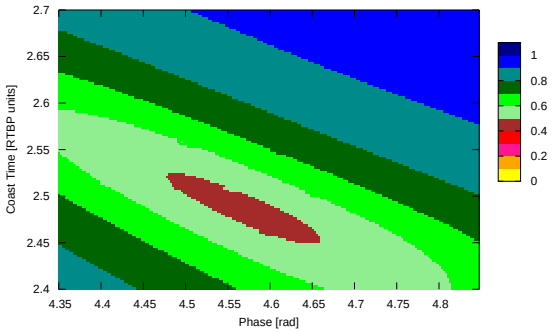

Figure 4.8: Eccentricity values of the parking orbits around the zone 1 for an halo orbit amplitude $\alpha_4 = 0.08$ and a thrust magnitude $F_T = 8.0 \cdot 10^{-5}[ms^{-2}]$.

4.2.5 Influence of the Parameters

Once the regions of interest in the phase-coast time plan were determined and several of their transfer trajectories simulated, the ones with lowest eccentricity of each zone were listed. All of them, with all their interesting parameters, are given in the table of appendix F. This section is dedicated to presenting the analyzis of this data and the results obtained.

The main objective is to determine the influence of the thrust magnitude and halo orbit amplitude in different characteristics of the parking orbit and of the total transfer. All data presented are of the transfers with lowest eccentric parking orbits in each zone.

The first characteristic of the parking orbit analyzed is, as already explained, its eccentricity. The results of this study are presented in figure 4.9.

As can be observed, no secure pattern is discovered from this figure. An even more precise study should be done, with very small steps of phase and coast time, in order to archive such kind of conclusions, if they are possible. Anyhow, this is not so interesting since a more precise model should be used, as it is done later in this project.

What it is important to observe is that for some pairs of halo phase and coast time, the low eccentricity zones do not contain any orbit having a ”very low eccentricity”, and therefore, cannot be used to fulfill the idea of this project.

Besides the eccentricity, the inclination of the parking orbit is also studied since it is a key factor in the launchers performance (see section 3.7). The other orbital elements are not so

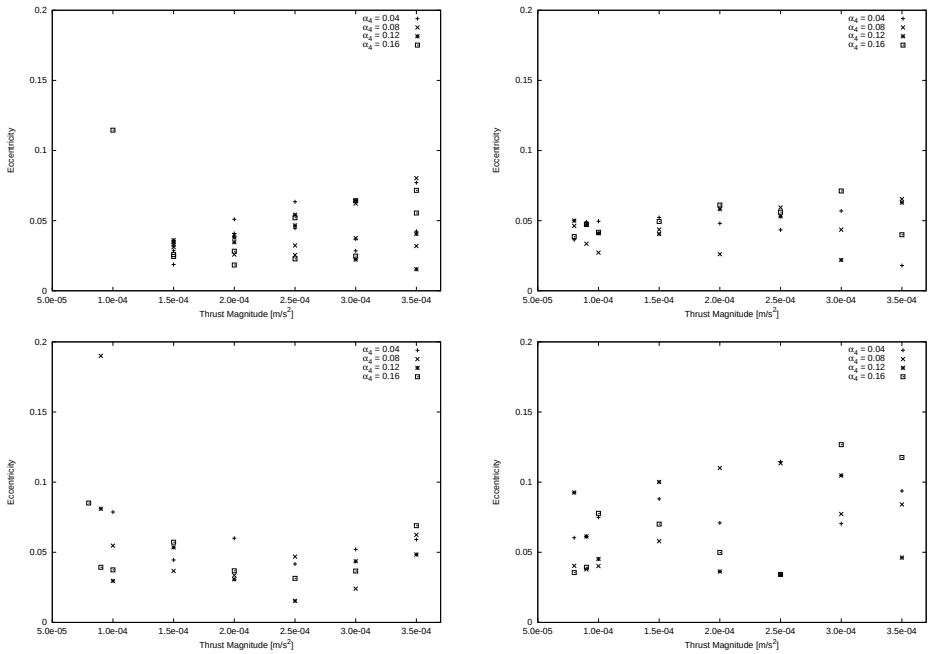

Figure 4.9: Influence of the halo amplitude and thrust magnitude on the eccentricity of the parking orbit. From right top in a clockwise direction: zone 1, zone 2, zone 3 and zone 4.

important for this first analysis: the semi-major axis is already defined from the 1000 km altitude and low eccentricity limits; the other three (longitude of the right ascension of the ascending node, longitude of the perigee and true anomaly) are not so important since we can choose launch windows satisfying them.

Figure 4.10 presents the comparison between the inclinations of the best transfers for each zone. All of them are with respect to the Earth ecliptic. Different lines correspond to different halo orbit amplitude. It is important to have in mind that the ordinary data of the launchers is with respect to the equator, as usual. Therefore, approximately 23° must be added in the present data to transform the reference from the ecliptic to the equator in order to make a comparison.

From figure 4.10, it is clear that the halo orbit amplitude plays the major role in determining the inclination of the parking orbit. Actually, form the figures we can take an approximately “rule of thumb” that an increase of 0.04 in the value of α_4 results in 1.5° increase in inclination.

Higher thrust magnitudes also cause an increase in the parking orbit inclination. This influence, however, is very small and varies between the analyzed low eccentricity zones. Zone 3 seems to be the most influenced by this effect while zone 4 looks to be the least one.

Nevertheless, the low-eccentricity zone does not seems to play a major role in the main values

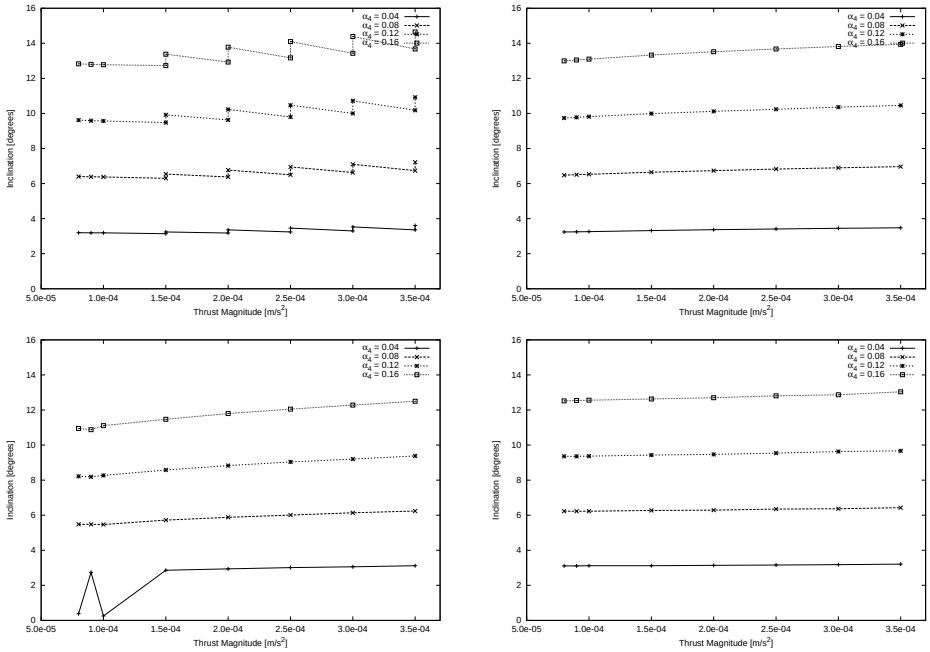

Figure 4.10: Influence of the halo orbit amplitude and thrust magnitude on the inclination of the parking orbit. From left to right and form top to bottom: zone 1, zone 2, zone 3 and zone 4.

of inclination. The two points for the higher thrust magnitudes for the zone 1 are the result of the splitting zones Z1A and Z1B. It is interesting to observe that the difference in the resulting inclinations is significant , and it increases with the halo orbit amplitude. For small thrust magnitude values when $\alpha_4 = 0.04$ the orbit inclination in zone 3 presents an erratic behavior. The reason is the scattered low eccentricity zones that are present for these values of parameters. The lowest eccentricity orbit, therefore, changes from micro-zone with the change of the parameters causing this major changes in inclination.

As explained in the last section, the main disadvantage of the low thrust transfer is the long maneuver time required. Therefore, the total transfer time is a very important parameter to be studied, and figure 4.11 presents the results.

As opposite to the results of the inclination, the halo amplitude almost does not influence the total maneuver time as can be seen in the figure. For transfers of zones 2 and 4 its influence cannot be seen and in the others the big differences only appear for low thrust magnitude values. These differences, however, are associated with higher eccentricity parking orbits, since, for these values of the parameters, no very-low-eccentricity orbit was observed.

In the other hand, a higher thrust magnitude always reduces the transfer time. Nevertheless, this reduction is not constant for all magnitudes. From the data obtained and presented here,

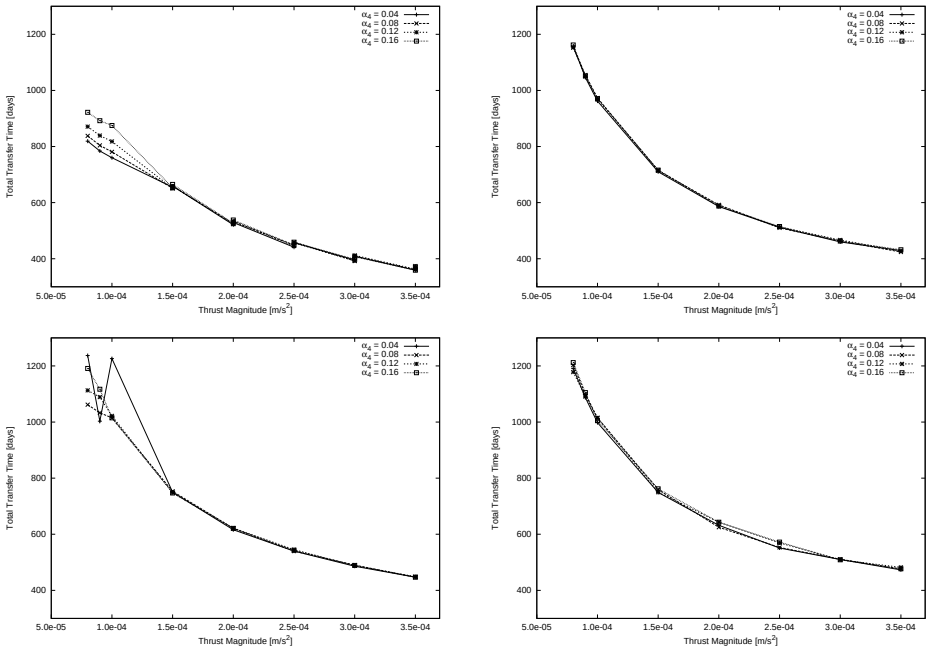

Figure 4.11: Influence of the halo amplitude and thrust magnitude on the transfer total time. From left to right and from top to bottom: zone 1, zone 2, zone 3 and zone 4.

the total transfer time seems to vary exponentially with the thrust magnitude.

From our choice of numbering the low-eccentricity zones, the ones with lowest coast time correspond to the ones with highest numbers. It is observed that the total transfer time follows this parameter, since the transfers corresponding to zone 1 are the fastest ones.

As or more important than the total transfer time, is the time of the thrusted arc, that is, the time with the propulsion system working, since its value is directly proportional to the needed propellant mass, and therefore, to the cost. The graphics with the results relative to this parameter are presented in figure 4.12.

Again in this case the halo amplitude plays a minor role in the value of the thrust time, with influence just observed in the zones 1 and 3. Moreover, the thrust magnitude also seams to influence exponentially this parameter, as it is infered from the results of the study of the total transfer time.

An interesting result arises from the comparison between thrust time for transfers of different zones. The values for zones 2 and 4 are very similar for all thrust magnitudes, while for the highest one all four zones agree well. Therefore, it can be concluded that the orbit chosen does not influence much in the cost associated with propellant. Thus, a natural choose would be for

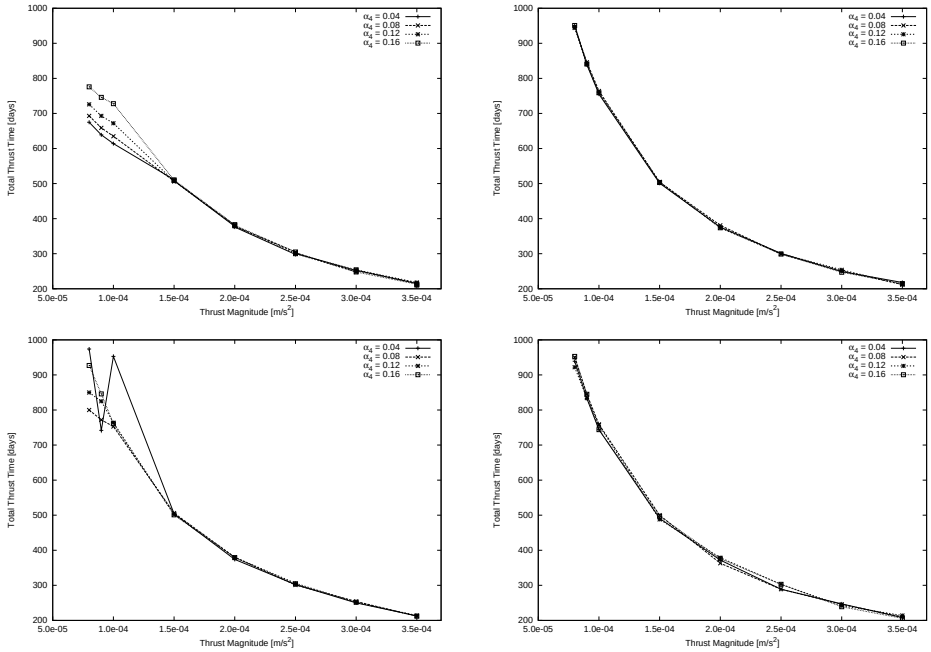

Figure 4.12: Influence of the halo amplitude and thrust magnitude on transfer thrust time. From left to right and from top to bottom: zone 1, zone 2, zone 3 and zone 4.

orbits of zone 1 since they are faster as seen above.

In order to illustrate more the results presented above, we present the spatial transfer trajectory plot of different transfers calculated. Figure 4.13 presents the comparison between transfers with different halo amplitudes (left) and different thrust magnitudes (right). Only the points closest to the halo orbit are plotted in order to maintain the figure “clean”.

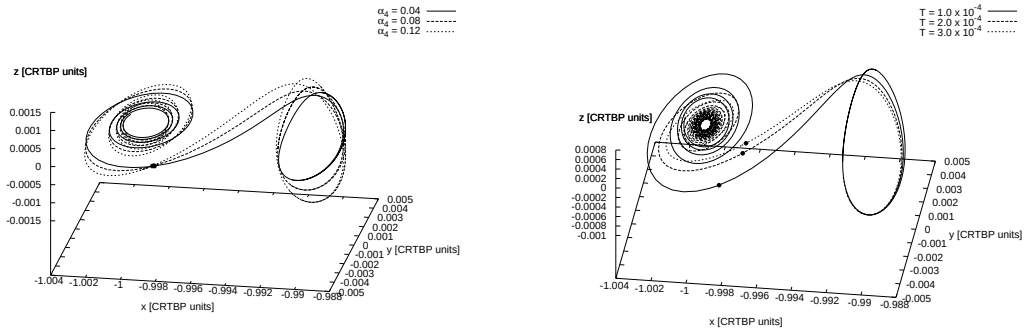

Figure 4.13: Transfer trajectory comparison, different halo amplitudes (left) and different thrust magnitudes (right)

From this figure it is clear the influence of the halo orbit amplitude in the inclination of the parking orbit. Since the halo orbit aimed is “higher” and the propulsion almost does not influences the inclination, a higher starting inclination is needed.

Analyzing the right hand side of the figure, we observe that the higher is the thrust magnitude, the closer to the Earth the spacecraft is settled in the manifold. This is due to the highest acceleration resulting from the higher thrust. If the acceleration is low, more time and spirals around the Earth are needed to the spacecraft to gain energy, thus the link with the manifold will be far from the Earth.

4.2.6 Evolution of the Orbital Elements During the Transfer

Once the main low-eccentricity parking orbit zones are determined and how they are influenced by the transfer parameters, it is investigated how the orbital elements change during the transfer. The objective is to find the influence of the manifold characteristics on the parking orbit and a behavior of it which could help control algorithms to be used in the transfer.

Figure 4.14 presents the variation of eccentricity and inclination with respect to the altitude and time. Moreover we plot the relation between themselves for one interesting transfer obtained during the last studies. Observe that the boxes present a magnification for the low altitude and low time values for a better view. The small circles once more represent the link between the thrust arc with the coast one.

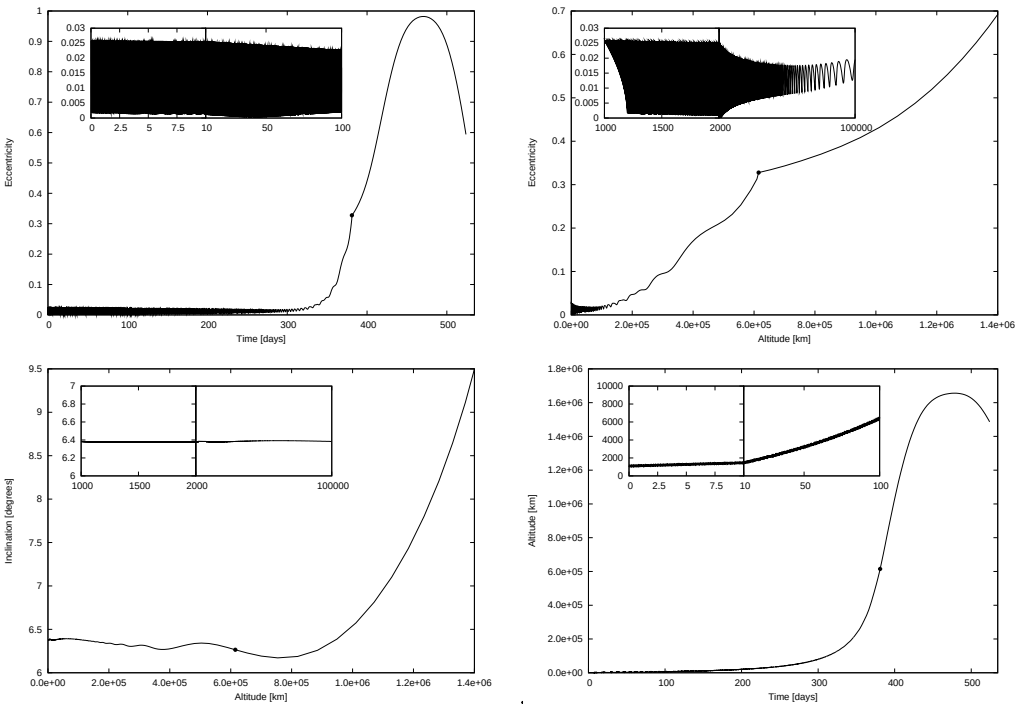

Figure 4.14: Variations of the orbital elements in the transfer associated with the lowest eccentric parking orbit. Halo orbit amplitude of $\alpha_4 = 0.08$ and thrust magnitude $F_T = 2.0 \cdot 10^{-4}[ms^{-2}]$.

The eccentricity begins with fast oscillations whose amplitude decreases with time and consequently with altitude. After some time, these oscillations disappear and the eccentricity grows exponentially with time until reaching the manifold. It is observed a not smooth transition in eccentricity from the thrust arc to the coast one, both with respect to time and altitude.

The graphic in the left bottom side of the figure presents the evolution in the inclination with respect to the altitude. It is observed that it almost stays constant until middle altitudes noticing only a low frequency oscillatory component. However, after the switching to the coast arc, it begins an exponential increase until reaching the halo orbit.

Finally, the last graphic presents the evolution of the altitude of the spacecraft with respect to time. As expected, during the thrust arc it is exponential, and later, links smoothly with the coast arc, continuing to gain altitude till the halo orbit.

In order to search for the manifolds characteristics that leads to a low eccentricity parking orbit, a different experiment was performed. Starting from a best transfer of a determined zone (i.e., the transfer associated with the lowest eccentric parking orbit), simulations with small variations of the coast time and halo orbit phase were done and the evolution of the orbital elements were plotted for comparison. An example of result of these experiments is shown in figure 4.15 where the zone chosen was the Z2 for an halo orbit of amplitude 0.08 and thrust magnitude of $2.0{\cdot}10^{-4}$ [m/s].

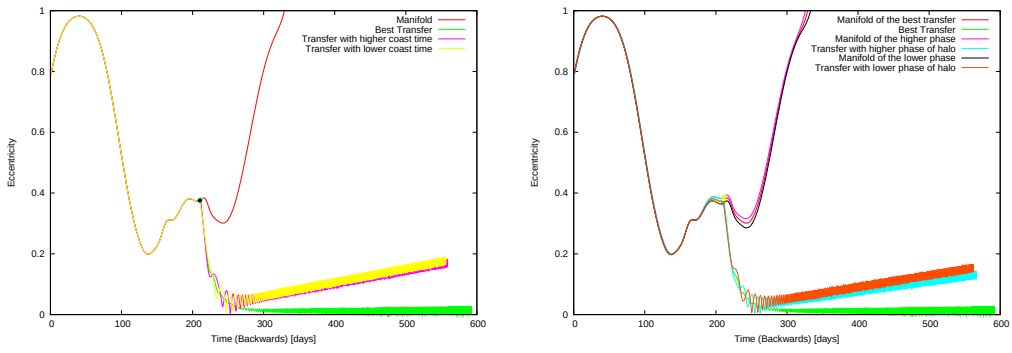

Figure 4.15: Comparison between the best transfer with ones with little different parameters. On the left the changed parameter was the coast time. On the right it was the halo orbit phase. In order to allow a better comparison, the manifolds are also presented.

It must be remembered that in this figure the time is plotted backwards. This was done because the orbits need different times to arrive to the 1000 km altitude checkpoint. The altitude could not be used in this comparison because the high eccentricities during the transfer sometimes caused the plot to go backwards and difficultting the analysis.

As it can be seen in the left hand side of the figure, even a very small change in the coast time is enough for increasing significantly the eccentricity of the parking orbit. Actually, the changes applied in this example are of 0.58 days (or approximately 14 hours) added or subtracted of the best found. These are too small gaps to allow any conclusion with respect to a characteristic of the manifold which support the low-eccentricity parking orbits.

In the case of changes in the phase of the halo orbit the same behavior happens. Nothing in the change of the orbital elements with respect to time is observed that could identify a specific characteristic of the manifold in the case of the best transfer.

Moreover, comparing figures 4.15 and 4.14, which correspond to different low-eccentricity zones, any conclusion in that sense could be taken neither. However, it is interesting to note that the manifold link point can present high eccentricities (such as 0.4 in the case of the figure 4.15) and still allow a low-eccentricity parking orbit.

4.2.7 Influence of the Check Altitude

As explained before, all results presented until now are obtained using the 1000 km altitude with respect to the Earth. The influence of this parameter in the results are studied in this section.

Several low-eccentricity transfer orbits founded in the work are analyzed computing the orbital elements at each point resulted from the integration. For each altitude, a mean value of the desired parameter was taken from a small interval of true anomaly values. This proceeding is needed since the low thrust introduces high frequency perturbations in the orbital elements as presented before.

Examples of this study are presented in figures 4.16 and 4.17. Both represents the variation of the interesting parameters with respect to the check altitude. In the first figure, the behavior for several halo orbit amplitudes are presented, while in the second are the comparison is between different thrust magnitudes.

First analyzing the eccentricity. It is observed that it tends to increase with the decrease of the check altitude. This agrees with the orbital element evolution with respect to time presented in figures 4.15 and 4.14. This increase seems to be linear and its inclination is related with the magnitude of the eccentricity. For very low eccentric orbits, in which we are interested, thus, this change is not significant.

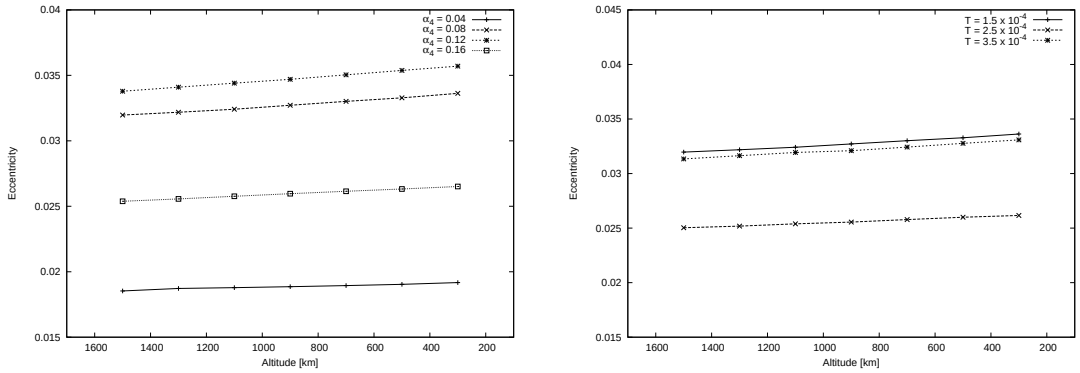

Figure 4.16: Influence of the check altitude on the eccentricity of the parking orbit obtained. In the left side different halo orbit amplitudes are tested, and in the right one, different thrust magnitudes.

The inclination can be considered constant for all the range of altitudes analyzed. This is an important conclusion since it has a great impact in the launcher performance.

Finally the total time of the transfer, and consequently the thrust time can be considered to vary linearly in the range of altitudes considered, i.e, the LEO typical altitudes. The magnitude of this variation does not seem to vary with the halo orbit amplitude, but only with the thrust magnitude. As it was expected, a bigger thrust leads to a less time difference between two transfers.

In order to compute a real mission, several tests must be done using this data and the performance data of the launcher to find the best altitude of the parking orbit, i.e., the altitude which allows the heaviest payload with the same cost.

4.3 Halo Orbits around SEL2

Basically the same tests done for the SEL1 transfers were repeated for the SEL2 ones. The results of both, however, are very similar. This fact is not completely unexpected. When the value of $\mu \rightarrow 0$ the behavior of the libration points 1 and 2 tends to be the same. The complete symmetry is obtained in the limit, known as Hill's case. Thus, in order to avoid making the report repetitive, we only present the results of the tests form SEL2 in appendix C without a deep discussion since it would be analogous to that done for SEL1.

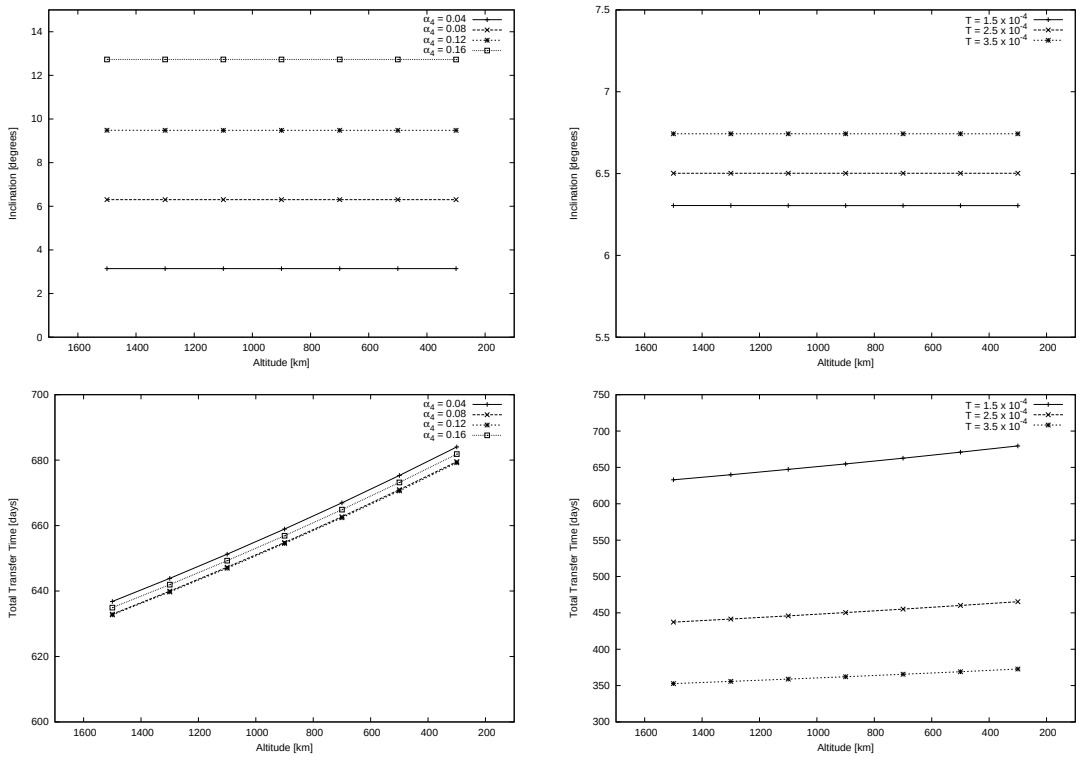

Figure 4.17: Influence of the check altitude influence on the inclination of the parking orbit and total transfer time. In the left side different halo orbit amplitudes are tested, and in the right one, different thrust magnitudes.

4.4 Effects of Changes in the Thrust Direction

Several tests were done, for both SEL1 and SEL2 transfers, variating the constrained thrust direction for small angles of about 2 degrees. The objective was making a small study of its influence in the transfer, mainly in the inclination of the parking orbit.

It is observed that this small changes do not affect the transfer significantly. This small influence was already cited in the NSTAR validation report [3], that affirms that many times during the DS1 mission the thrust was not pointed in the optimum trajectory direction without a significant penalty.

Nevertheless, more tests can be done in order to study the possibility of control of the transfer by varying the thrust vector direction.

5 The CRTBP with Near-Earth Perturbations

As explained in section 2, the circular restricted three body problem is a good model to describe the motion of a spacecraft in zones where the Sun and the Earth gravitational attraction are comparable like near the libration points.

In order to describe the small deviations from the three body orbit motion, specifically near to the Earth, we use the approach of the orbital perturbations. The idea is to add to the equations of motion some other forces that act in the spacecraft affecting its motion.

In the case of the low thrust transfers studied in this project, due to the long spiral path of the spacecraft near the Earth, the perturbing forces about the Earth are the most important to be considered. Between all of them three are the most significant

Gravitational Harmonics. The mass distribution of the Earth is not spherically symmetric and, therefore, the assumption of a point mass to derive the equations of the CRTBP is not valid. Thus, a perturbing component resulting from this non-symmetry is considered.

Atmospheric Drag. Gas atoms and molecules are present around the Earth even at high altitudes. Although the density of the flow around the spacecraft is small enough to be considered a free molecular flow, the losses of energy in a spacecraft describing a LEO can be significant, usually being the determining factor of a LEO satellite's lifetime.

Solar Radiation Pressure. The solar radiation pressure arises from the momentum transfer between the photons that collide with the spacecraft. It is an important perturbing force specially for spacecrafts that have large solar panels.

Therefore, once interesting halo transfers have been determined with the CRTBP and the thrust simple model, the following step was to study the influence of the near-Earth perturbations on them. In order to do this, the work was divided in two parts. The first one was to model the perturbations in the vectorfield, and the second was the study of their influence when acting on the interesting orbits.

5.1 The Model of the Near Earth Perturbations

Several models of the near Earth perturbations have been developed and implemented suitably for numerical integrations of the equations of motion of the spacecraft. The work done as part

of this project started from the basic study of these models and ended with the implementation and validation of a model which is in accord with the ESA and NASA advice for modeling perturbations.

A complete discussion of the nature of the perturbations, the available models, the implementation and the validation done can be found in appendix G. Only its main features will be presented here.

The basic reference used was the book of Montenbruck [15] which contains a great discussion of the nature of the perturbations, its models and implementations. Moreover, it contains functions written in C++ to model them. Although these routines are very good, they are restricted to the models used in the book and have some hypotheses implicit on them. In order to obtain a more general model, to be used in other projects with small or no changes, and to facilitate the integration with previous C and FORTRAN codes, it was decided to use them only as a guide for the new ones to be developed.

ESA has a standard (reference [6]) where it names the models that should be applied to each perturbation and also provides the ways of obtaining them. NASA, in turn, maintains a web site (reference [20]) with their public available models. The idea used in this project, therefore, was to mix all three references aiming at the best model as possible.

The gravitational harmonic coefficients used are from the model EGM96 indicated by NASA in its web page and by ESA as the near future model to be applied (the standard is from 2000). The calculation of the accelerations, however, are performed using the algorithm presented by Montenbruck.

The atmospheric density model used is the MSISE90, whose routine is provided by NASA in its web site. Once the density is calculated, the atmospheric drag is just a function of the relative velocity of the spacecraft with respect to the atmosphere and the ballistic coefficient of the spacecraft. To find the relative velocity it was used the same assumption as Montenbruck in the sense that the atmospheres co-rotates with the Earth. ESA and NASA advice the use of a high-altitude wind model, but it was considered out of the scope of our purposes. Moreover, atmospheric models for high altitudes still suffer of big differences between each other.

Finally the solar radiation pressure was modeled considering the constant solar radiation coefficient at 1 AU presented in appendix D. This was considered to be acceptable since the farther distance from the Earth considered in the work was around 0.01AU (the relative position of the libration points 1 and 2). Considering that the solar radiation is proportional to the inverse of

the square of the distance, this change is not significant for the accuracies considered in this project.

5.1.1 Integration of the Perturbing Accelerations in the CRTBP Equations

The equations of the CRTBP model are written with respect to the synodic reference system as explained in section 2. Meanwhile, the near-Earth perturbations are usually modeled with respect to a geocentric equatorial "quasi-inertial" reference system, as discussed in appendix G. Therefore, it is necessary to develop the transformation between these two reference systems in order to derive the equations of a combined model. This is the objective of this section.

The first step is concerned with the different origin of both systems, taking as reference the figure 5.1, we can easy deduce the expression

$$\vec{r}_s = \vec{r} - \vec{R} \tag{5.1}$$

where $\vec{r}$ is the position vector of the spacecraft with respect to the synodic system (with origin in the barycenter of the Sun-Earth/Moon system); $\vec{R}$ is the position of the Earth is this same system; and $\vec{r}_s$ is the position of the spacecraft with respect to a reference frame with the synodic axis but with origin in the center of the Earth.

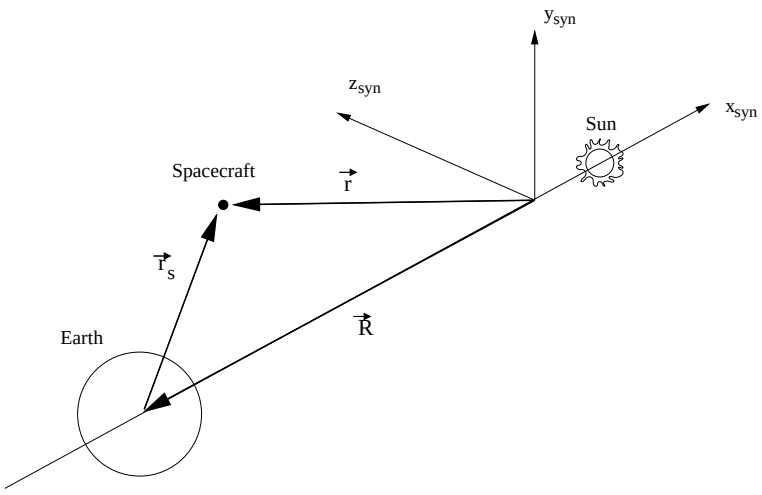

Figure 5.1: Relation between the position vectors in the synodic reference system

The next and more difficult part is to relate the vector $\vec{r}_s$ with the $\vec{r}_g$, which is the position vector of the spacecraft with respect to the geocentric equatorial frame. This relation involves two rotations and one scale factor, mathematically

$$\vec{r}_s = k\mathbf{M}\vec{r}_g \tag{5.2}$$

where k is the scale factor and $\mathbf{M}$ is an orthogonal rotation matrix.

The scale factor k is needed since the synodic reference system used is dimensionless, while the position vector in the geocentric equatorial system has the unit of meters. As previously explained, the scale factor used in the Sun-Earth/Moon system is the *Astronomical Unit* which is the mean distance between the Earth and the Sun. Thus

$$k = \frac{1}{1AU} = \frac{1}{1.49597870691 \cdot 10^{11}} \text{ (see appendix D)} \tag{5.3}$$

The deduction of an expression for the matrix M is done with help of the figure 5.2. It can be observed that the relation between the geocentric equatorial and the synodic axes (represented with subscripts ($_g$) and ($_s$) respectively is made with two angles: the obliquity of the ecliptic ε and the mean ecliptic longitude of the Sun $L_\odot$.

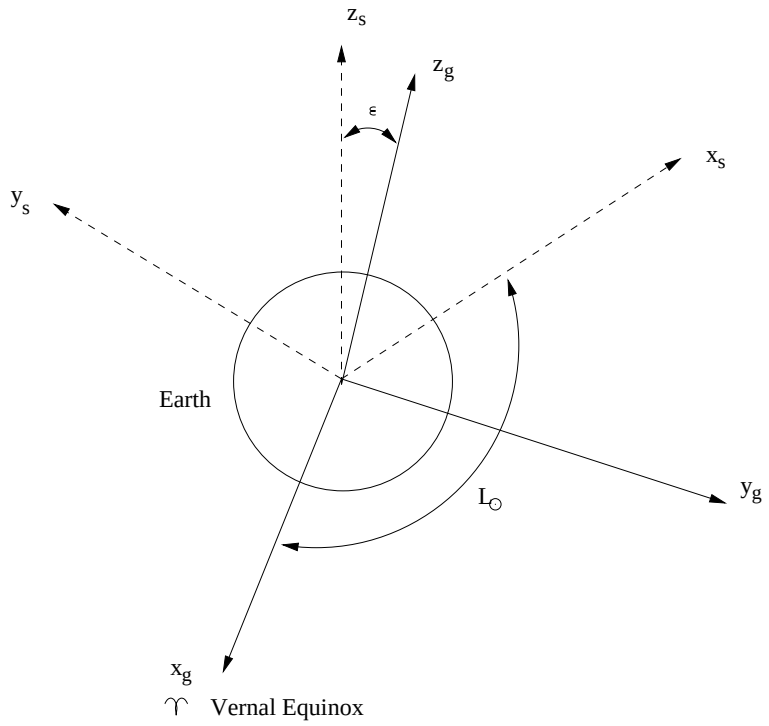

Figure 5.2: Relation between the position vectors in the synodic reference system

Therefore, the matrix M can be expressed by

$$\mathbf{M} = \mathbf{R_z}(L_\odot)\mathbf{R_x}(\varepsilon) \tag{5.4}$$

i.e, a rotation around the x_g axis of ε, followed by a rotation of $L_\odot$ around the z_g axis. The

matrixes are expressed by

$$\mathbf{R_z}(L_\odot) = \begin{pmatrix} +\cos L_\odot & +\sin L_\odot & 0 \\ -\sin L_\odot & +\cos L_\odot & 0 \\ 0 & 0 & 1 \end{pmatrix} \quad \text{and} \quad \mathbf{R_x}(\varepsilon) = \begin{pmatrix} 1 & 0 & 0 \\ 0 & +\cos\varepsilon & +\sin\varepsilon \\ 0 & -\sin\varepsilon & +\cos\varepsilon \end{pmatrix} \tag{5.5}$$

In order to find the relations between the velocities vectors in both frames, the equation 5.2 must be derived with respect to the time t. A small but important fact must be observed in this derivation: the time t of the synodic system is dimensionless, while the time t^* of the geocentric equatorial system has the dimension of the SI second. The relation between both was given in appendix B, and is copied here

$$t = nt^* \tag{5.6}$$

where n is the mean motion of the primaries. For the Sun-Earth/Moon system this value is presented in appendix D.

Therefore, the first time derivative of equation 5.2 is

$$\begin{aligned} \frac{d\vec{r}_s}{dt} &= \frac{dt^*}{dt}\frac{d}{dt^*}\left(k\mathbf{M}\vec{r}_g\right) \\ \frac{d\vec{r}_s}{dt} &= \frac{1}{n}\left(k\frac{d\mathbf{M}}{dt^*}\vec{r}_g + k\mathbf{M}\frac{d\vec{r}_g}{dt^*}\right) \end{aligned} \tag{5.7}$$

The last step is to develop the derivatives of the matrix $\mathbf{M}$. The values of $L_\odot$ and ε can be expressed by (see [14])

$$L_\odot = 280^\circ.46645 + 36000^\circ.76983T + 0^\circ.0003032T^2 \tag{5.8}$$

$$\varepsilon = 23^\circ 26' 21''.448 - 46''.8150T - 0''.00059T^2 + 0''.001813T^3 \tag{5.9}$$

both of them with respect to the mean equinox of the date. The variable T is the time measured in Julian centuries from the epoch J2000.0 in ephemeris time, i.e,

$$T = \frac{JDE - 2451545.0}{36525} \tag{5.10}$$

From these expressions, it can be observed that the variation of the $L_\odot$ is much bigger than the one of the ε. Moreover, only the linear term of the expression of $L_\odot$ is significant while time intervals of only few months are considered, as in the case of this work. Therefore two assumptions will be done in order to develop the time derivatives of $\mathbf{M}$:

1. The value of ε is considered constant with time;

2. The value of $L_\odot$ is considered to have a linear variation with time [4]:

$$\frac{dL_\odot}{dt^*} = 36000^\circ.76983[\text{Julian century}^{-1}] = 1.991063854 \cdot 10^{-7}[\text{s}^{-1}] \tag{5.11}$$

Thus, the time derivative of the matrix $\mathbf{M}$ can be expressed by

$$\frac{d\mathbf{M}}{dt^*} = \frac{d\mathbf{R_z}(L_\odot)}{dt^*}\mathbf{R_x}(\varepsilon) \tag{5.12}$$

Finally the time derivatives of the matrix $\mathbf{R_z}(L_\odot)$ are given by

$$\frac{d\mathbf{R_z}(L_\odot)}{dt^*} = \frac{dL_\odot}{dt^*}\begin{pmatrix} -\sin L_\odot & -\cos L_\odot & 0 \\ +\cos L_\odot & -\sin L_\odot & 0 \\ 0 & 0 & 0 \end{pmatrix} \tag{5.13}$$

(5.14)

Once all basic vectors relations have been developed, we can explain how the integration between both models was done. The equations of the motion are basically derived from the application of the Second Law of Newton with respect to an inertial coordinate system, i.e., for the model used until now

$$\frac{d^2\vec{r}_{sid}}{dt^*} = \mathbf{CRTBP}_{sid}\left(t^*, \vec{r}_{sid}\right) + \mathbf{THRUST}_{sid}\left(\vec{r}_{sid}, \frac{t^*, d\vec{r}_{sid}}{dt^*}\right) \tag{5.15}$$

Where $\mathbf{CRTBP}$ and $\mathbf{THRUST}$ are the accelerations due to the Earth + Sun (non inertial) and low thrust respectively. Their inputs are presented inside the parenthesis and their outputs must be written in the sidereal system, as expressed by the $_{sid}$ in the equation.

However, it is interesting to work in the synodic coordinate system, therefore, the hole equation 5.15 was transformed to this system. As the synodic system is not a inertial reference system, the acceleration vector must be transformed taking into account the movements of one frame with respect to the other.

The transformations of the CRTBP force function (see appendix B) and thrust function (see section 3) were made in such a way that the accelerating equations $\mathbf{CRTBP}$ and $\mathbf{THRUST}$ were already written in the synodic system. Therefore the vectorial camp used has the form:

$$\begin{aligned} \frac{d^2\vec{r}_{syn}}{dt} &= \mathbf{CRTBP}_{syn}\left(t, \vec{r}_{syn}\right) + \mathbf{THRUST}_{syn}\left(t, \vec{r}_{syn}, \frac{d\vec{r}_{syn}}{dt}\right) \\ &\quad + \mathbf{REFCORRECTION}_{syn} \end{aligned} \tag{5.16}$$

[4] It is important to remember that the SI second is defined with respect to the TAI second and it is equal to one Ephemeris Time second

Now we want to add the factor corresponding to the near Earth perturbations. The equation 5.15 must be rewritten as

$$\begin{aligned}\frac{d^2\vec{r}_{sid}}{dt^*} &= \mathbf{CRTBP}_{sid}\left(t^*, \vec{r}_{sid}\right) + \mathbf{THRUST}_{sid}\left(t^*, \vec{r}_{sid}, \frac{d\vec{r}_{sid}}{dt^*}\right) \\ &\quad + \mathbf{EARTHPERT}_{sid}\left(t^*, \vec{r}_{geo}, \frac{d\vec{r}}{dt^*}\right)\end{aligned} \tag{5.17}$$

Again, applying the transformations from the sidereal to the synodic coordinate system for this equations we will have:

$$\begin{aligned}\frac{d^2\vec{r}_{syn}}{dt} &= \mathbf{CRTBP}_{syn}\left(t, \vec{r}_{syn}\right) + \mathbf{THRUST}_{syn}\left(t, \vec{r}_{syn}, \frac{d\vec{r}_{syn}}{dt}, \right) \\ &\quad + \mathbf{EARTHPERT}_{syn}\left(t^*, \vec{r}_{geo}, \frac{d\vec{r}}{dt^*}\right) + \mathbf{REFCORRECTION}_{syn}\end{aligned} \tag{5.18}$$

Comparing equation 5.18 with 5.16 we observe that only one term must be added, that is the component due to the near Earth perturbations in the synodic reference system. Although it has the units of acceleration it is *not* equal to the acceleration of the spacecraft, it is only a part of it.

Since one of the objectives while modeling the near Earth perturbations was to obtain a multiple purpose model, the routines were made to receive as inputs the values with respect to the geocentrical equatorial quasi-inertial system and give the output also with respect to it.

Thus, the first thing to integrate it to the previous vectorial camp is to convert its inputs (spacecraft position, velocity and time) from the synodic to the geocentrical quasi-inertial frame. This is easily done with the equations deduced in this section.

The second part is to transform the outputs back to the synodic coordinate system. As explained, they have units of acceleration, however, since it is not the acceleration vector, the corrections due to the non-inertial frame must not be done again since they were already part of equation 5.18. Thus the transformation can be done easily by

$$\mathbf{EARTHPERT}_{syn} = \frac{k}{n^2}\mathbf{M} \cdot \mathbf{EARTHPERT}_{geo} \tag{5.19}$$

Although this can seems strange in the beginning, several testes were performed to assure the transformations were correct. The basic idea was to run LEO orbits with the deduced vectorfield without thrust and compare it with a two body problem camp only. Since the spacecraft is always very near to the Earth, the results must be very similar. These tests proved that the relation between both reference systems was well done.

5.1.2 Parameters Defining the Spacecraft

With exception of the gravitational harmonics, the other two near Earth perturbation forces considered in this work are dependent of specific spacecraft parameters that have not been used until now. These parameters are difficult to be estimated accurately even at late stages of a mission design. Considering this and the fact that we are more interested in the qualitative effects of the perturbations, most of them are estimated following the principles discussed below.

The atmospheric drag acceleration is a function of the spacecraft mass (m), cross-sectional area (A) and drag coefficient (C_D). The first is the most easy parameter to obtain. The cross-sectional area is a function of the spacecraft attitude but can be considered constant. The drag coefficient, however, is very difficult to be determined. Usually it is only estimated from historical data and precisely obtained only when the spacecraft is launched.

These three parameters, however, are usually combined in only one known as *ballistic coefficient* defined as

$$B = \frac{mg_0}{C_D A} \tag{5.20}$$

where g_0 is the constant mean Earth gravitational acceleration at sea level.

For the simplified solar radiation pressure model used in this project, only three parameters from the spacecraft are needed: its mass, its mean cross-sectional area and its radiation pressure coefficient (C_R). The last one takes into account the radiation absorption by the spacecraft and varies from one to two. More details can be found in appendix G.

The first idea was to use parameters from typical spacecraft already in operation. Nevertheless, obtaining these data is not an easy task, only the value of masses and of the three dimensions are public available for almost all spacecrafts.

The cross-sectional area can be estimated from the three dimensions but it is important to take into account the solar panels that should have a considerable size due to the electric low thrust propulsion. Observe that we only use one value of area for both forces. This is not rigorously right, but can be assumed for the level of accuracy wanted in this project.

The other two parameters, the drag coefficient and the solar radiation coefficient are more difficult to be obtained. For all Earth orbiting satellites, its is available in internet a set of orbital parameters in the form known as *two-line element set*. This set contains a modified version of the ballistic coefficient. Nevertheless, this parameter is dependent of the atmospheric model

used by the NORAD SGP4/SDP4 orbital model (see [11]). Detailed explanation of how to transform the parameter to the atmospheric model desired is also available. Due to this complicator factors, for this project we decided to run the simulations with a standard drag coefficient of 2.3, following advises from Montenbruck (see [15]) and Chobotov (see [5]).

A standard value of 1.0 was taken to the radiation pressure coefficient, which means that the spacecraft absorbs all the photons that collides with it. This hypothesis was done since most of the cross-sectional area represents the solar panels. As will be discussed later, some tests were done variating these parameters (radiation and drag coefficient) looking for the impact in the transfer.

5.2 Results of the Impact of the Perturbations on the Halo Transfers

Since the results of transfers to SEL1 or SEL2 halo orbits were found to be very similar with the CRTBP simple model, we choose to present the results for both transfers together in this section. Thus we focus the discussion in the influence of each of the perturbing forces in the transfers.

Two important observations must be done about the results presented in this section. First all the inclination values are with respect to the equatorial plane and not to the ecliptic as in the previous sections. The second one is about the check altitude. Since the gravitational and atmospheric perturbations are a function of the distance to the Earth, we reduce the standard check altitude from 1000km to 500km looking for a better study of their impacts over the transfer.

5.2.1 First Results

In order to have an overview of the influence of the perturbations, the first test has been a scan over all the halo phase - coast time surface. This scan was made with each perturbing force separately and also with all of them combined, and for various values of halo orbit amplitude and thrust magnitude.

As explained before, our first interest is in transfers with low eccentricity parking orbits. Figure 5.3 presents the graphic with the difference between the parking orbit eccentricity including or not the perturbing forces.

From this figure we observe that there is no new low eccentricity zone that appears or disap-

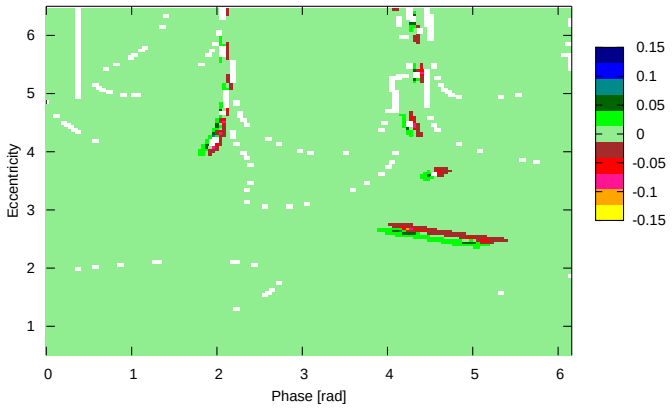

Figure 5.3: Difference between parking orbits eccentricity of the transfers computed with and without the perturbation forces ($e_{without} - e_{with}$). Data for a halo orbit amplitude of 0.04 and a thrust magnitude of 2.0·10^{-4}. Ballistic coefficient $B = 1636[Nm^{-2}]$ and area/mass ratio $A/m = 384[kgm^{-2}]$. Spacecraft parameters based on a big spacecraft.

pears, but actually their position is changed, mainly with respect to the halo orbit phase. It can be seen the increase in the parking orbit eccentricity at the previous (without perturbations) zones, and its decrease in zones immediately at the right side of the graphics.

Once this change was noted, we started to look for the responsible perturbing force. Since we scanned with all of them separately this was easily done. Gravitational harmonics and atmospheric drag have shown to have very little or none influence on the eccentricity of the parking orbit, the changes was, therefore, results of the solar radiation pressure. This was somewhat expected from the theory of perturbations, and will be discussed in the next subsections more deeply.

The points not colored in figure 5.3 are associated with the boundary of the regions were we had the thrust problems or not converging transfers (the ones that does not reach the Earth after long time). The perturbations move these boundaries causing great changes in the eccentricity of the parking orbits associated with these transfers. These changes, however, are not interesting for the project since no interesting transfer near them was observed.

Other two important characteristics of the transfer are its total time and the inclination of the parking orbit. Figure 5.4 presents the results for both of them related with the same conditions used in figure 5.3.

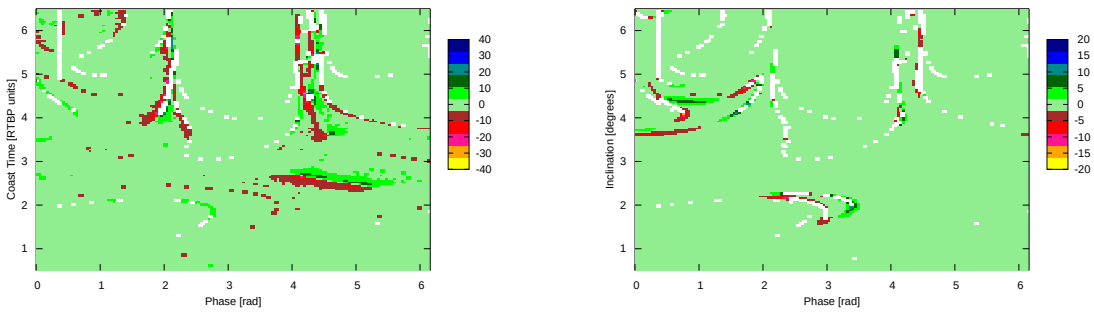

Figure 5.4: Difference between total transfer time (in days, left) and parking orbits inclination (in degrees, right) of the transfers computed without and with the perturbation forces. Data used are the same of figure 5.3.

Considering the total time of the transfer, it is directly related to the thrust time since the coast time is also defined. From these figures we can basically only observe variations related with the parking orbit eccentricity changes. The more circular is the parking orbit, more time is needed to the transfer, therefore, it was expected the variations in the transfer time near the low eccentricity parking orbit.

About the inclination plot, we observe no significant changes in the inclination of the parking orbit for the low eccentricity ones. The big changes are, again, associated with the boundaries of the problematic zones and are not relevant to this project.

5.2.2 Gravitational Harmonics

Starting the study of the influence of each of the perturbative forces by the gravitational harmonics, no big influence in eccentricity or inclination of the halo orbit is noted in the first overview. This was expected since the major influence is to introduce secular variations in the right ascension of the ascending node and in the argument of perigee, both not so important for the purpose of this project. Since the gravitational harmonic forces are not function of any of the spacecraft parameters, there is no need of further study impact in different spacecrafts. However we can study the impact of considering a bigger or lower number of harmonics to be included in our model.

Table 5.1 presents the comparison between the parking orbit elements and transfer times when the gravitational model is introduced and more of its factors are considered. As it was expected, the term J_2 has the biggest impact, being the main responsible for the regression of the line of

the nodes (see appendix G). Inclusion of more terms in the series does not cause great impact on it. Only a small change is observed in the argument of the perigee.

Table 5.1: Influence of gravitational harmonics in the best transfer obtained for a SEL1 halo orbit amplitude $\alpha_4 = 0.12$ and thrust magnitude of $F_T = 1.0 \cdot 10^{-4}[ms^{-2}]$ (halo phase $\phi = 4.055[rad], t_{coast} = 144[days]$)

Grav. Harm.		Parking Orbit Orbital Elements					Transfer Time	
Zonal	Tesseral	Eccentricity [degrees]	Inclination [degrees]	Right. Ascending [degrees]	Arg. Perigee [degrees]	True Anomaly [degrees]	Total [days]	Thrust [days]
0	0	0.02452	30.2	-18.6	133.4	5.6	421.7	263.7
2	0	0.02534	30.2	-147.6	127.0	4.9	421.6	263.6
2	2	0.02534	30.2	-147.6	126.8	4.8	421.6	263.6
3	3	0.02541	30.2	-147.6	127.7	6.1	421.6	263.6
4	4	0.02541	30.2	-147.3	127.4	6.1	421.6	263.6
20	20	0.02542	30.2	-147.3	127.7	6.2	421.6	263.6

It is also observed in this table a very small increase in the halo orbit eccentricity when we use more complex models. From the theory of perturbations for the two-body problem, we know that the gravitational harmonics do not cause secular changes on it. Thus, we believe that this changes are related to low amplitude high frequency oscillatory components resulting from these perturbations.

Also no significant difference in the transfer time was observed. Actually there was a very small reduction in time when the gravitational harmonics were considered, but without any practical application.

In order to compare the results, table 5.1 presents the same study but for a SEL2 transfer using the low eccentricity zone 4 and a smaller thrust magnitude. The idea was verify any different behavior in a longer transfer even if does not have practical interest.

Table 5.2: Gravitational harmonics influence in the best transfer obtained for a SEL2 halo orbit amplitude of $\alpha_4 = 0.04$ and thrust magnitude of $F_T = 8.0 \cdot 10^{-5}[ms^{-2}]$ (halo phase $\phi = 1.180[rad], t_{coast} = 259[days]$)

Grav. Harm.		Parking Orbit Orbital Elements					Transfer Time	
Zonal	Tesseral	Eccentricity [degrees]	Inclination [degrees]	Right. Ascending [degrees]	Arg. Perigee [degrees]	True Anomaly [degrees]	Total [days]	Thrust [days]
0	0	0.03525	25.2	-6.3	-68.2	4.0	1050.9	791.6
2	0	0.03658	25.2	-31.0	178.6	-2.7	1050.6	791.3
2	2	0.03660	25.2	-31.0	178.3	-3.1	1050.6	791.3
3	3	0.03688	25.2	-31.8	179.0	-2.3	1050.4	791.3
4	4	0.03688	25.2	-30.8	177.6	-2.5	1050.4	791.1
20	20	0.03688	25.2	-30.7	177.4	-2.5	1050.4	791.1

Observing the table the only change from the previous one are that the differences between the use of more coefficients becomes more evident, but they are still very small to be significant to the transfer. Moreover, as discussed before, changes in the ascending node and argument of

perigee can be obtained by the choice of the launch date.

In order to illustrate better this results, figure 5.5 presents the variation of the orbital elements for the same transfer studied in table 5.1. A first observation is that the results with a gravity model of order 2x0 is almost the same as 4x4, thus both are almost always overlapped in the graphics.

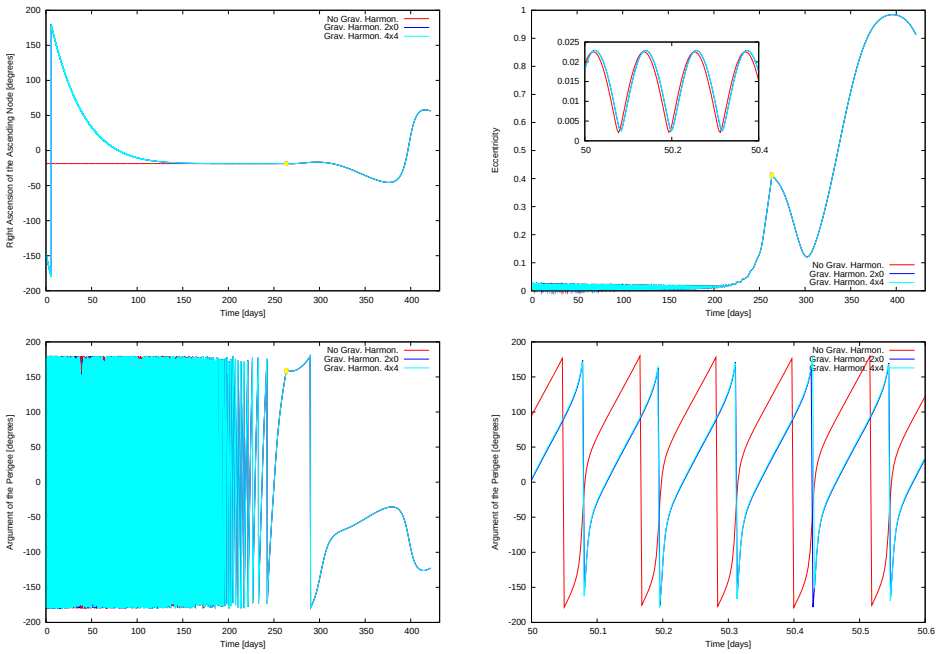

Figure 5.5: Evolution of the orbital elements with time for the same transfer of table 5.1

About the ascending node, it is clear the great influence of the gravitational harmonic J_2. Moreover, it can be observed the decrease in its influence with distance. Although the graphic is with respect to time to be better visualized, it is clear the non linearity of the curve.

The eccentricity difference can be visualized in the zoom shown in the respective plots. It can be seen clearly the big difference in phase of the oscillations and the small in eccentricity. Finally the perigee behavior that was not illustrated as we guessed in the previous table is explained by the graphics. Due to the low thrust, it has a very large amplitude oscillatory behavior that imposes itself over the small perturbations coming from the gravity harmonics. The graphic in the left bottom side of the figure presents a zoom, so this behavior can be better visualized.

Thus we can conclude that the gravitational harmonics should be considered mainly in order to have a more realistic value for the right ascension of the ascending node of the parking orbit. Moreover, it can slightly affect the eccentricity of it.

5.2.3 Atmospheric Drag

The atmospheric drag acts on the spacecraft as a force opposite to the thrust, but with magnitude that varies approximately exponentially with altitude. The ”rule of thumb” from the literature says that it should be considered for orbits below 1000 km of altitude. This was one of the main reasons of the change to 500 km of the check altitude used in this part of the work.

Following the same method used in the study of the influence of the gravity harmonics, starting from a good transfer obtained with the CRTBP model, we make several simulations with different ballistic coefficients. Table 5.3 presents the result for one of this orbits.

Table 5.3: Influence of the atmospheric drag in the best transfer obtained for a SEL2 halo orbit amplitude $\alpha_4 = 0.04$ and thrust magnitude of $F_T = 2.5 \cdot 10^{-4}[ms^{-2}]$ (halo phase $\phi = 1.000[rad], t_{coast} = 159[days]$

Ballistic	Parking Orbit Orbital Elements					Transfer Time	
Coefficient	Eccentricity	Inclination	Right. Ascending	Arg. Perigee	True Anomaly	Total	Thrust
$[N.m^{-2}]$	[degrees]	[degrees]	[degrees]	[degrees]	[degrees]	[days]	[days]
∞	0.02228	25.1	-7.4	100.4	3.6	476.0	317.3
$4.0 \cdot 10^3$	0.02228	25.1	-7.4	100.4	3.6	476.0	317.3
$4.0 \cdot 10^2$	0.02229	25.1	-7.4	100.2	3.4	476.0	317.3
$4.0 \cdot 10^0$	0.02277	25.1	-7.4	101.7	4.9	476.1	317.4
$4.0 \cdot 10^{-1}$	0.02896	25.1	-7.4	99.9	6.2	477.2	318.5

It can be observed that a wide range of order of magnitude of the ballistic coefficient were tested. The value ∞ represents no influence of the atmospheric drag in the spacecraft, thus, the less is the value more the spacecraft is affected by drag.

It is interesting to observe that the most affected parameter from our analysis is exactly the eccentricity of the parking orbit, which increases with the increase of the ballistic coefficient. This is somehow expected since we do the integration backwards. The atmospheric drag tends to make an orbit more circular at each revolution (see appendix G). Thus, if our satellite is with a given eccentricity at a specific altitude after some time, the more is his ballistic coefficient, more is the eccentricity of its starting orbit.

The transfer time, that was expected to vary significantly do not present great changes also. Even with our lowest value of ballistic coefficient, which is already very low for practical purposes, the total and thrust time just increased by 1.1 days. A possible explanation is the high altitudes involved in the work. Even 500km is still high to get significant atmospheric drag.

To compare the evolution of the parameters with time, figure 5.6, presents the variation of eccentricity and altitude for different values of ballistic coefficient.

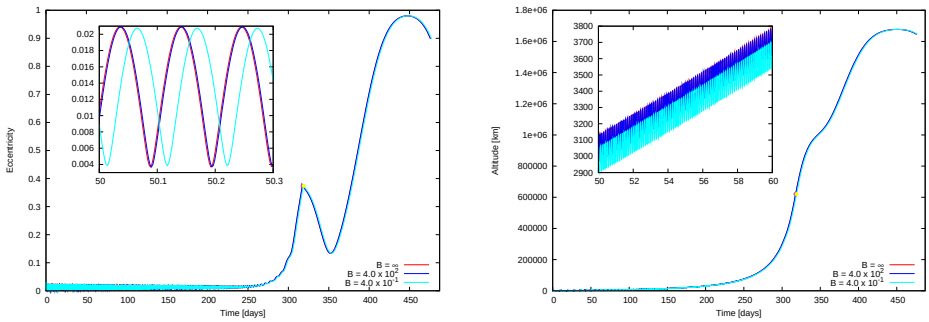

Figure 5.6: Evolution of the orbital elements with time for the same transfer of table 5.3

From this graphic of eccentricity we can note that the increase in the ballistic coefficient reduces the amplitude of the oscillations, although this reduction is very small. From the altitude graphic it is clear the effect of the drag reducing the acceleration of the spacecraft and therefore its altitude for the same time.

Thus, the atmospheric drag should be considered specially when determining the optimum altitude for the parking orbit. It even establishes a minimum limit to this altitude, since for a certain value, the atmospheric drag acceleration becomes bigger that the low-thrust one.

5.2.4 Solar Radiation Pressure

The major influence of the solar radiation pressure was already seen in the first overview test with the perturbations. It is the change in the position of the low eccentricity parking orbit zones in the halo phase - coast time surface.

Figure 5.3 was enough to verify this consequence, but in order to study it a little more deeply and also study the influence of the spacecraft parameters, the scan was repeated for different low eccentricity zones only and with different values of the spacecraft parameters.

As discussed before and deeply on appendix G, the solar radiation pressure acceleration is a function of the area/mass ration of the spacecraft and the radiation coefficient. The last one had its value fixed to 1.0 due to the major contribution of the solar panels. Thus, the parameter we vary in the tests studies is the area/mass ratio.

One example of this study is the figure 5.7. Three scans with different area/mass ratio are presented in order to be compared.

It can be noticed that the shift of the low eccentricity zone seams to be in the top right direction,

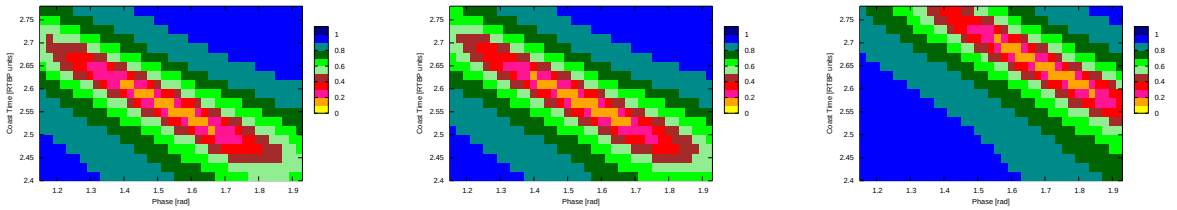

Figure 5.7: Changes in the low eccentricity zone 1 of a SEL2 transfer for $\alpha_4 = 0.04$ and $F_T = 1.0 \cdot 10^{-4}[ms^{-2}]$ due to the solar radiation pressure. For all of them $C_R = 1.0$. At the left $A/m = 0$, at the center $A/m = 1/300$ and finally at the right $A/m = 1/30$ [m^{2}kg^{-1}]

that is, an increase in both halo phase and coast time.

The effect of the solar radiation can also be studied by observing the variation of the eccentricity with respect to time along the transfer orbit for different values of area/mass ratio. One of the results of these studies is presented in figure 5.8.

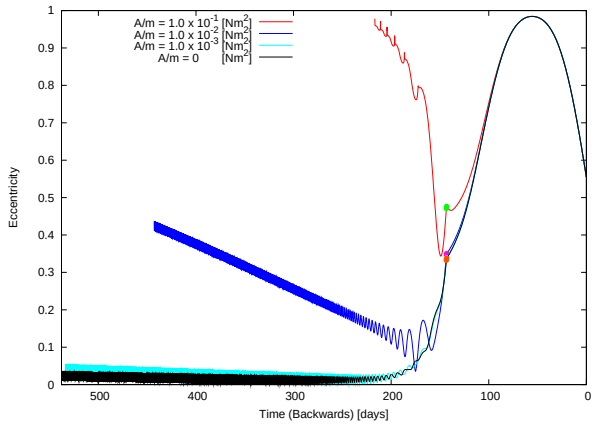

Figure 5.8: Comparison between the evolution of the eccentricity along the transfer orbit for different values of the area/mass ratio. The transfer considered was the best of zone 1 for SEL1 with thrust magnitude $F_T = 2.0 \cdot 10^{-4}[ms^{-2}]$ and halo amplitude $\alpha_4 = 0.12$

From this figure its is clear one important difference of the solar radiation pressure with respect to the other perturbations. As it is not a function of the distance between the spacecraft and the Earth, it acts over a long time period, even modifying the behavior of the manifold significantly when the area/mass ration is big enough.

Since it only shifts the zones, without changing it significantly the solar radiation pressure must be taken into account in a more precise orbit determination. Nevertheless, it has been not proved to be responsible for significant losses in transfer time or fuel consumption needed to accomplish the mission.

6 The JPL Ephemerides Model

Once interesting transfers has been studied with the CRTBP model with and without the near Earth perturbation forces, the next step was the study of transfers with the most complex dynamic model available, i.e., using the JPL Development Ephemeris (DE403 in this case). This section is dedicated to explain how the halo orbits and manifolds are obtained in this new model and the results of testing the previously obtained transfers in it.

6.1 The Time Dependence and the Influence of the Moon

The use of the JPL Ephemerides model has two major differences with respect to the first one: its time dependence and the influence of the Moon.

The simple CRTBP model, even perturbed by the low thrust is *autonomous*, i.e., its differential equations are not a direct function of the time but only of the position of the spacecraft. Thus, the absolute value of the time is meaningless, i.e., the halo orbit and its manifold is determined only by the position and velocity vectors. The time is only represents interval between two different states.

When the Earth perturbations were considered, the system is no longer autonomous. The dependence comes from the orientation of the Earth needed to calculate the influence of the gravitational harmonics and the seasons considered by the atmospheric density model used. Nevertheless, since these perturbations are of small magnitude, the dependences are also very small, and no real study of them was considered of great importance in this project.

In the case of the JPL ephemeris the situation changes deeply. The relative position of all the bodies of the solar system depends on the time and, therefore, so the equations of the motion. Thus, a system state is defined by the position and velocity angle and the corresponding time value. This has a great impact in our considerations. The periodic halo orbit, for example, is changed to a quasi-periodic orbit in the new system as will be seen lately.

The second difference is that the acceleration contributions due to the Earth and Moon are taken into account separately, while in the previously used models, the barycenter of both was being used as a point mass.

This fact has strong consequences in the analysis. The Moon's orbit is approximately at one third of the distance between a LEO and the halo orbits around SEL1 and SEL2. Its gravitational

force, as others, is inversely proportional to the square of the distance between it and the spacecraft. Thus, if the spacecraft passes near the Moon its attraction can easily becomes the major term of the equations of the motion. In these cases the result would be completely different from those obtained with the CRTBP model.

The idea of using the simplest models previously was that, knowing that the Moon performs orbits with approximately 28 day period around the Earth, we could choose a date of the transfer so that the spacecraft does not approach to it. Nevertheless, the influence of the Moon can have positive points to the mission, helping it in accelerating the spacecraft and in direction change maneuvers.

Although the Moon's orbit is subject to regression of nodes and perturbations mainly due to the Sun's gravitational attraction, we focused the study only in a month period. This is enough to observe the strongest influences in the interesting transfers.

6.2 The JPL Ephemeris Model

6.2.1 Introduction to the JPL Ephemerides

When high precision trajectories are needed, the best way of modeling the gravitational field inside the solar system is taking into account the contribution of all the biggest masses. That is, the Sun, all the planets and the Moon in the case of orbits near to the Earth. All of them are considered point masses in the first approach.

In order to do so, the position of all these bodies with respect to the time must be accurately known. To this end we use a JPL Development Ephemerides file of records. They are the standard reference for high-precision planetary and lunar coordinates and are also public available.

The ephemerides are calculated with a rigorous numerical integration of the respective equations of the motion. Besides the point masses interactions between the main bodies, it takes into account perturbations from other selected bodies (such as other moons and asteroids), lunisolar torques on the figure of Earth, relativistic corrections, and other factors (see [15]).

Since it covers a large interval of time, usually a thousand of years, a compact representation of data must be used in order to reduce the amount of memory occupied by them. This is accomplished by the use of the Chebyshev polynomials. The time interval is divided in arcs, each one covering a fixed time interval (usually of 32 days) and for each one the coefficients of

a Chebyshev polynomial expansion for the bodies of the solar system are given.

6.2.2 Determination of the Halo Orbit and Stable Manifold in the JPL model

When the complete ephemerides model is considered the Halo periodic orbit does not exists anymore due to the perturbations of the other solar system bodies. It is replaced by a quasi-periodic orbit that resembles it. Similarly, its stable manifold also must be determined again taken into account these perturbations. For this work we basically use the subroutines and methods described in reference [9]. This subsection presents a small summary about it.

First step is determination of the halo orbit from the CRTBP model. Then, a quasi-periodic orbit of the real solar system, i.e. using the JPL ephemerides DE403 is computed by means of a parallel shooting procedure. This is accomplished by the program `GQPTPS` that receives as one of its input the desired halo orbit amplitude and the initial epoch. Its output are the epochs in various time formats, the normalized position and velocity, and the variation matrixes at each of these intervals of the parallel shooting.

With these results, the next step is the obtaintion of the local approximations of the stable manifold near the selected quasi-periodic halo orbit. In order to do so, we use the program `VECSWS`. It reads the output of the previous program and asks among other inputs, the desired revolution to be used and the number points to be calculated. Following advises from the program developers we use the second revolution of the quasi-periodic orbit to be analyzed. This revolution is divided into the number of points we want (typical is 250) and the program calculates for each one of them the normalized halo orbit position and velocity as well as its stable directions.

The final step is the globalization of the stable manifold from the results of the program `VECSWS`. The program `ESTWS1` does this job and gives as outputs the initial position and velocities of the manifold to be used in the backwards integration just in the way it was done previously for other models.

Thus, the standard output of the program `ESTWS1` are a number of initial conditions to be used, each one related to an specific date in Ephemeris Julian Date. This is another consequence of the model being non-autonomous, the concept of “phase” of the halo orbit does not exists anymore. Nevertheless, the quasi-periodic orbit is close enough to the original halo so we can make a parallel between both definitions and substitute the parameter phase used previously for the index of the initial condition used. The relation between both will be better discussed

later in this section.

6.2.3 The JPL vectorfield

The vectorfield of the new model was developed with a main C function responsible for summing up all the contributions calculated with other specialized subroutines.

The solar system bodies positions from the JPL model are read with the use of two subroutines previously developed and available by Masdemont. With them, we can know the position and velocity of each body at an desired epoch.

The gravitation acceleration due to each of the solar system bodies is computed considering them point masses by a subroutine coded in FORTRAN based a previously available subroutine.

Secondly the main subroutine calls a new function that computes the low thrust acceleration. This new subroutine had to be written to work in the sidereal system. Although not exactly exposed in section 3, its computation can be basically summarized as

1. The velocity vector of the spacecraft with respect to the Earth is computed simply with the difference between their velocities with respect to the sidereal system;
2. The velocity vector is then normalized and its product with the low thrust acceleration magnitude is the desired acceleration vector.

Finally the near earth perturbing accelerations are added calling the functions previously developed. This time the integration of both acceleration in different reference systems is simplier since the geocentric quasi-inertial system does not rotate with respect to the sidereal one. Basically we only rotate the vectors due to the difference of the ecliptic and equatorial planes and uses a scale factor to set up the units. Following the standard of the ephemerides, the integrations are done with the kilometer and day as length and time units respectively.

6.2.4 Parameters Defining the Model

The JPL ephemerides model used was the DE403 that was previously available and that covers the time interval from JED 2433264.5 (December 14th, 1949) to JED 2469808.5 (January 2nd,

2050).

The programs used to determine the manifolds, discussed above, only allow the choice of the time of the transfer indirectly, since we choose a time for the beginning of the simulation of the quasi-periodic halo, and later we use another revolution to derive the manifolds. Nevertheless, intervals between two dates used for a same halo orbit are approximately constant, i.e., we we delay the reference date for 14 days all the transfer dates will be approximately delayed by the same time.

For all the discussion presented in this report, we choose the month of July 2006 as the basic input from the routines. Actually four dates were most tested as the inputs of the program `GQPTPS` explained below: 1st, 8th, 15th and 22nd of July 2006. The number of divisions made in each halo orbit to determine initial states of the manifolds was set to 500.

Finally, the spacecraft parameters were not varied in this part of the project since their basic influence were discussed with the CRTBP model. Their values were set to: $A/m = 100.0[m^2/kg]$, $C_D = 2.3$ and $C_R = 1.0$ accordign with the discussion presented in the last section.

6.3 Halo Orbits and the Behavior of their Manifolds

As discussed above, the periodic halo orbit observed in the CRTBP problem is replaced by and quasi-periodic one when the JPL ephemerides model is used. Figure 6.1 presents both of them in order to allow a comparison between them. As we can see, one resemble the other, as discussed previously.

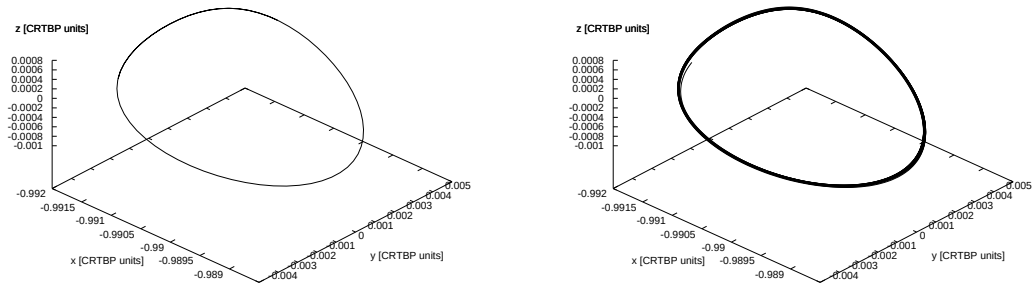

Figure 6.1: Comparison between a SEL1 CRTBP periodic halo orbit (left) and theSEL1 JPL Ephemerides quasi-periodic halo orbit (right) when a CRTBP like system of conditions is used for the plot.

Our first idea was using the previous results obtained with simpler models as starting transfers

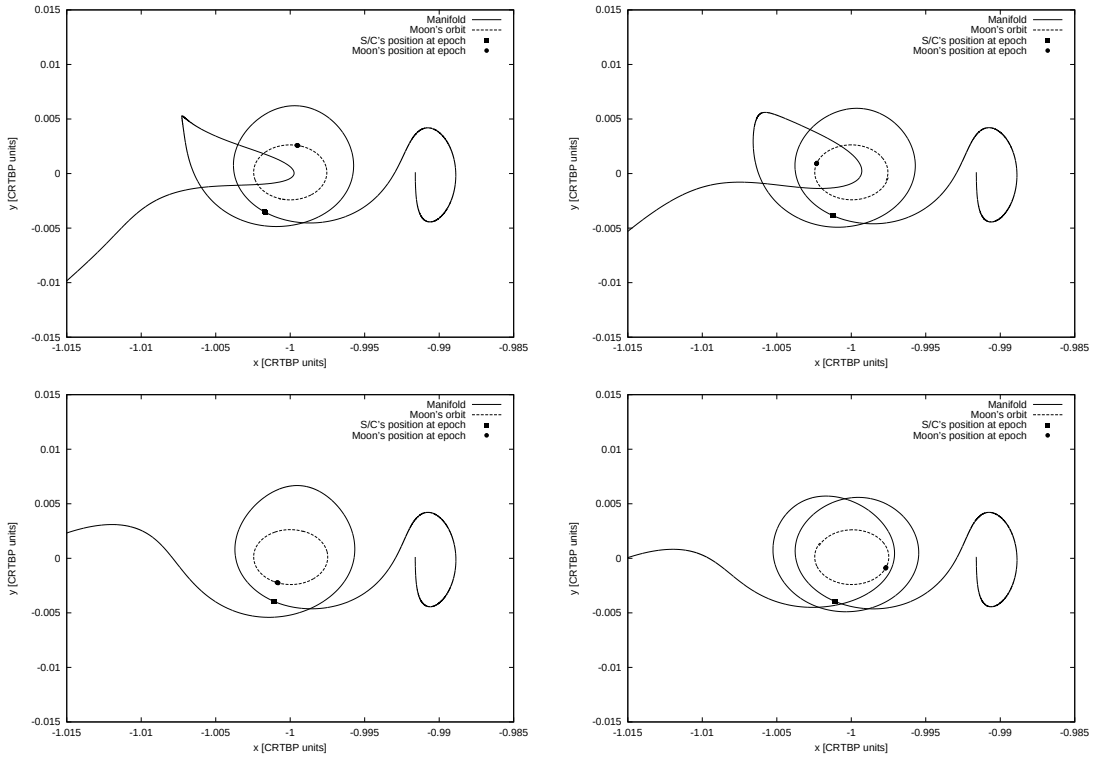

Figure 6.2: Comparison of the manifolds for different times throughout a month. All of them are with respect to a halo orbit of amplitude $\alpha_4 = 0.04$ and the same "phase"(index 1 of the 250 divisions). From right to left and top to bottom pairs reference date of the halo and epoch date represented: (JUL 01 06 ; JUN 03 06), (JUL 08 06 ; JUN 10 06), (JUL 15 06 ; JUN 17 06) and (JUL 22 06 ; JUN 24 06).

to be studied with the JPL ephemerides. As discussed previously, we expect to see the Moon's influence on it, that represents a potential difficulty. Moreover, the phase parameter is changed to the index of the result from the [9] routines and the coast time and thrust magnitude are changed to coherent dimensional units.

The scale factors to change the dimensions are easily obtained from the constants adopted throughout the work and presented in appendix D. The coast time, however, is dependent of the initial distance between the manifold and the halo orbit as discussed in section 4. Since not only this distance but also the calculation of the starting condition is different we can expect that the best values for this parameter will need to be determined again.

Considering all these difficulties the first study performed was related to the behavior of the manifolds. As an example we plot in the figure 6.2 the manifolds computed for a halo orbit with amplitude $\alpha_4 = 0.04$, index 1 of 250 divisions and different reference times. The orbit is plotted using the synodic reference system in order to have a better visualization and to help the comparison with previous results.

As we can observe, the difference in the reference time strongly affects the manifold behavior. While the one at the bottom left of the figure seams to closely agrees with the group 4 of the figure 4.2. The others, however, presents different behaviors not observed before.

The reason for this changes is the influence of the Moon. In the figure, we present the positions of both the spacecraft and the Moon in a specific epoch chosen in such a way that the spacecraft is located approximately in the same position. We can clearly observe the difference in relative position for the different dates.

6.4 Study of Low Thrust Transfers

The differences in the geometry of the manifold between the results of the new model and the previous ones increase the difficulties to use previously obtained results. Moreover, the Moon not only imposibilitates some transfers observed with the CRTBP model, but also allows others that were not possible on it.

A complete study of the new possibilities would be time demanding and probably should be started with a model of intermediately complexity between the RTBP and the JPL Ephemerides, such as the bi-circular restricted three body problem. This, however, would be outside the objectives of this work and also impossible to do with the available time. Thus, it is suggested as a continuation step to it as discussed in section 6.4.3.

Therefore, our objective in this part of the project was to look for some low thrust transfers with a low eccentricity parking orbit using the JPL ephemerides model and study its relation with other simulation parameters. In special the position of the Moon expressed by the reference time. In order to do so, we developed a simple method to import results obtained with the CRTBP in order to be used in the JPL Ephemerides. This method should be improved in order to be more automatically and precise, but proved to satisfy our needs in this project.

For simplicity and time requirements we present in this section only results for SEL1 transfers. Nevertheless, results for SEL2 are expected to be very similar as discussed in the previous sections.

6.4.1 Relation Between the CRTBP and the JPL Ephemerides Transfer Parameters

Our main objective here was to find a mathematical relationship relating the phase and coast time values of the CRTBP model with the manifold point index and the coast time in the JPL Ephemeris model. Once this relation is established, we can test the interesting orbits obtained with the simple model in the complex one.

The idea used was based in comparing the values of the position in the x-axis when the manifold crossed the $y = 0$ plane from the positive to the negative. In order to explain it we present figure 6.3. On its left hand side we see the manifolds of a SEL1 halo orbit with only the points with positive y component are plotted (in the synodic reference system). All the manifolds crossed the plane $y = 0$ before arriving at the Earth and its x coordinates exactly when that happens[5] can be plotted with respect to the phase of the halo or the manifold point index in the case of the JPL model, as presented in the right side of the figure.

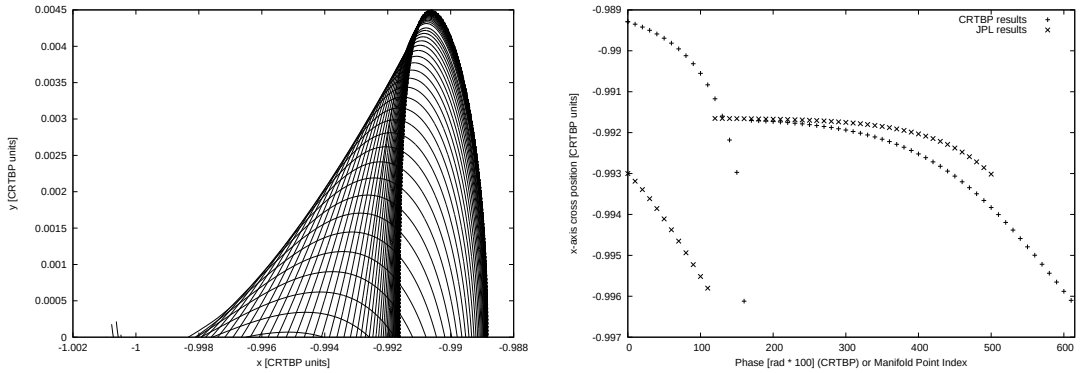

Figure 6.3: Simple method used to establish the relation between the transfer parameters in both models.

With this graphic we can establish a simple linear function that relates the phase with the manifold point index. The scale factor value is set corresponding to the difference in both limits, and the offset is determined comparing points in the graphic. Finally we got the following expression for the 0.08 halo orbit amplitude

$$n_{JPL} = \frac{500}{620}\left(\phi_{CRTBP} - 5.00\right) + 40. \tag{6.1}$$

A second relation must be establish to relate the values of the coast time. In the previous sections, with the CRTBP model, we used the name “coast time” to define all the time interval between the computed first point of the manifold till the link with the thrust arc of the trajectory.

[5] To be exact, it was used the last point of crossing before an arbitrary limit value of x. This must be done since the manifolds can perform several turns near to the halo orbit before departure to the Earth. The arbitrary limit was set to -0.996 to avoid the influence of the Moon on the manifolds

As discussed in section 4 this definition is not accurate since it is dependent from initial distance from the halo orbit and the manifold used.

A more precise parameter should be the time since the end of the thrust vector and the cross of the $y = 0$ plane. Once we are in the same manifold, this time should not vary with different parameters. Thus, the idea was to compute the time from the beginning of the integration until the time of plane cross for all values of halo phase. Then, the result was subtracted from the values tabuled for interesting maneuvers and used in the simulations with the JPL Ephemerides.

Testing with some manifolds, we could determine that the results obtained with this simple method could satisfy our needs of accuracy for this work. Nevertheless, the method still lacks of some accuracy and automatization to be implemented in a wide range of halo orbits and transfers.

A better method could be considered using the intersections of the manifolds with a plane parallel to the y axis and at a defined position with respect to the x one. The result would be a closed curve for the CRTBP manifolds and an open one for the JPL ones, but that closely resembles the first one. Then it would be a question of use the relations between the phase (manifold index) and the points in this plane to establishes a transformation that links both of them. This could be accomplished with a least square method, for example.

The solution for the coast time is more difficult not for technical reasons, but because of its poor definition. The best idea would be to define the coast time from an arbitrary plane intersection or something similar. This would eliminate all problems with respect to it.

6.4.2 Results for the Interesting Transfers

Once the relation between the transfer parameters were done, we use the values of interesting transfers obtained with the CRTBP model to look for the corresponding in the JPL Ephemerides model. The idea was testing several transfers with manifold index and coast time close to the best computed ones from the approximations. Moreover, several reference times were used, in order to study the impact of the influence of the Moon on them.

In order to illustrate the study, the results presented in this and in the next subsection are all for an halo orbit with amplitude $\alpha_4 = 0.04$ and thrust magnitude of $F_T = 2.0 \cdot 10^{-4}[ms^{-2}]$. Our objective was to find the transfer orbits related to zone 1A of the halo phase-coast time surface

(see section 4). These transfers were used since they are the simplest ones. The others, since consists of more time near to the Earth or Earth by-passes, tend to be more influenced by the Moon.

Using the relations presented above and the results presented in appendix F, we obtain that the parameters for the best transfer would be manifold index of 477 and coast time of 203 days, in the JPL ephemeris model. Figure 6.4 presents the results for the eccentricity of the parking orbit for a neighborhood of these parameters and different reference dates.

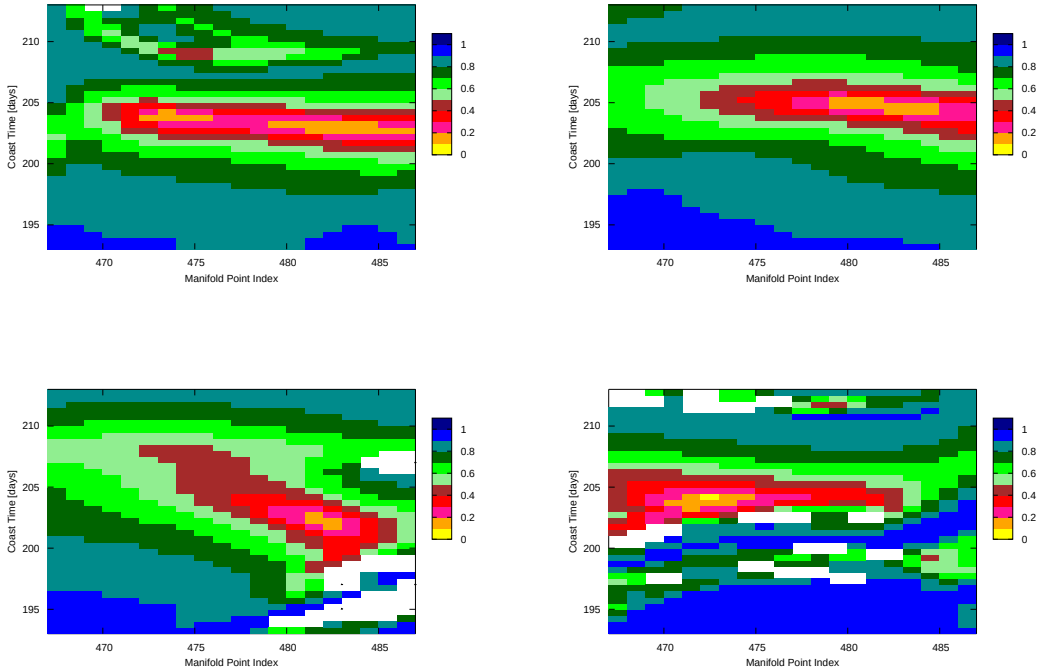

Figure 6.4: Eccentricity of the parking orbit for several transfers near to the predicted best one for halo amplitude $\alpha_4 = 0.04$ and thrust magnitude $F_T = 2.0 \cdot 10^{-4}[ms^{-2}]$. From left to right and from top to bottom, reference dates: JUL 01 06, JUL 08 06, JUL 15 06 and JUL 22 06.

As we can observe the results are strongly influenced by the reference date, i.e., by the relative position of the Moon with respect to the spacecraft during the transfer. The points not colored represent transfer parameters for which some problem happened. Usually a Moon collision or a ejection from the neighborhood of the Earth by a close encounter with the Moon. Nevertheless, it is important to notice that transfers with low eccentricity parking orbits were observed for all the four positions of the Moon, even with a change in the value of the parameters.

In order to better study the influence of the reference date for the best transfer obtained from the scans shown above, we present the transfers computed with the same parameters but different

reference times. They are shown in figure 6.5, where we plot all the transfers and also a zoom in the region when the satellite crosses the orbit of the Moon.

In the right hand side of the figure, the epoch plotted is chosen such as the spacecraft is almost at the same point in space for all the transfers to compare the relative position with respect to the Moon. Table 6.1 presents the eccentricity and inclination[6] of the parking orbits obtained with these same thrusters.

Table 6.1: Eccentricity and inclination of the parking orbits of the transfers presented in figure 6.5

Reference Date	Eccentricity	Inclination [degrees]
JUN 01 06	0.311	40.6
JUN 08 06	0.600	40.7
JUN 15 06	0.014	41.0
JUN 22 06	0.657	44.7

As we can observe from the table, the major influence of the Moon in all the cases was on the eccentricity of the parking orbit. The changes in its inclinations are also present but are not very significant in these particular cases.

The total transfer time and thrust were not compared in table 6.1 because the orbit have very different eccentricities. In order to make a proper comparison two transfers with low eccentricity parking orbits should be compared. This was done for a small number of orbits and nothing significant was observed for them. However, we cannot say anything about this topic due to the transfers that are possible due to the moon (see next section). For the transfers expected the thrust and total transfer time were in accord with the CRTBP results.

6.4.3 Transfers which are Strongly Influenced by the Moon

Results presented in the last section does not show any transfer that was really strongly affected by the Moon. This was not our objective, as discussed previously, but some of them were found during our tests and it is interesting to show two different possible effects. Two examples are presented in figure 6.6.

In the first case we have a good example of the Moon dominating the motion. The transfers passed so closely to the Moon that was attracted to it and stayed in its orbit till collided with its surface. Actually this is an example of a good low thrust transfer from a low Moon orbit to the SEL1 halo orbit.

[6] With respect to the Earth's Equatorial plane

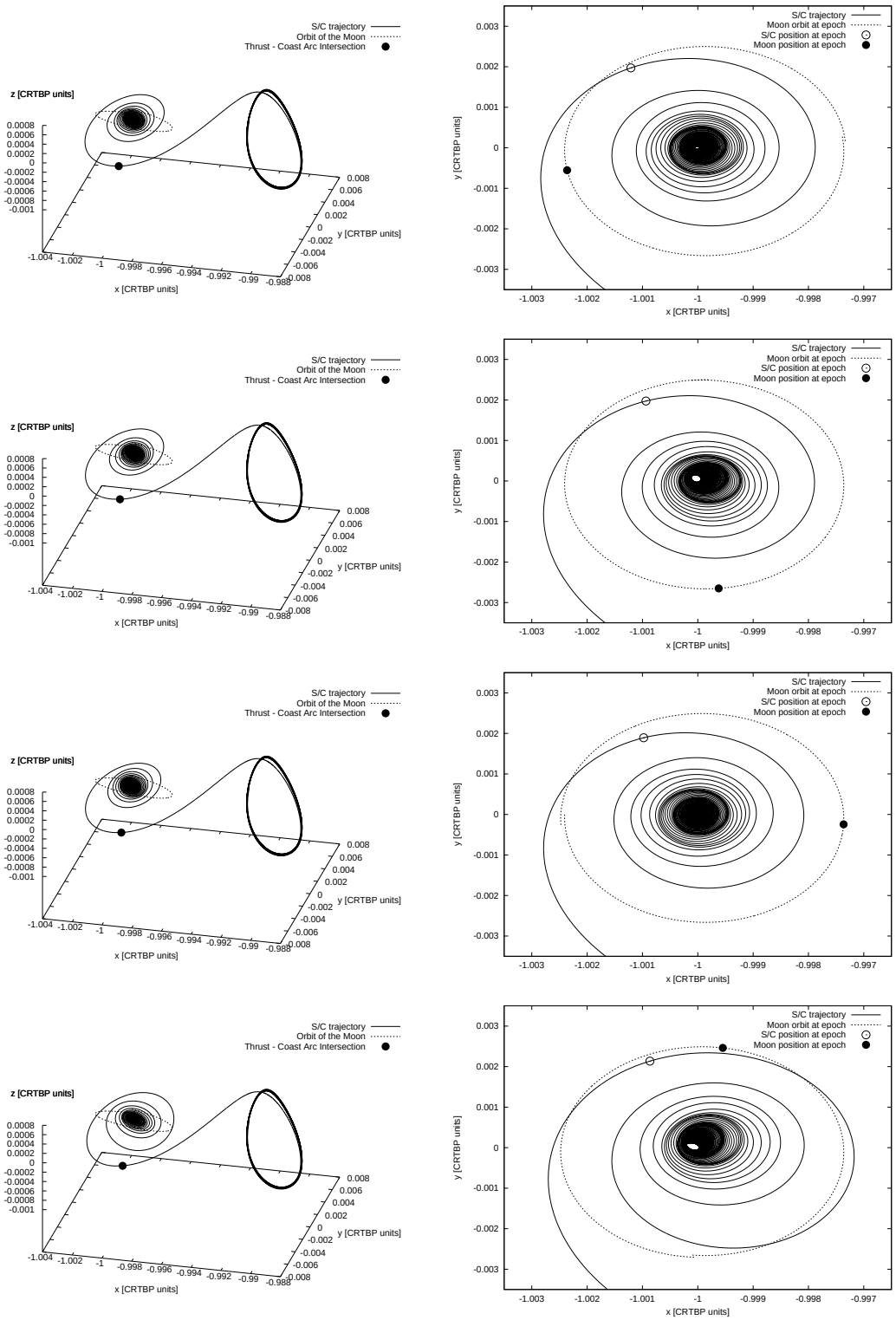

Figure 6.5: Transfer trajectories computed for manifold index equal to 482 and coast time equal to 202.2 days. From top to bottom reference time and epoch time (left side): (JUL 01 06 ; NOV 06 06), (JUL 08 06 ; NOV 13 06), (JUL 15 06 ; NOV 20 06) and (JUL 22 06 ; NOV 29 06) .

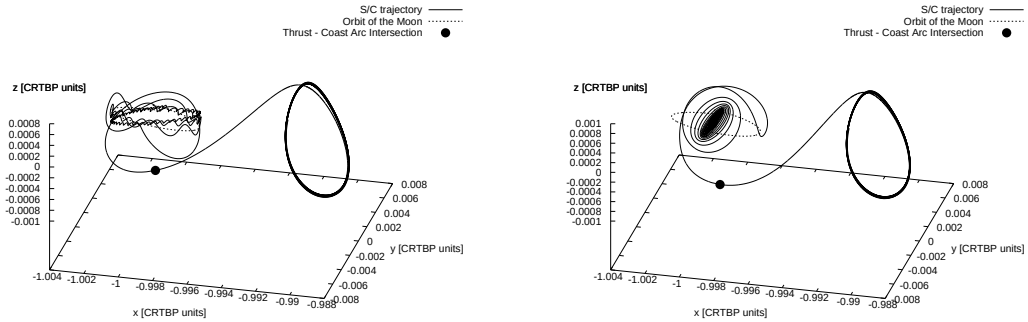

Figure 6.6: Examples of transfers which are strongly affected by the Moon. On the left the reference date 22 Jun 06, manifold index 478 coast time 200.0 days. On right side reference date 08 Jun 06, manifold index 444, coast time 202.0

The Moon's effect can also help on the transfers. The transfer presented in the right hand side of figure 6.6 is a clear example of using the Moon to change the inclination of the parking orbit, what could be necessary, for example in the case of launching with high inclination angles such as in the case of the Soyuz from Baikonour.

Conclusions and Future Work

The use of libration points orbits is already a reality for various mission objectives, and it only tends to increase in the future. Moreover, after the successful flight tests of the NSTAR ionic thruster in Deep Space I, the solar electric low thrust thrusters were qualified as possible propulsion system for future mission, in special those associated with large payload weights.

The studies conducted with the simple CRTBP model proved to be possible simple transfers to SEL1 and SEL2 halo orbits with only one constant magnitude thrust arc followed by a coast one starting in low eccentricity and low inclination LEO. Although these transfers were only possible for restricted sets of halo orbit phase and coast time, these sets does not present considerable changes with variations of the target halo orbit amplitude and thrust magnitude. Thus, with the results of this project, we can guess the probable location of the interesting zones in the halo phase - coast time surface for other values of thrust magnitude and halo orbit amplitude.

From the study of the effects of the near Earth perturbations, we observed that the impact of the gravitational harmonics and atmospheric drag were not significant to the transfers. The first one only affects orbital elements which does not represent losses in he payload such as the right ascension of the ascending node. The atmospheric drag effects should be more carefully analyzed only during a further step of the mission design, when the altitude of the parking orbit is precisely determined. Even in this case, they are only significant if low altitudes (below 500 km) are considered. The greatest effect on the interesting transfers is the produced by the solar radiation pressure. The reason is that its magnitude almost does not vary during all the transfer. Moreover, it affects the eccentricity of the parking orbit, which is a crucial factor for the payload. Fortunately, the low eccentricity zones does not change considerably in size with its action, but only moves slightly its position in the halo phase - coast time surface.

The use of the JPL Ephemerides model, even if limited due to time restrictions, was able to show how the CRTBP can be applied in order to determine accurate transfer parameters and trajectories. The Moon influence was analyzed and it was show that a proper choose of dates can eliminates most of its perturbing effects on the transfer.

As a parallel product of this work, it was developed and validated a precise near earth perturbations model that is able to be integrated with other projects or even changed without great difficulties, according to the desired accuracy.

For further work we must cite the continuation of the study of the transfers with the JPL

Ephemerides model. This should be done applying more precise methods described in this project to develop the relation between the parameters of the transfers computed with the CRTBP model and the JPL ones. Moreover, a precise study about the influence of the Moon could be performed.

Finally, using the results from this project and data from primary estimations of spacecraft parameters, a more precise analyze could be done determining a best parking orbit altitude, launch date and thrust magnitude. Thus, a complete mission could be designed.

Acknowledgements

This project is a result of a bilateral agreement between the Escola Tècnica Superior d'Enginyeria Industrial de Barcelona (ETSEIB) which is part of the Universitat Politècnica de Catalunya (UPC) and the Instituto Tecnológico de Aeronáutica (ITA) of Brazil.

The student, which is actually coursing the fifth year of its bachelor degree in Aeronautic Engineering in ITA, is allowed by his institution to accomplish his obligatory practice time and his final project in foreign universities or research institutions.

The agreement with ETSEIB was possible due to previous contacts between Prof. Dr. Josep Masdemont of ETSEIB and Dr. Antonio Bertachini, a researcher of the Instituto Nacional de Pesquisas Espaciais (INPE), where the student was already developing some projects as a "rookie researcher".

Firstly I thank God for the wonderful experience, for the absence of problems throughout it, and specially for giving me a wonderful family which always gave me all the support I needed, and that even becoming geographically more distance each day due to many reasons, is still as close as always.

I would like to thank Prof. Josep Mademont for accepting me as a guest student, for the dedicated time of tutoring, for all the useful advises and interesting talking.

To the Departament de Matemàtica Aplicada I, I would like to say thanks for accepting and receiving me, providing access to all its facilities and supports needed to the accomplishment of this project.

My thanks to the INPE, in special to the researcher Dr. Antonio Bertachini and Dr. Elbert Macau, for facilitating the contact and being the linkers that were fundamental to this experience. Moreover, I must thank FUNCATE and Dr. Geilson Loureiro for providing the special funding to support my stay in Barcelona.

To the Divisão de Engenharia Aeronáutica do ITA, thanks for making possible these extern projects, specially Prof. Dr. Paulo Rizzi, the responsible for the creation and increasing of the program, and supporter of a wonderful dinner in Barcelona during the Carnaval Holidays for me and the students working in Toulouse. Thanks also to Prof. Dr. Pedro Paglione for accepting me as student and for supporting the last parts of the work that will be done in Brazil.

I would also thanks all the friends of the Associação dos Pesquisadores e Estudantes Brasileiros na Catalunha (APEC), for receiving me so friendly, for helping in the everyday difficulties of living in a foreign country, and for the company in exploring the main sites of Barcelona and Catalunya.

Finally I would like to thank my colleges of AER06 class, specially those who were working in this kind of projects, for sharing the experiences and helping mutually. Moreover, I thanks my roommates of Brazil, specially Estillac, Miguel and Israel for the wonderful friendship and help in everything I needed from them.

I hope that this first experience helps the improvement of the relations between the institutions involved in this project, allowing further exchanges of students, researches and information between them.

References

[1] Arianespace. *Ariane 5, User's Manual, Issue 4, Revision 0*, November 2004. Available electronically at `http://www.arianespace.com/site/documents/Ariane5_users_manual_Issue4.pdf`. Visited on April 3, 2006.

[2] R. R. Bate, D. D. Mueller, and J. E. White. *Fundamentals of Astrodynamics*, chapter 1,2. Dover Publications, Inc., 1971.

[3] J. R. Brophy, R. Y. Kakuda, J. E. Polk, et al. Ion propulsion system (nstar) ds1 technology validation report. Technical report, JPL - NASA, 2000. Available electronically at `http://nmp-techval-reports.jpl.nasa.gov/DS1/IPS_Integrated_Report.pdf`, visited on March 9, 2006.

[4] E. Canalias, G. Gomez, M. Marcote, and J. J. Masdemont. Assessment of mission design including utilization of libration points and weak stability boundaries. Technical Report ESA-ESTEC ARIADNA 03/4103, ESA, 2004.

[5] V. A. Chobotov, editor. *Orbital Mechanics*, chapter 8,9,10, pages 209–274. AIAA Education Series. American Institute of Aeronautics and Astronautics, Inc., 1991. Third Printing.

[6] European Cooperation for Space Stadardization, ECSS. *Space Engineering, Space Environment*, JAN 2000. ECSS-E-10-04A.

[7] J. Gilland, D. Fiehler, and V. J. Lyons. Electric propulsion concepts enabled by high power systems for space exploration. In *2nd International Energy Conversion Engineering Conference, Providence, Rhode Island*, number AIAA-2004-5960 and NASA/TM-2005-213371. AIAA, 2004. Available electronically at `http://ntrs.nasa.gov/index.cgi?method=display&redirect=http://hdl.handle.net/2060/20050161946&oaiID=oai:casi.ntrs.nasa.gov:20050161946`. Visited on March 9, 2006.

[8] G. Gómez, A. Jorba, J. Masdemont, and C. Simó. Study of the transfer from the earth to a halo orbit around the equilibrium point l1. *Celestial Mechanics and Dynamical Astronomy*, 56:239–259, 1993.

[9] G. Gómez, A. Jorba, J. Masdemont, and C. Simó. *Dynamics and Mission Design Near Libration Points - Vol. III - Advanced Methods for Collinear Points*, pages v–x, 69–78, 93–101. World Scientific Monograph Series in Mathematics - Vol. 4. World Scientific, 2001.

[10] R. W. Humble, G. N. Henry, and W. J. Larson, editors. *Space Propulsion Analysis and Design, revised*, chapter 9. The McGraw-Hill Companies, Inc, 1995.

[11] T. S. Kelso. Frequently asked questions: Two line element set format. URL: `http://celestrak.com/columns/v04n03/`. Visited in April 3, 2006.

[12] C. A. Kluever. Simple control laws for low-thrust orbit transfers. In *Spaceflight Mechanics*, volume Second, pages 1455–1468, 1998.

[13] J. J. Masdemont. High order expansions of invariant manifolds of libration point orbits with applications to mission designs. *Dynamical Systems, an International Journal*, 20:59–113, 2005.

[14] J. Meeus. *Astronomical Algorithms*, chapter 7,9 and 24. Willman-Bell, Inc., 1991.

[15] O. Montenbruck and E. Gill. *Satellite Orbits - Models, Methods, and Applications*, chapter 2,3,5, pages 15–116,157–190. Springer, first edition, 2000. Corrected 2nd Printing 2001.

[16] S. Oleson, L. Gefert, S. Benson, et al. Mission advantages of next: Nasa's evolutionary xenon thruster. In *38th Joint Propulsion Conference and Exhibit cosponsored by the AIAA, ASME, SAE, and ASEE*, number AIAA-2002-3969 and NASA/TM-2002-211892. AIAA, July 2002. Available electronically at `http://scholar.google.es/url?sa=U&q=http://gltrs.grc.nasa.gov/reports/2002/TM-2002-211892.pdf`. Visited on March 9, 2005.

[17] Starsem, The Soyuz Company. *Soyuz User's Manual, Baikonur Cosmodrome, ST-GTD-SUM-01 - Issue 3 - Revision 0*, April 2001. Available electronically at `http://www.arianespace.com/site/images/soyuz_man_baikonur_tit.jpg`. Visited on April 3, 2006.

[18] G. P. Sutton. *Rocket Propulsion Elements, An Introduction to the Engineering of Rockets*, chapter 1,2,16. John Wiley & Sons, Inc., sixth edition, 1992.

[19] V. Szebehely. *Theory of Orbits, The Restricted Problem of Three Bodies*, chapter 1,10.2, pages 7–41,131–138,557–561. Academic Press, 1967.

[20] Spdf modelweb: Geophysical models. URL: `http://modelweb.gfsc.nasa.gov/models_home.html`. Visited in May 14, 2006.

[21] Introduction to soyuz. Available electronically at `http://www.starsem.com/soyuz/introduction.htm`. Visited on April 5, 2006.

[22] The james webb space telescope. URL: `http://www.jwst.nasa.gov/about.html`. Visited in May 30, 2006.

[23] The solar and heliospheric observatory. URL: http://soho.esac.esa.int/. Visited in May 30, 2006.

[24] Icgem - table of models. URL: http://icgem.gfz-postdam.de/ICGEM/modelstab.htm. Visited in May 14, 2006.

[25] Current local time in barcelona - spain. URL: http://www.timeanddate.com/worldclock/city.html?n=31. Visited in May 18, 2006.

[26] Astronomical almanac online. URL: http://asa.usno.navy.mil/contents.html, 2007. Pages K6 and K7, Visited in June 28, 2006.

A Classical Orbital Elements

The size, shape and orientation of any conic orbit can be defined by five independent quantities. Another sixth parameter is needed to define the position of the satellite in an specific instant of time.

This set of six parameters is defined in relation to a inertial coordinate system. When working with the sun-earth system, this coordinate system will be the heliocentric-ecliptic, which center is located at the center of the earth and the fundamental plane (X-Y plane) is the plane of the earth orbit.

The classical orbit parameters are described below. They can be better understood by looking at figure A.1.

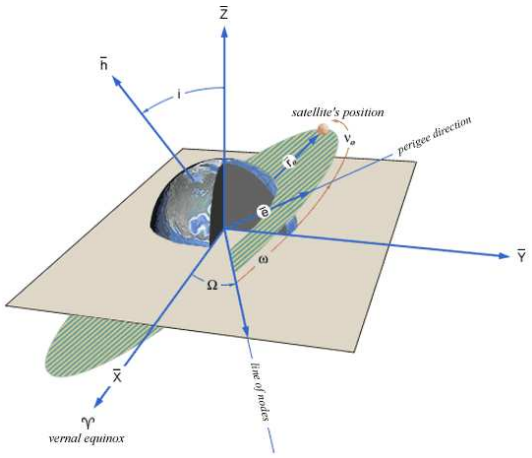

Figure A.1: Orbital Elements

a **- Semi-major axis** a constant defining the size of the orbit;

e **- Eccentricity** a constant defining the shape of the conic orbit;

$$\begin{array}{cc} e = 0 & \text{Circle} \\ 0 < e < 1 & \text{Ellipse} \\ e = 1 & \text{Parabola} \\ e > 1 & \text{Hiperbola} \end{array} \tag{A.1}$$

i **- Inclination** the angle between $\vec{K}$, which is perpendicular to the fundamental plane, and the angular momentum vector $\vec{h}$;

Ω **- Longitude of the accending node** the angle, in the fundamental plane, between $\vec{I}$ and the point where the satellite crosses through the fundamental plane in a northly direction measured counterclockwise when viewed from the north side of the fundamental plane;

ω **- Argument of periapsis** the angle, in the plane of the satellite's orbit between the ascending node and the periapsis point;

T **- Time of periapsis passage** an epoch when the satellite is at the periapsis.

Although these are "the classical orbit elemens", some of the parameters are usually changed for other ones that are more adjusted to the specific problem. In this work the " time of periapsis passage" is substituted by the "true anomaly at epoch" define by:

ν **True anomaly at epoch** the angle between periapsis and the position of the the satellite at a particular time t.

B Restricted Three-Body Problem - Mathematical Development

The main objective of this section is to present the mathematical developments of the equations of the motion of the CRTBP used in this work. Moreover, a small historical background is presented in order to name the major contributors to the theory and the need of their development. A short introduction about the Jacobi constant is also available due to its large use in the CRTBP theory.

The deductions presented here are completely based in reference [19], in which a detailed deduction of the two-dimensional problem is presented in chapter 1 and the modification to a three-dimensional space is available in section 10.2.1. The historical background is based in the sections of same name of first two chapters of reference [2] and in the introduction section of reference [19].

B.1 Historical Background

Sir Isaac Newton presented to the world his law of universal gravitation in 1687, more then twenty years after discovering it [2]. Applying this law, toghether with his second law of the motion, he was able two solve the *two-body problem*. It basically consists in describing the motion of 2 bodies in space interacting between themselves by the gravitational force with two simplyfing assumptions: the masses are homogeneous and spherically symmetric and there are no other external forces acting in the system.

This solution proved the famous Kepler's three laws of planetary motion published in 1609 and 1619 [2]. The orbital elements used in this work and presented in Appendix A are based entirely in this theory.

The application of this model is based in the low influence of distant bodies is the motion of two near bodies. The next problem to be solved in complexity order is the three-body problem. This problem, however, is much more complex and can not be solved analitically. Therefore, simplifications are applied aiming at a solution which can be achieved and applied in practical problems. From this arises the restricted three-body problem.

The first contributions to it were made by Euler in 1772 in his second lunar theory, although some authors give credit to Jacobi in 1836 [19]. His major contribution was the introduction of the synodic coordinate system. Lagrange, in the same year, made his collaboration, particularly

with the discovery of the Lagrangian (libration) points that are one of the bases of this work.

In 1836, Jacobi, who rediscovered the synodic system, made another great contribution with the integral of the equations of motion, today known as the Jacobian integral. Hill in 1878 made use of this integral establishing the *forbidden region* where the third body can never be.

Poincare in 1899 published his work which is known for have a great emphasis in the qualitative aspects of celestial mechanics as opposed to the quantitative approach. Numerous other scientist continued the work that had another great advance with Kolmogorov in the 1950s.

B.2 Statement of the Problem and Equations of Motion in the Sidereal System

The three dimensional restricted three body problem is defined as: *to describe the motion of a third body which is attracted by other two but that does not influence their motion. These two other bodies, called primaries, revolve their center of mass in circular orbits under the influence of their mutual gravitational attraction.*

Analyzing first the motion of the two primaries. Their masses m_1 and m_2 are arbitrary but their distribution inside the body is assumed to be such that they may be considered point masses. The balance between the gravitational and centrifugal forces requires that

$$G\frac{m_1 m_2}{l^2} = m_2 a n^2 = m_1 b n^2, \tag{B.1}$$

where G is the Gaussian constant of gravitation, n is the (common) angular velocity of the two masses, which is called *mean motion* in celestial mechanics, l is their mutual distance and a and b are the distances their center of mass and body 2 and 1 respectively. Figure B.1 present an scheme of this configuration.

Rearranging this equation

$$a = \frac{m_1 l}{M} \qquad \text{and} \qquad b = \frac{m_2 l}{M} \tag{B.2}$$

where $M = m_1 + m_2$.

Now analyzing the third body motion. The time is represented by the symbol t^* to preserve t to the dimensionless time. The reference system that we will use to describe its motion is called *sidereal coordinate system*. Its origin is in the center of mass of the primaries and it is fixed (inertial). The reference frame associated with it is formed by the axes X, Y, Z shown in figure B.1. The axes X and Y form the *fundamental plane* which coincides with the primaries plane of motion.

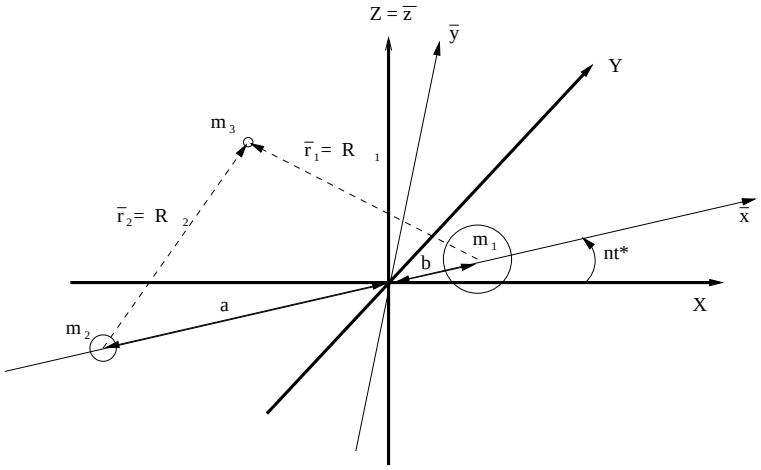

Figure B.1: CRTBP and the sidereal and the synodic coordinate systems

Applying the Newton's second law of the motion follows that

$$\frac{d^2X}{dt^{*2}} = \frac{\partial F}{\partial X} \quad , \quad \frac{d^2Y}{dt^{*2}} = \frac{\partial F}{\partial Y} \quad \text{and} \quad \frac{d^2Z}{dt^{*2}} = \frac{\partial F}{\partial Z} \tag{B.3}$$

where X, Y and Z are the coordinates of m_3 in the sidereal coordinate system, and F is the negative gravitational potential which can be expressed by

$$F = G\left(\frac{m_1}{R_1} + \frac{m_2}{R_2}\right). \tag{B.4}$$

The distances R_1 and R_2 can be easily deducted by looking at figure B.1 and are expressed by

$$\begin{aligned} R_1 &= [(X - b\cos nt^*)^2 + (Y - b\sin nt^*)^2 + Z^2]^{\frac{1}{2}}, \\ R_2 &= [(X + a\cos nt^*)^2 + (Y + a\sin nt^*)^2 + Z^2]^{\frac{1}{2}}. \end{aligned} \tag{B.5}$$

Substituting the equation B.5 into B.4 and B.4 into B.3, the set of differential equations describing the motion of the third body is achieved

$$\begin{aligned} \frac{d^2X}{dt^{*2}} &= -G\left(\frac{m_1(X - b\cos nt^*)}{R_1^3} + \frac{m_2(X + a\cos nt^*)}{R_2^3}\right) \\ \frac{d^2Y}{dt^{*2}} &= -G\left(\frac{m_1(Y - b\sin nt^*)}{R_1^3} + \frac{m_2(X + a\sin nt^*)}{R_2^3}\right) \\ \frac{d^2Z}{dt^{*2}} &= -G\left(\frac{m_1 Z}{R_1^3} + \frac{m_2 Z}{R_2^3}\right) \end{aligned} \tag{B.6}$$

B.3 Equations of the motion in a synodic coordinate system

The time dependence of the equations B.6 is not desired because the system's integral is also time dependent, as it will be explained below. Since this time dependence is due to the motion

of the primaries in relation to this system, it is not difficult to imagine that, in a system in which the primaries are fixed, there will not be this time dependence.

Such system, called *synodic coordinate system*, rotates with the primaries. The coordinate transformation from it to the sidereal system is easily deduced from figure B.1 and in matrix notation becomes

$$\mathbf{R} = \mathbf{A}\bar{\mathbf{r}} \quad , \quad \mathbf{A} = \begin{pmatrix} \cos nt^* & -\sin nt^* & 0, \\ \sin nt^* & \cos nt^* & 0, \\ 0 & 0 & 1 \end{pmatrix} \tag{B.7}$$

where the vector $\mathbf{R}$ has the components X, Y and Z, while $\bar{x}$, $\bar{y}$ and $\bar{z}$ are the components of $\bar{\mathbf{r}}$, the position vector in the synodic system.

The transformation of equation B.6 to the synodic frame is easier if complex variables are used. The reference [19] presents this transformation step by step which results in

$$\begin{aligned} \frac{d^2\bar{x}}{dt^{*2}} - 2n\frac{d\bar{y}}{dt^*} - n^2\bar{x} &= -G\left(\frac{m_1(\bar{x}-b)}{\bar{r}_1^3} + \frac{m_2(\bar{x}+a)}{\bar{r}_2^3}\right) \\ \frac{d^2\bar{y}}{dt^{*2}} - 2n\frac{d\bar{x}}{dt^*} - n^2\bar{y} &= -G\left(\frac{m_1\bar{y}}{\bar{r}_1^3} + \frac{m_2\bar{x}}{\bar{r}_2^3}\right) \\ \frac{d^2\bar{z}}{dt^{*2}} &= -G\left(\frac{m_1\bar{z}}{\bar{r}_1^3} + \frac{m_2\bar{z}}{\bar{r}_2^3}\right) \end{aligned} \tag{B.8}$$

where $\bar{r}_1$ and $\bar{r}_2$ are not time dependent.

This set of differential equations seems to be as complex as the B.6 since it does not has time dependent terms, but it has first order derivatives. However, this set can be simplified. The first step is to rewrite B.8 as

$$\begin{aligned} \frac{d^2\bar{x}}{dt^{*2}} - 2n\frac{d\bar{y}}{dt^*} &= \frac{\partial F^*}{\partial \bar{x}} \\ \frac{d^2\bar{y}}{dt^{*2}} - 2n\frac{d\bar{x}}{dt^*} &= \frac{\partial F^*}{\partial \bar{y}} \\ \frac{d^2\bar{z}}{dt^{*2}} &= \frac{\partial F^*}{\partial \bar{z}} \end{aligned} \tag{B.9}$$

The problem of finding a function F^* which makes equation B.9 equal to B.8 is well known in potential theory and its answer is

$$F^* = \frac{n^2}{2}(\bar{x}^2 + \bar{y}^2) + G\left(\frac{m_1}{\bar{r}_1} + \frac{m_2}{\bar{r}_2}\right). \tag{B.10}$$

B.4 Equations of Motion in Dimensionless Coordinates and the Jacobi Constant

Once a simply form for the set of differential equations was achieved and presented in equations B.8 and B.10, the next to step is to rewrite them in dimensionless coordinates. As the work is developed in the synodic reference system, only its adimensionalization will be presented here. For the sidereal system the steps are similar and can be found at reference [19].

Introducing the new dimensionless variables

$$\begin{array}{lll} x = \bar{x}/l & y = \bar{y}/l & z = \bar{z}/l \\ t = nt^* & r_1 = \bar{r}_1/l & r_2 = \bar{r}_2/l \\ & \mu_{1,2} = m_{1,2}/M & \end{array} \tag{B.11}$$

The law of the motion is then reduced to

$$\begin{aligned} \ddot{x} - 2\dot{y} &= \frac{\partial \bar{\Omega}}{\partial x} \\ \ddot{y} + 2\dot{x} &= \frac{\partial \bar{\Omega}}{\partial y} \\ \ddot{z} &= \frac{\partial \bar{\Omega}}{\partial z} \end{aligned} \tag{B.12}$$

where the function $\bar{\Omega}$ is given by

$$\bar{\Omega}(x, y, z) = \frac{F^*}{l^2 n^2} + \frac{\mu_1}{r_1} + \frac{\mu_2}{r_2} \tag{B.13}$$

However, the parameters μ_1 and μ_2 are not independent, since $\mu_1 + \mu_2 = 1$. The choose of which parameter will be eliminated varies in the literature [19]. In this work we will use the same notation as reference [19]: $\mu_2 = \mu$ and $\mu < 0.5$, therefore the bigger mass is located at the right hand side of the x axis.

Moreover, the addition of a constant in $\bar{\Omega}$ will not affect the equations, therefore we use $\Omega = \bar{\Omega} + 0.5\mu(1-\mu)$ in equations B.12. Ω is expressed by

$$\Omega(x, y, z) = \frac{1}{2}\left(x^2 + y^2\right) + \frac{1-\mu}{r_1} + \frac{\mu}{r_2} + \frac{1}{2}\mu(1-\mu) \tag{B.14}$$

which

$$\begin{aligned} r_1^2 &= (x-\mu)^2 + y^2 + z^2 \\ r_2^2 &= (x-\mu+1)^2 + y^2 + z^2 \end{aligned} \tag{B.15}$$

Therefore, the equations B.12 and B.14 completely describe the motion of the third body in dimensionless coordinates. They will form the vectorfield that will be used in this work.

A last, but not least important, mathematical deduction must be presented to introduce the concept of the Jacobi integral. multiplying equations B.12 by $\frac{dx}{dt}$, $\frac{dy}{dt}$ and $\frac{dz}{dt}$ respectively, and integrating with respect to time t:

$$\frac{1}{2}\left[\left(\frac{dx}{dt}\right)^2+\left(\frac{dx}{dt}\right)^2+\left(\frac{dx}{dt}\right)^2\right]=\int_{t_0}^{t}\left(\frac{\partial\Omega}{\partial x}dx+\frac{\partial\Omega}{\partial y}dy+\frac{\partial\Omega}{\partial z}dz\right) \tag{B.16}$$

Using v to represent the dimensionless velocity of the third body, the equation B.16simplifies to

$$\frac{1}{2}v^2=\Omega-\frac{C}{2}\Rightarrow v^2=2\Omega+C \tag{B.17}$$

where C is a constant of integration.

The equations B.16 and B.17 are called *Jacobi integral*, while C is the *Jacobi constant*. The value of C depends only on the initial conditions of the third body.

The Jacobi integral has several applications. One of the most important ones and that will be used in this work is in numerical integrations. It can be used as a measure of the error in the integrations since the Jacobi constant should not change if we are integrating just the CRTBP equations.

C Results from the CRTBP Modeling with Low Thrust for Halo Orbits around SEL2

As explained in section 4 the low thrust transfers for halo orbits around SEL2 is very similar to the ones for SEL1 transfers. This symmetric behavior is observed when $\mu \to 0$, and the study of the orbits in this limit is known as Hill's case.

Basically the same studies made with the transfers to SEL1 orbits were redone to the ones around SEL2. In this appendix we present a summary of this results, with a less deeper discussion of them.

The main difference between the parameters used in the case of the SEL2 to those of the SEL1 has been the sign of the α_2 amplitude. Whenever otherwise specified, all results presented in this section are obtained taking $\alpha_2 = -10^{-3}$. This change is needed in order to consider manifolds that approach to the Earth.

The remaining parameters have the same values as used in the SEL1 case, and the influence in the results is very similar to the ones discussed to the previous case.

C.1 Behavior of the Manifolds

Figure C.1 displays the corresponding results of 4.1 for the manifolds of the orbits around SEL2. Comparing both of them it is evident their high similarity. The main difference noted is a change in the values of the phases associated with each group of manifolds.

Continuing the same studies made for SEL1, figure C.2 presents the projection of one example of manifold of each group in the fundamental plane, as done previously with the figure 4.2.

It is clear from that when compared to figure C.2, the manifolds for SEL1 and SEL2 are strongly related. Actually we can say that the SEL2 manifolds are mirror images of the ones of the SEL1, considering the mirror placed perpendicular to the synodic x axes passing through the Earth.

Tests with different values of the α_2 parameters are also performed with results very similar to the ones of SEL1, i.e, only changes in the phase and coast time are observed, that does not affect the main results of the study.

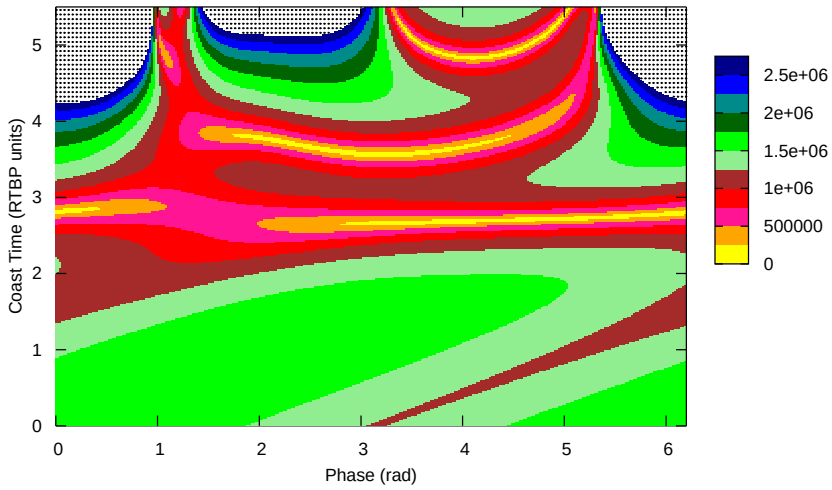

Figure C.1: Altitudes [km] of stable manifolds of SEL2 halo orbit with amplitude 0.08.

C.2 Zones of Low-eccentricity Parking Orbit

An example of a full search around the phase-coast time surface looking for low eccentricity parking orbits is presented in figure C.3. In order to make a comparison, the amplitude of the target halo orbit and the thrust magnitude are the same one of figure 4.4. Again, it is clear the huge similarity between both results.

In order to illustrate a different thing from SEL1 anallyzis, figure C.4 presents the scan results for two different target halo orbit amplitudes.

As it can be observed the target halo orbit amplitude plays a minor role in the location and form of the low eccentricity parking orbit zones in the phase-coast time surface if compared with the influence of thrust seen in figures 4.5. This was also observed in the case of the SEL1 transfers.

Following the procedure done in the case of the SEL1, we can identify and number four interesting zones in the plot. Figure C.5 contains the transfer trajectories for each of this zones, for the same value of halo amplitude and thrust magnitude as figure 4.6.

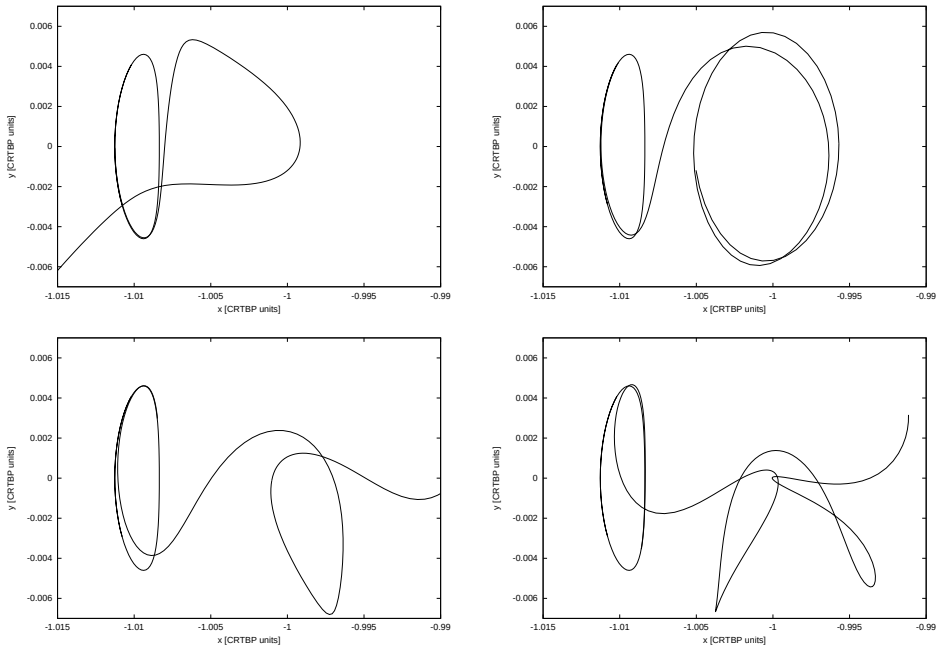

Figure C.2: Behaviors of the manifolds. From left to right and from top to down: $\phi = 0.00$ rad, $\phi = 1.20$ rad, $\phi = 2.50$ rad, $\phi = 4.00$ rad. All relative to an halo orbit with $\alpha_4 = 0.08$.

C.3 Evolution and Size of the Low Eccentricity Zones

In the case of the "size" of the interesting zones, observing the appendix F the value of 33 transfers with parking orbit eccentricity below 0.05 found for a specific set of parameters ($\alpha_4 = 0.16$, $F_T = 1.0 \cdot 10^{-4} [ms^{-2}]$, zone 1) is very surprising. No specific reason for this was found, but it was interesting to prove that the interesting zones can be quite large in the halo phase - coast time surface. Figure C.6 presents two results of this zone with increasing number analyzed transfers and magnifications in the region wanted.

C.4 Influence of the Parameters

In order to save space, the graphics for the SEL2 related to figures 4.9, 4.10, 4.11 and 4.12 for SEL1 have been condensed in only one figure C.7.

As can be seen, the same observations made for SEL1 transfers applies to SEL2. In the case of the eccentricity few can be concluded due to the scattered distribution of the points. The inclination is highly dependent of the target halo orbit amplitude. An increase in the thrust magnitude just causes a small increase in the inclination of the parking orbit and its is bigger

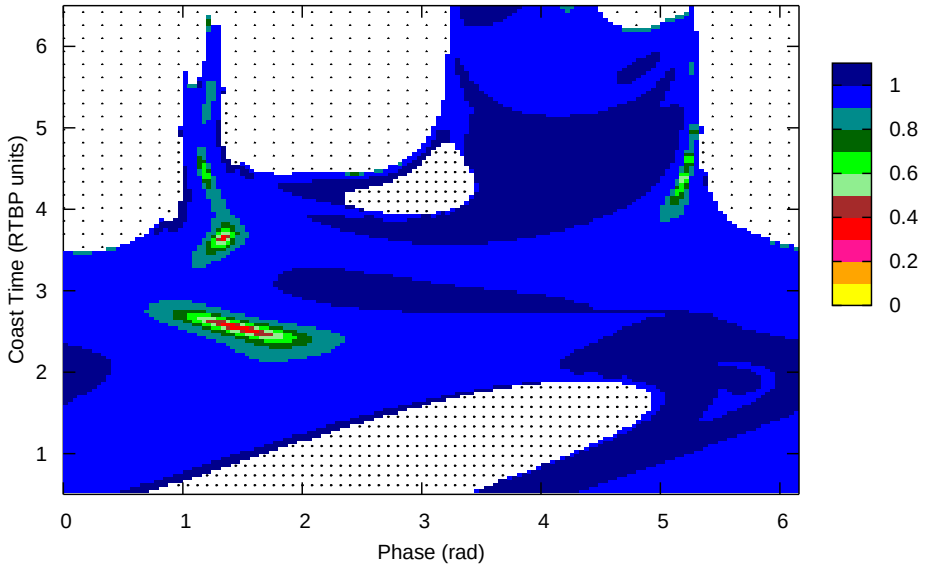

Figure C.3: Eccentricities of the departure orbit for $F_T = 1.00 \cdot 10^{-4}[ms^{-2}]$ and $\alpha_4 = 0.08$.

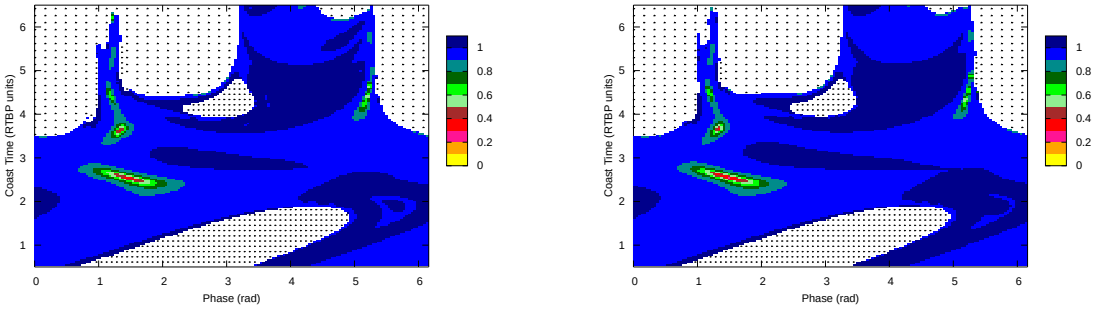

Figure C.4: Same study presented in figure C.3, but with $\alpha_4 = 0.04$ (left) and $\alpha_4 = 0.12$ (right).

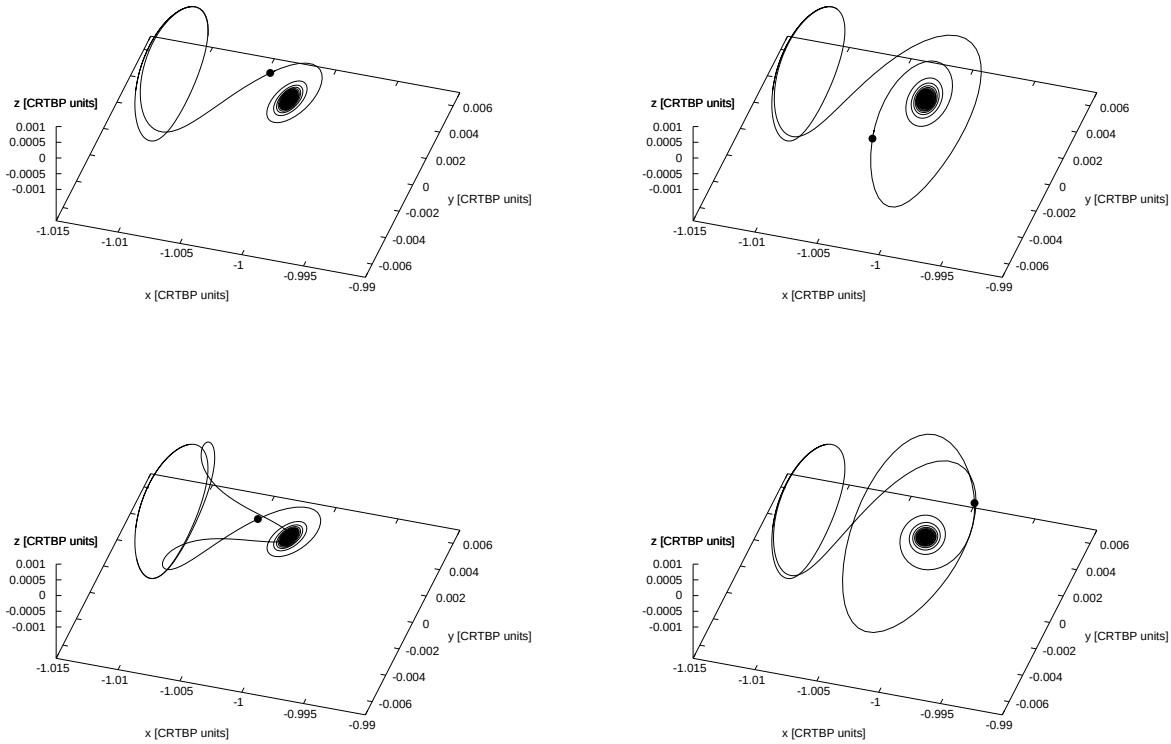

Figure C.5: Examples of trajectories with low-eccentricity parking orbits. All of them calculated with $F_T = 3.00 \cdot 10^{-4}[ms^{-2}]$ and $\alpha_4 = 0.08$. From left to right and from top to bottom: Z1 $\phi = 2.150$ [rad] $t_{coast} = 2.515$ [CRTBP units], Z2 $\phi = 1.475$ [rad] $t_{coast} = 3.715$ [CRTBP units], Z3 $\phi = 5.045$ [rad] $t_{coast} = 4.115$ [CRTBP units], Z4 $\phi = 1.135$ [rad] $t_{coast} = 4.640$ [CRTBP units].

for high values of inclination.

About the total transfer time and thrust time we also observe its exponential behavior with respect to the thrust magnitude and the small changes related with different halo orbit amplitudes. Again, exceptions for this observations can be seen for low thrust magnitudes, usually related with high eccentric parking orbits. Moreover, the thrust time is also similar for the various zones of the halo phase - coast time surface indicating that there is not a better one.

C.5 Evolution of the Orbital Elements During the Transfer

In order to illustrate a different zone of the phase-coast time surface, figure C.8 presents the evolution of the orbital elements for a SEL2 zone 3 transfer.

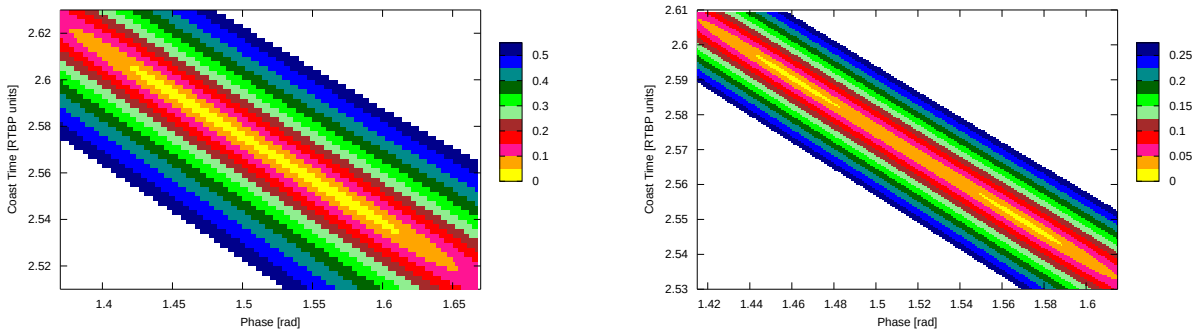

Figure C.6: Magnification of the eccentricities of the parking orbit calculated for $\alpha_2 = 0.16$ and $F_T = 1.0 \cdot^{-4} [ms^{-2}]$.

From this figure we can study better the characteristics of a manifold of the group 1, which approaches and goes away from the Earth several times. The first approach, however, is done in a very eccentric way, which does not allow a low thrust transfer from a low eccentricity parking orbit. The second one, however, is done with less eccentricity and a interesting low thrust transfer can be accomplished.

Due to this first high eccentric approach, the plots of figure C.8 are more difficult to interpret than those of 4.14 since there are some overlaps in some of the magnitudes plotted.

Although with few hope of finding anything in the series of orbital elements with respect o the time that characterizes a good point for a connection with a low thrust arc, as we tried for the SEL1, the same was done for the SEL2 concentrating in the zone with high number of interesting orbits explained above. Figure C.9 is the analogous to the 4.15 but for this transfer to a SEL2 orbit.

Even using the biggest low eccentricity zone found in the scans, the results shown in figure C.9 are very similar to the ones of 4.15. Small changes in both, coast time and halo phase lead to significant changes in the eccentricity profile of the transfer without a clear difference from one to the other.

C.6 Influence of the Check Altitude

Few tests of changing the check altitude value have been done for some of the interesting transfers to the SEL2 that were found. The results, however, are very similar to the ones

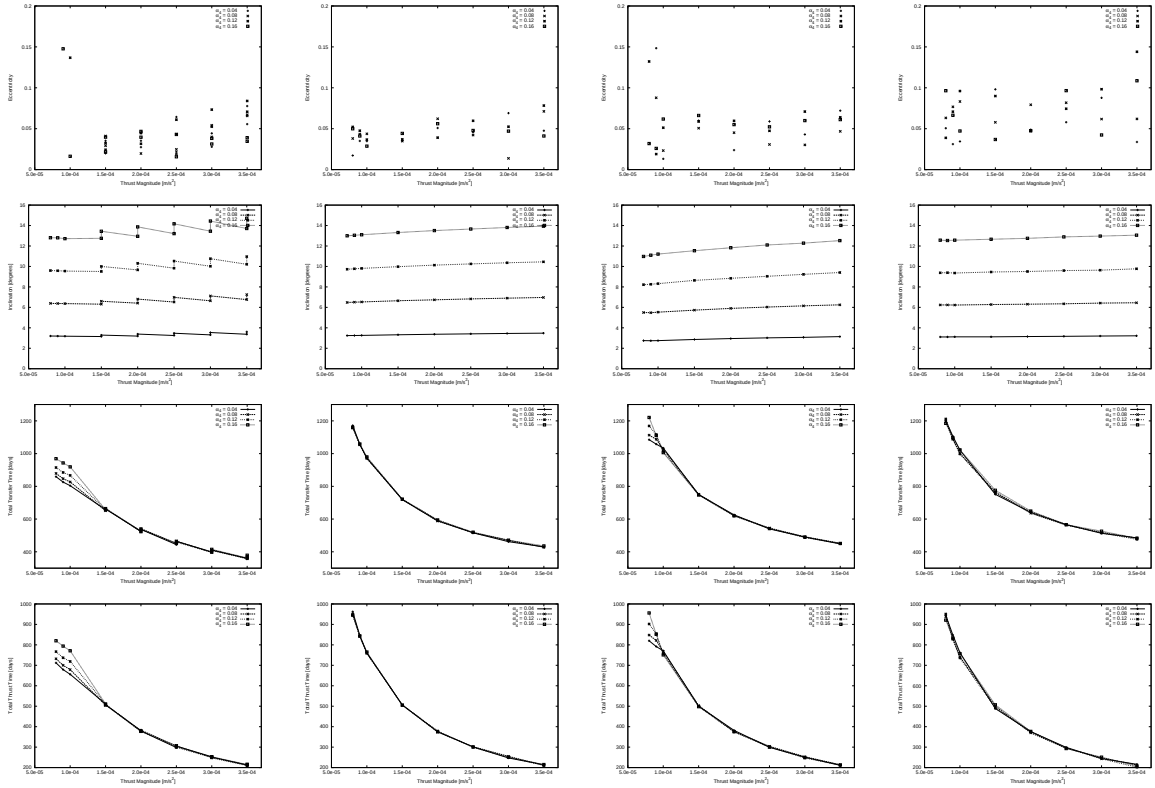

Figure C.7: Influence of the halo amplitude and thrust magnitude on SEL2 transfers. From top to bottom eccentricity and inclination of the parking orbit, total transfer time and thrust time. From left to right: zone 1, zone 2, zone 3 and zone 4.

presented for the SEL1, without any different observation.

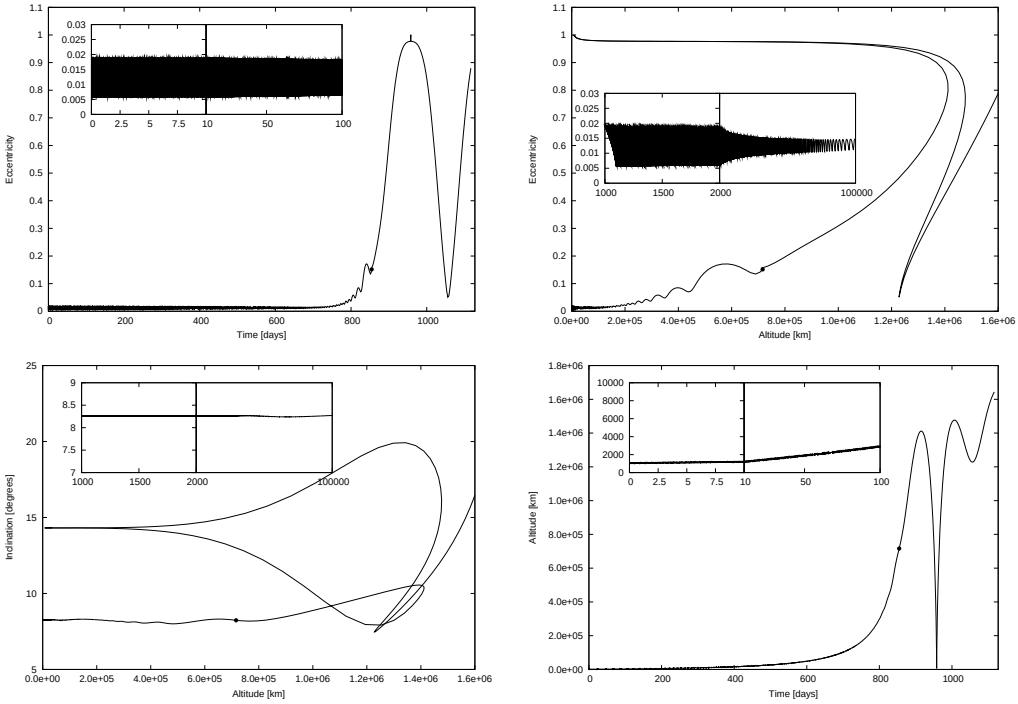

Figure C.8: Orbital elements variations for the SEL2 transfer associated with the lowest eccentric parking orbit for an halo orbit amplitude $\alpha_4 = 0.12$ and a thrust magnitude $F_T = 9.0 \cdot 10^{-5}[ms^{-2}]$.

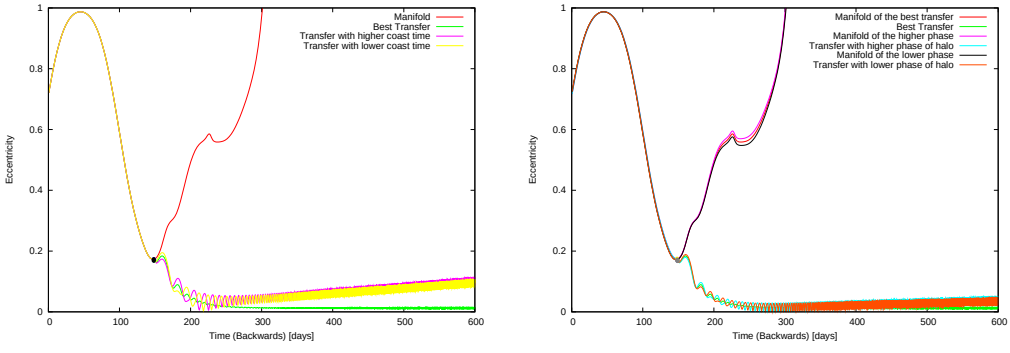

Figure C.9: Comparison between the best transfer with ones with little different parameters for SEL2. On the left the changed parameter was the coast time. On the right it was the halo orbit phase. In order to allow a better comparison, the manifolds are also presented.

D Astronomical Constants

Table D.1: Astronomical constants used in this project

Quantity	Value and Unit	Reference
Sun - Earth/Moon CRTBP mass constant	$3.040423398444176 \cdot 10^{-06}$	JPL Ephem.
Sun - Earth/Moon CRTBP mean distance [7]	$1.49597871464 \cdot 10^{+11}$ [m]	[26]
Sun - Earth/Moon CRTBP mean period	$365.256371[days]$	[19]
Equatorial Radius of the Earth	$6.3781366 \cdot 10^{+06}$ [m]	[26]
Geocentric Gravitational Constant	$3.98600439 \cdot 10^{+14}$ [m^3s^{-2}]	[26]
Solar Radiation Pressure at 1AU	$4.56 \cdot 10^{-6}$ [Nm^{-2}]	[15]
Equatorial Radius of the Moon	1737.4 [km]	[26]

E Halo Orbit Amplitudes

Throughout this work, the halo orbit amplitudes are expressed in a dimensionless unit. It is closely related with the system of equations 2.10. In order to give a more practical meaning for this units, this appendix present the conversion between them and the dimensions of the halo orbit in kilometers.

Tables E.1 and E.2 present the coordinates of the furthest points of the halo orbits in kilometers with respect to the CRTBP frame. The first present the data of orbits around Sun-Earth/Moon libration point 1, and the second of the SEL2.

Table E.1: Halo orbit amplitude conversions for the SEL1 libration point

Amplitude	Upper Furthest Point		Left Furthest Point		Bottom Furthest Point		Right Furthest Point	
[CRTBP units]	X Pos. [km]	Z Pos. [km]	X Pos. [km]	Y Pos. [km]	X Pos. [km]	Z Pos. [km]	X Pos. [km]	Y Pos. [km]
0.04	-1.483e+08	5.391e+04	-1.482e+08	6.614e+05	-1.479e+08	-6.689e+04	-1.482e+08	-6.614e+05
0.08	-1.483e+08	1.076e+05	-1.482e+08	6.696e+05	-1.479e+08	-1.340e+05	-1.482e+08	-6.696e+05
0.12	-1.484e+08	1.610e+05	-1.482e+08	6.832e+05	-1.479e+08	-2.015e+05	-1.482e+08	-6.832e+05
0.16	-1.484e+08	2.139e+05	-1.482e+08	7.016e+05	-1.479e+08	-2.697e+05	-1.482e+08	-7.016e+05
0.20	-1.484e+08	2.660e+05	-1.482e+08	7.246e+05	-1.479e+08	-3.387e+05	-1.482e+08	-7.246e+05
0.24	-1.484e+08	3.173e+05	-1.482e+08	7.516e+05	-1.479e+08	-4.088e+05	-1.482e+08	-7.516e+05
0.28	-1.484e+08	3.676e+05	-1.482e+08	7.822e+05	-1.479e+08	-4.801e+05	-1.482e+08	-7.822e+05

Table E.2: Halo orbit amplitude conversions for the SEL2 libration point

Amplitude	Upper Furthest Point		Left Furthest Point		Bottom Furthest Point		Right Furthest Point	
[CRTBP units]	X Pos. [km]	Z Pos. [km]	X Pos. [km]	Y Pos. [km]	X Pos. [km]	Z Pos. [km]	X Pos. [km]	Y Pos. [km]
0.04	-1.513e+08	6.773e+04	-1.510e+08	6.800e+05	-1.509e+08	-5.396e+04	-1.510e+08	-6.800e+05
0.08	-1.513e+08	1.357e+05	-1.510e+08	6.881e+05	-1.508e+08	-1.077e+05	-1.510e+08	-6.881e+05
0.12	-1.513e+08	2.041e+05	-1.510e+08	7.013e+05	-1.508e+08	-1.611e+05	-1.510e+08	-7.013e+05
0.16	-1.513e+08	2.731e+05	-1.510e+08	7.194e+05	-1.508e+08	-2.140e+05	-1.510e+08	-7.194e+05
0.20	-1.513e+08	3.430e+05	-1.510e+08	7.419e+05	-1.508e+08	-2.662e+05	-1.510e+08	-7.419e+05
0.24	-1.513e+08	4.139e+05	-1.510e+08	7.685e+05	-1.508e+08	-3.175e+05	-1.510e+08	-7.685e+05
0.28	-1.513e+08	4.862e+05	-1.510e+08	7.986e+05	-1.508e+08	-3.677e+05	-1.510e+08	-7.986e+05

F Transfer Trajectories Using the CRTBP with Low-Thrust

In this appendix is dedicated to present the numerical data from the most interesting transfer trajectories obtained using the simples model, i.e., the CRTBP only perturbed by the low-thrust propulsion.

Each of the transfers presented in tables F.1, F.2 and F.3 presents the most circular transfer trajectory associated with a given halo orbit amplitude, magnitude of the thrust and zones of low-eccentricity parking orbits. The distance from the halo orbit to the manifold is settled as $\alpha_2 = 10^{-3}$ and the check altitude is always 1000 km.

The column named “Circ. Tranf.” refers to the number of transfer trajectories found where the parking orbit has $e \leq 0.05$. It is important to give an idea of how large is the zone with low eccentricity transfer trajectories for each set of parameters.

Tables F.4, F.5 and F.6 contains the same parameters but with respect to the libration point 2 of the Sun-Earth/Moon system.

Table F.1: Sun-Earth/Moon Libration Point 1 Transfer Trajectories Zone 1

Zone 1										
Halo Amp. α_4 [CRTBP]	Thrust F_T [m/s^2]	ϕ [rad]	t_{coast} [CRTBP]	t_{coast} [days]	Circ. Tranf.	a [km]	e	i [degrees]	t_{total} [days]	t_{thrust} [days]
	$8.0{\cdot}10^{-5}$	4.565	2.480	144	0	14983	0.507861	3.20	819	675
	$9.0{\cdot}10^{-5}$	4.580	2.490	145	0	13173	0.440106	3.19	784	639
	$1.0{\cdot}10^{-4}$	4.585	2.500	145	0	11548	0.361405	3.19	760	614
	$1.5{\cdot}10^{-4}$	4.815	2.475	144	5	7518	0.018728	3.14	655	511
		4.415	2.585	150	5	7595	0.028611	3.24	659	508
	$2.0{\cdot}10^{-4}$	5.015	2.465	143	2	7692	0.040874	3.18	521	378
0.04		4.245	2.643	154	0	7774	0.051003	3.36	529	376
	$2.5{\cdot}10^{-4}$	5.150	2.465	143	0	7876	0.063493	3.24	441	298
		4.135	2.675	156	2	7721	0.044560	3.46	457	301
	$3.0{\cdot}10^{-4}$	5.235	2.475	144	3	7661	0.036957	3.30	396	252
		4.070	2.691	156	2	7594	0.028500	3.53	409	253
	$3.5{\cdot}10^{-4}$	5.315	2.480	144	2	7704	0.042467	3.36	359	215
		4.005	2.705	157	0	7992	0.077068	3.61	368	210
	$8.0{\cdot}10^{-5}$	4.575	2.485	144	0	14198	0.480712	6.40	838	693
	$9.0{\cdot}10^{-5}$	4.585	2.495	145	0	12417	0.405963	6.39	804	659
	$1.0{\cdot}10^{-4}$	4.590	2.505	146	0	10831	0.318941	6.38	781	635
	$1.5{\cdot}10^{-4}$	4.865	2.470	144	4	7626	0.032614	6.30	651	507
		4.380	2.605	151	4	7614	0.031152	6.54	659	508
	$2.0{\cdot}10^{-4}$	5.045	2.465	143	3	7572	0.025818	6.38	525	381
0.08		4.225	2.659	155	2	7683	0.039771	6.77	533	378
	$2.5{\cdot}10^{-4}$	5.170	2.470	144	3	7571	0.025534	6.50	448	305
		4.130	2.685	156	2	7622	0.032293	6.95	459	303
	$3.0{\cdot}10^{-4}$	5.265	2.475	144	0	7865	0.062220	6.63	392	248
		4.060	2.702	157	2	7664	0.037555	7.10	409	252
	$3.5{\cdot}10^{-4}$	5.335	2.485	144	3	7619	0.031915	6.74	361	216
		4.010	2.710	158	0	8018	0.080286	7.22	368	210
	$8.0{\cdot}10^{-5}$	4.585	2.495	145	0	12962	0.431114	9.62	871	726
	$9.0{\cdot}10^{-5}$	4.595	2.505	146	0	11237	0.343639	9.59	839	693
	$1.0{\cdot}10^{-4}$	4.605	2.515	146	0	9718	0.240875	9.57	818	672
	$1.5{\cdot}10^{-4}$	4.910	2.470	144	4	7642	0.034594	9.48	651	507
		4.345	2.630	153	3	7654	0.036026	9.92	659	507
	$2.0{\cdot}10^{-4}$	5.095	2.465	143	3	7642	0.034654	9.63	523	380
0.12		4.215	2.675	156	2	7667	0.037965	10.23	534	379
	$2.5{\cdot}10^{-4}$	5.210	2.475	144	2	7736	0.046591	9.80	445	301
		4.130	2.700	157	0	7800	0.054180	10.47	457	300
	$3.0{\cdot}10^{-4}$	5.305	2.480	144	0	7883	0.064273	10.00	392	248
		4.055	2.718	158	2	7545	0.022268	10.72	412	254
	$3.5{\cdot}10^{-4}$	5.375	2.490	145	3	7493	0.015374	10.18	363	218
		4.000	2.730	159	1	7687	0.040565	10.92	374	215
	$8.0{\cdot}10^{-5}$	4.610	2.505	146	0	11375	0.351700	12.83	922	776
	$9.0{\cdot}10^{-5}$	4.625	2.515	146	0	9742	0.242694	12.80	892	746
	$1.0{\cdot}10^{-4}$	4.630	2.525	147	0	8331	0.114517	12.78	875	728
	$1.5{\cdot}10^{-4}$	4.995	2.465	143	3	7573	0.025799	12.73	653	510
		4.320	2.660	155	3	7563	0.024480	13.38	665	510
	$2.0{\cdot}10^{-4}$	5.155	2.470	144	3	7516	0.018364	12.93	527	383
0.16		4.200	2.702	157	2	7592	0.028234	13.78	538	381
	$2.5{\cdot}10^{-4}$	5.265	2.480	144	3	7549	0.022730	13.17	449	305
		4.120	2.725	158	0	7781	0.052088	14.10	459	300
	$3.0{\cdot}10^{-4}$	5.355	2.490	145	3	7565	0.024770	13.43	398	254
		4.055	2.740	159	0	7883	0.064205	14.39	407	248
	$3.5{\cdot}10^{-4}$	5.430	2.500	145	0	7809	0.055455	13.68	359	213
		4.000	2.750	160	0	7945	0.071608	14.65	371	211

Table F.2: Sun-Earth/Moon Libration Point 1 Transfer Trajectories Zones 2 and 3

Halo Amp. α_4 [CRTBP]	Thrust F_T [m/s^2]	ϕ [rad]	t_{coast} [CRTBP]	t_{coast} [days]	Circ. Tranf.	a [km]	e	i [degrees]	t_{total} [days]	t_{thrust} [days]
Zone 2										
	$8.0{\cdot}10^{-5}$	4.455	3.560	207	1	7656	0.036404	3.24	1158	951
	$9.0{\cdot}10^{-5}$	4.465	3.565	207	1	7759	0.049201	3.25	1046	839
	$1.0{\cdot}10^{-4}$	4.480	3.570	208	1	7762	0.049530	3.26	962	755
0.04	$1.5{\cdot}10^{-4}$	4.525	3.595	209	0	7784	0.052278	3.32	710	501
	$2.0{\cdot}10^{-4}$	4.570	3.610	210	1	7749	0.048040	3.37	586	376
	$2.5{\cdot}10^{-4}$	4.600	3.620	210	1	7712	0.043461	3.41	512	301
	$3.0{\cdot}10^{-4}$	4.635	3.630	211	0	7821	0.056918	3.45	460	249
	$3.5{\cdot}10^{-4}$	4.660	3.635	211	1	7513	0.018026	3.48	429	218
	$8.0{\cdot}10^{-5}$	4.450	3.570	208	2	7736	0.046284	6.48	1153	946
	$9.0{\cdot}10^{-5}$	4.465	3.580	208	1	7634	0.033500	6.51	1055	846
	$1.0{\cdot}10^{-4}$	4.475	3.585	208	1	7584	0.027214	6.53	973	764
0.08	$1.5{\cdot}10^{-4}$	4.520	3.610	210	1	7714	0.043657	6.65	714	504
	$2.0{\cdot}10^{-4}$	4.560	3.625	211	1	7576	0.026110	6.74	592	381
	$2.5{\cdot}10^{-4}$	4.595	3.635	211	0	7842	0.059387	6.83	510	299
	$3.0{\cdot}10^{-4}$	4.625	3.645	212	1	7714	0.043566	6.90	463	251
	$3.5{\cdot}10^{-4}$	4.650	3.655	212	0	7894	0.065387	6.97	424	212
	$8.0{\cdot}10^{-5}$	4.445	3.590	209	0	7766	0.050010	9.74	1153	944
	$9.0{\cdot}10^{-5}$	4.460	3.605	210	1	7741	0.047071	9.78	1050	841
	$1.0{\cdot}10^{-4}$	4.470	3.610	210	1	7693	0.040986	9.82	969	759
0.12	$1.5{\cdot}10^{-4}$	4.515	3.635	211	1	7689	0.040513	9.99	716	505
	$2.0{\cdot}10^{-4}$	4.550	3.655	212	0	7832	0.058224	10.12	587	374
	$2.5{\cdot}10^{-4}$	4.580	3.665	213	0	7788	0.053039	10.24	513	300
	$3.0{\cdot}10^{-4}$	4.610	3.675	214	1	7543	0.021947	10.36	467	254
	$3.5{\cdot}10^{-4}$	4.635	3.685	214	0	7872	0.062888	10.46	427	212
	$8.0{\cdot}10^{-5}$	4.440	3.625	211	1	7674	0.038639	13.00	1162	951
	$9.0{\cdot}10^{-5}$	4.450	3.635	211	1	7743	0.047224	13.05	1052	841
	$1.0{\cdot}10^{-4}$	4.460	3.640	212	1	7699	0.041723	13.10	971	759
0.16	$1.5{\cdot}10^{-4}$	4.505	3.675	214	1	7761	0.049412	13.33	716	503
	$2.0{\cdot}10^{-4}$	4.540	3.690	215	0	7858	0.061158	13.52	588	374
	$2.5{\cdot}10^{-4}$	4.570	3.705	215	0	7816	0.056066	13.68	515	299
	$3.0{\cdot}10^{-4}$	4.595	3.715	216	0	7939	0.071160	13.82	463	247
	$3.5{\cdot}10^{-4}$	4.615	3.725	217	1	7684	0.039988	13.94	432	215
Zone 3										
	$8.0{\cdot}10^{-5}$	2.200	4.535	264	0	11011	0.330350	0.38	1237	974
	$9.0{\cdot}10^{-5}$	2.065	4.500	262	0	9825	0.249091	2.74	1003	742
	$1.0{\cdot}10^{-4}$	2.200	4.705	274	0	8008	0.078723	0.25	1226	953
0.04	$1.5{\cdot}10^{-4}$	1.995	4.240	246	2	7722	0.044519	2.86	750	504
	$2.0{\cdot}10^{-4}$	1.955	4.160	242	0	7848	0.060019	2.94	616	374
	$2.5{\cdot}10^{-4}$	1.915	4.100	238	1	7699	0.041629	3.01	540	302
	$3.0{\cdot}10^{-4}$	1.885	4.065	236	0	7783	0.052068	3.06	486	250
	$3.5{\cdot}10^{-4}$	1.850	4.025	234	0	7838	0.059123	3.12	447	213
	$8.0{\cdot}10^{-5}$	2.075	4.515	262	0	10690	0.310185	5.48	1062	800
	$9.0{\cdot}10^{-5}$	2.070	4.500	262	0	9108	0.190086	5.48	1033	772
	$1.0{\cdot}10^{-4}$	2.070	4.510	262	0	7804	0.054714	5.47	1015	753
0.08	$1.5{\cdot}10^{-4}$	2.000	4.240	246	1	7658	0.036714	5.72	753	506
	$2.0{\cdot}10^{-4}$	1.960	4.160	242	1	7634	0.033508	5.88	621	380
	$2.5{\cdot}10^{-4}$	1.925	4.110	239	1	7740	0.046892	6.01	540	301
	$3.0{\cdot}10^{-4}$	1.890	4.065	236	1	7559	0.024029	6.14	490	254
	$3.5{\cdot}10^{-4}$	1.860	4.035	235	0	7867	0.062430	6.24	447	212
	$8.0{\cdot}10^{-5}$	2.085	4.525	263	0	9498	0.223298	8.22	1113	850
	$9.0{\cdot}10^{-5}$	2.085	4.540	264	0	8028	0.081057	8.19	1089	825
	$1.0{\cdot}10^{-4}$	2.065	4.425	257	3	7602	0.029587	8.27	1022	764
0.12	$1.5{\cdot}10^{-4}$	2.010	4.240	246	0	7795	0.053496	8.58	748	502
	$2.0{\cdot}10^{-4}$	1.970	4.160	242	1	7612	0.030720	8.83	622	380
	$2.5{\cdot}10^{-4}$	1.935	4.110	239	1	7493	0.015386	9.04	545	306
	$3.0{\cdot}10^{-4}$	1.905	4.075	237	1	7712	0.043557	9.20	488	251
	$3.5{\cdot}10^{-4}$	1.870	4.035	235	1	7751	0.048393	9.38	449	214
	$8.0{\cdot}10^{-5}$	2.100	4.530	263	0	8064	0.085109	10.95	1191	927
	$9.0{\cdot}10^{-5}$	2.115	4.670	271	3	7679	0.039299	10.88	1117	846
	$1.0{\cdot}10^{-4}$	2.070	4.370	254	1	7665	0.037480	11.11	1015	761
0.16	$1.5{\cdot}10^{-4}$	2.025	4.235	246	0	7824	0.057177	11.47	747	501
	$2.0{\cdot}10^{-4}$	1.985	4.160	242	1	7659	0.036782	11.80	621	379
	$2.5{\cdot}10^{-4}$	1.955	4.120	240	1	7617	0.031395	12.05	543	304
	$3.0{\cdot}10^{-4}$	1.925	4.085	237	1	7657	0.036592	12.28	489	252
	$3.5{\cdot}10^{-4}$	1.895	4.050	235	0	7924	0.068956	12.50	447	212

Table F.3: Sun-Earth/Moon Libration Point 1 Transfer Trajectories Zone 4

Zone 4										
Halo Amp. α_4 [CRTBP]	Thrust F_T [m/s^2]	ϕ [rad]	t_{coast} [CRTBP]	t_{coast} [days]	Circ. Tranf.	a [km]	e	i [degrees]	t_{total} [days]	t_{thrust} [days]
0.04	$8.0{\cdot}10^{-5}$	4.310	4.340	252	0	7852	0.060366	3.11	1191	939
	$9.0{\cdot}10^{-5}$	4.305	4.360	253	0	7859	0.061218	3.11	1087	833
	$1.0{\cdot}10^{-4}$	4.300	4.375	254	0	7974	0.074932	3.12	998	744
	$1.5{\cdot}10^{-4}$	4.285	4.430	258	0	8089	0.088042	3.12	749	491
	$2.0{\cdot}10^{-4}$	4.270	4.475	260	0	7940	0.070944	3.14	632	372
	$2.5{\cdot}10^{-4}$	4.260	4.500	262	0	8330	0.114548	3.16	551	289
	$3.0{\cdot}10^{-4}$	4.250	4.530	263	0	7933	0.070403	3.18	510	247
	$3.5{\cdot}10^{-4}$	4.240	4.555	265	0	8136	0.093721	3.21	473	208
0.08	$8.0{\cdot}10^{-5}$	4.315	4.355	253	1	7688	0.040346	6.23	1203	950
	$9.0{\cdot}10^{-5}$	4.310	4.375	254	1	7667	0.037817	6.23	1099	845
	$1.0{\cdot}10^{-4}$	4.305	4.395	255	1	7686	0.040118	6.23	1015	759
	$1.5{\cdot}10^{-4}$	4.285	4.460	259	0	7830	0.057928	6.27	759	500
	$2.0{\cdot}10^{-4}$	4.275	4.495	261	0	8289	0.110073	6.29	625	363
	$2.5{\cdot}10^{-4}$	4.260	4.535	264	0	8318	0.113474	6.35	553	289
	$3.0{\cdot}10^{-4}$	4.255	4.550	265	0	7995	0.077313	6.37	511	246
	$3.5{\cdot}10^{-4}$	4.245	4.575	266	0	8054	0.084083	6.43	476	210
0.12	$8.0{\cdot}10^{-5}$	4.320	4.395	255	0	8130	0.092607	9.36	1178	922
	$9.0{\cdot}10^{-5}$	4.315	4.410	256	0	7858	0.061273	9.36	1091	834
	$1.0{\cdot}10^{-4}$	4.310	4.430	258	1	7726	0.045202	9.37	1015	757
	$1.5{\cdot}10^{-4}$	4.290	4.500	262	0	8198	0.100133	9.43	750	488
	$2.0{\cdot}10^{-4}$	4.280	4.535	264	1	7656	0.036316	9.47	643	379
	$2.5{\cdot}10^{-4}$	4.270	4.565	265	1	7638	0.034061	9.54	569	303
	$3.0{\cdot}10^{-4}$	4.260	4.595	267	0	8240	0.104755	9.63	509	242
	$3.5{\cdot}10^{-4}$	4.255	4.610	268	1	7732	0.046179	9.67	482	214
0.16	$8.0{\cdot}10^{-5}$	4.325	4.450	259	1	7650	0.035525	12.52	1212	953
	$9.0{\cdot}10^{-5}$	4.320	4.475	260	2	7679	0.039314	12.54	1105	845
	$1.0{\cdot}10^{-4}$	4.315	4.495	261	0	7999	0.077780	12.56	1005	744
	$1.5{\cdot}10^{-4}$	4.300	4.555	265	0	7934	0.070075	12.63	762	497
	$2.0{\cdot}10^{-4}$	4.290	4.590	267	1	7764	0.049923	12.70	643	376
	$2.5{\cdot}10^{-4}$	4.280	4.620	269	1	7639	0.034253	12.81	572	303
	$3.0{\cdot}10^{-4}$	4.275	4.640	270	0	8444	0.126722	12.87	509	239
	$3.5{\cdot}10^{-4}$	4.265	4.665	271	0	8358	0.117621	13.04	477	206

Table F.4: Sun-Earth/Moon Libration Point 2 Transfer Trajectories Zone 1

Zone 1										
Halo Amp. α_4 [CRTBP]	Thrust F_T [m/s^2]	ϕ [rad]	t_{coast} [CRTBP]	t_{coast} [days]	Circ. Tranf.	a [km]	e	i [degrees]	t_{total} [days]	t_{thrust} [days]
	$8.0{\cdot}10^{-5}$	1.450	2.525	147	0	13466	0.452450	3.20	859	712
	$9.0{\cdot}10^{-5}$	1.465	2.535	147	0	11706	0.370244	3.19	826	679
	$1.0{\cdot}10^{-4}$	1.470	2.545	148	0	10158	0.273757	3.18	804	656
	$1.5{\cdot}10^{-4}$	1.760	2.505	146	3	7527	0.019916	3.15	657	511
		1.225	2.655	154	4	7647	0.035201	3.29	661	507
	$2.0{\cdot}10^{-4}$	1.945	2.500	145	4	7585	0.027433	3.19	526	381
0.04		1.085	2.705	157	2	7646	0.035208	3.39	537	379
	$2.5{\cdot}10^{-4}$	2.065	2.505	146	0	7884	0.064336	3.25	444	298
		1.000	2.730	159	2	7542	0.021827	3.47	464	305
	$3.0{\cdot}10^{-4}$	2.150	2.515	146	3	7588	0.027864	3.31	399	253
		0.935	2.745	160	2	7718	0.044328	3.54	410	251
	$3.5{\cdot}10^{-4}$	2.225	2.525	147	0	7809	0.055622	3.37	360	213
		0.880	2.755	160	0	7995	0.077689	3.61	371	211
	$8.0{\cdot}10^{-5}$	1.460	2.530	147	0	12755	0.421859	6.39	879	732
	$9.0{\cdot}10^{-5}$	1.470	2.540	148	0	11034	0.331422	6.38	847	700
	$1.0{\cdot}10^{-4}$	1.475	2.550	148	0	9524	0.225488	6.37	827	679
	$1.5{\cdot}10^{-4}$	1.790	2.505	146	4	7694	0.041119	6.31	651	505
		1.220	2.665	155	4	7599	0.029195	6.60	664	509
	$2.0{\cdot}10^{-4}$	1.970	2.500	145	2	7722	0.044614	6.41	523	377
0.08		1.080	2.715	158	2	7526	0.019676	6.81	541	383
	$2.5{\cdot}10^{-4}$	2.085	2.510	146	3	7565	0.024757	6.52	451	305
		0.995	2.740	159	2	7522	0.019184	6.98	465	306
	$3.0{\cdot}10^{-4}$	2.170	2.520	146	0	7799	0.054189	6.64	396	249
		0.930	2.755	160	1	7684	0.039996	7.12	412	251
	$3.5{\cdot}10^{-4}$	2.245	2.525	147	0	7896	0.065677	6.76	359	212
		0.875	2.765	161	0	7907	0.067081	7.25	373	212
	$8.0{\cdot}10^{-5}$	1.470	2.540	148	0	11635	0.366128	9.60	915	767
	$9.0{\cdot}10^{-5}$	1.480	2.550	148	0	9979	0.260693	9.58	885	737
	$1.0{\cdot}10^{-4}$	1.500	2.555	149	0	8545	0.136735	9.55	867	719
	$1.5{\cdot}10^{-4}$	1.850	2.500	145	3	7561	0.024245	9.51	656	510
		1.190	2.690	156	3	7624	0.032306	10.00	664	508
	$2.0{\cdot}10^{-4}$	2.010	2.505	146	2	7619	0.031599	9.66	526	380
0.12		1.065	2.735	159	1	7726	0.045024	10.31	536	377
	$2.5{\cdot}10^{-4}$	2.120	2.515	146	2	7711	0.043296	9.83	448	302
		0.990	2.755	160	0	7856	0.061018	10.53	459	299
	$3.0{\cdot}10^{-4}$	2.210	2.525	147	0	7786	0.052483	10.02	397	250
		0.920	2.775	161	0	7960	0.073326	10.76	408	247
	$3.5{\cdot}10^{-4}$	2.285	2.530	147	0	8052	0.083903	10.21	357	210
		0.865	2.785	162	0	7937	0.070722	10.96	373	211
	$8.0{\cdot}10^{-5}$	1.495	2.550	148	0	10210	0.277614	12.81	969	820
	$9.0{\cdot}10^{-5}$	1.495	2.565	149	0	8655	0.147642	12.80	943	794
	$1.0{\cdot}10^{-4}$	1.570	2.550	148	33	7500	0.016298	12.72	919	771
	$1.5{\cdot}10^{-4}$	1.910	2.500	145	3	7540	0.021513	12.75	657	511
		1.180	2.715	158	3	7682	0.039702	13.44	664	506
	$2.0{\cdot}10^{-4}$	2.060	2.510	146	2	7738	0.046740	12.95	523	377
0.16		1.055	2.760	160	2	7683	0.039637	13.87	539	379
	$2.5{\cdot}10^{-4}$	2.175	2.520	146	3	7495	0.015663	13.21	453	307
		0.980	2.780	162	2	7709	0.043004	14.17	464	302
	$3.0{\cdot}10^{-4}$	2.260	2.530	147	2	7671	0.038203	13.45	399	252
		0.920	2.795	162	2	7616	0.031312	14.44	415	253
	$3.5{\cdot}10^{-4}$	2.335	2.540	148	2	7675	0.038993	13.71	363	215
		0.865	2.805	163	2	7641	0.034588	14.71	379	216

Table F.5: Sun-Earth/Moon Libration Point 2 Transfer Trajectories Zones 2 and 3

Halo Amp. α_4 [CRTBP]	Thrust F_T [m/s^2]	ϕ [rad]	t_{coast} [CRTBP]	t_{coast} [days]	Circ. Tranf.	a [km]	e	i [degrees]	t_{total} [days]	t_{thrust} [days]
Zone 2										
0.04	$8.0{\cdot}10^{-5}$	1.320	3.620	210	1	7508	0.017260	3.24	1172	962
	$9.0{\cdot}10^{-5}$	1.330	3.625	211	1	7646	0.035059	3.25	1057	846
	$1.0{\cdot}10^{-4}$	1.340	3.635	211	1	7644	0.034882	3.26	973	761
	$1.5{\cdot}10^{-4}$	1.385	3.660	213	1	7648	0.035449	3.32	719	506
	$2.0{\cdot}10^{-4}$	1.425	3.675	214	0	7771	0.050848	3.37	589	376
	$2.5{\cdot}10^{-4}$	1.455	3.690	215	1	7729	0.045673	3.41	516	301
	$3.0{\cdot}10^{-4}$	1.485	3.700	215	0	7922	0.069043	3.45	462	247
	$3.5{\cdot}10^{-4}$	1.505	3.705	215	1	7743	0.047528	3.48	430	214
0.08	$8.0{\cdot}10^{-5}$	1.315	3.630	211	1	7670	0.038056	6.48	1162	951
	$9.0{\cdot}10^{-5}$	1.325	3.640	212	1	7712	0.043344	6.51	1054	842
	$1.0{\cdot}10^{-4}$	1.335	3.645	212	1	7715	0.043750	6.53	970	758
	$1.5{\cdot}10^{-4}$	1.380	3.675	214	1	7644	0.034832	6.65	720	507
	$2.0{\cdot}10^{-4}$	1.415	3.690	215	0	7866	0.062158	6.74	588	374
	$2.5{\cdot}10^{-4}$	1.450	3.705	215	1	7703	0.042240	6.83	517	302
	$3.0{\cdot}10^{-4}$	1.475	3.715	216	1	7481	0.013749	6.90	471	255
	$3.5{\cdot}10^{-4}$	1.500	3.725	217	0	7943	0.071202	6.97	428	211
0.12	$8.0{\cdot}10^{-5}$	1.310	3.655	212	0	7784	0.052213	9.73	1156	944
	$9.0{\cdot}10^{-5}$	1.320	3.660	213	1	7746	0.047518	9.77	1054	841
	$1.0{\cdot}10^{-4}$	1.330	3.670	213	1	7658	0.036640	9.81	974	761
	$1.5{\cdot}10^{-4}$	1.375	3.700	215	1	7662	0.037036	9.98	721	506
	$2.0{\cdot}10^{-4}$	1.410	3.720	216	1	7677	0.039080	10.13	595	379
	$2.5{\cdot}10^{-4}$	1.440	3.735	217	0	7843	0.059645	10.25	516	299
	$3.0{\cdot}10^{-4}$	1.465	3.745	218	0	7785	0.052432	10.36	467	250
	$3.5{\cdot}10^{-4}$	1.485	3.750	218	0	8001	0.078244	10.45	429	211
0.16	$8.0{\cdot}10^{-5}$	1.305	3.685	214	1	7765	0.049922	13.00	1160	946
	$9.0{\cdot}10^{-5}$	1.315	3.695	215	1	7694	0.041122	13.05	1059	844
	$1.0{\cdot}10^{-4}$	1.325	3.705	215	1	7595	0.028704	13.10	980	765
	$1.5{\cdot}10^{-4}$	1.365	3.735	217	1	7719	0.044243	13.32	722	505
	$2.0{\cdot}10^{-4}$	1.400	3.760	219	0	7817	0.056128	13.51	594	375
	$2.5{\cdot}10^{-4}$	1.425	3.775	219	1	7747	0.047864	13.66	520	301
	$3.0{\cdot}10^{-4}$	1.450	3.785	220	1	7741	0.047046	13.81	471	251
	$3.5{\cdot}10^{-4}$	1.470	3.795	221	1	7691	0.041094	13.94	436	215
Zone 3										
0.04	$8.0{\cdot}10^{-5}$	5.230	4.560	265	0	10201	0.276957	2.75	1085	820
	$9.0{\cdot}10^{-5}$	5.230	4.575	266	0	8662	0.148414	2.74	1058	792
	$1.0{\cdot}10^{-4}$	5.220	4.525	263	6	7476	0.013151	2.75	1034	771
	$1.5{\cdot}10^{-4}$	5.155	4.290	249	0	7847	0.059876	2.86	749	500
	$2.0{\cdot}10^{-4}$	5.110	4.205	244	1	7557	0.023840	2.95	626	382
	$2.5{\cdot}10^{-4}$	5.070	4.150	241	0	7839	0.058897	3.02	540	299
	$3.0{\cdot}10^{-4}$	5.040	4.115	239	1	7708	0.042986	3.07	490	251
	$3.5{\cdot}10^{-4}$	5.000	4.070	237	0	7946	0.072040	3.14	448	211
0.08	$8.0{\cdot}10^{-5}$	5.235	4.555	265	0	9550	0.227565	5.50	1113	848
	$9.0{\cdot}10^{-5}$	5.235	4.575	266	0	8087	0.087834	5.48	1088	822
	$1.0{\cdot}10^{-4}$	5.215	4.465	260	2	7554	0.023277	5.53	1027	767
	$1.5{\cdot}10^{-4}$	5.160	4.290	249	0	7771	0.050634	5.73	752	503
	$2.0{\cdot}10^{-4}$	5.115	4.205	244	1	7726	0.045156	5.90	622	377
	$2.5{\cdot}10^{-4}$	5.080	4.155	242	1	7611	0.030737	6.03	545	304
	$3.0{\cdot}10^{-4}$	5.045	4.115	239	1	7606	0.030214	6.15	492	253
	$3.5{\cdot}10^{-4}$	5.015	4.085	237	1	7737	0.046785	6.25	452	214
0.12	$8.0{\cdot}10^{-5}$	5.250	4.595	267	0	8499	0.132182	8.22	1169	902
	$9.0{\cdot}10^{-5}$	5.235	4.510	262	3	7521	0.018999	8.26	1117	855
	$1.0{\cdot}10^{-4}$	5.220	4.440	258	0	7776	0.051197	8.32	1014	756
	$1.5{\cdot}10^{-4}$	5.165	4.270	248	0	7839	0.058790	8.64	749	500
	$2.0{\cdot}10^{-4}$	5.130	4.215	245	0	7844	0.059628	8.84	619	374
	$2.5{\cdot}10^{-4}$	5.095	4.165	242	1	7744	0.047394	9.04	543	301
	$3.0{\cdot}10^{-4}$	5.060	4.125	240	0	7941	0.070912	9.23	487	247
	$3.5{\cdot}10^{-4}$	5.025	4.085	237	0	7881	0.063924	9.41	450	212
0.16	$8.0{\cdot}10^{-5}$	5.260	4.560	265	4	7621	0.031847	10.98	1221	956
	$9.0{\cdot}10^{-5}$	5.240	4.445	258	1	7574	0.025903	11.10	1111	852
	$1.0{\cdot}10^{-4}$	5.225	4.380	255	0	7863	0.061806	11.21	1006	751
	$1.5{\cdot}10^{-4}$	5.180	4.270	248	0	7901	0.066168	11.54	747	498
	$2.0{\cdot}10^{-4}$	5.145	4.210	245	0	7807	0.055042	11.83	620	376
	$2.5{\cdot}10^{-4}$	5.110	4.165	242	0	7783	0.052293	12.10	542	300
	$3.0{\cdot}10^{-4}$	5.085	4.140	241	0	7845	0.059912	12.28	490	249
	$3.5{\cdot}10^{-4}$	5.050	4.100	238	0	7854	0.061126	12.53	451	213

Table F.6: Sun-Earth/Moon Libration Point 2 Transfer Trajectories Zone 4

Zone 4										
Halo Amp. α_4 [CRTBP]	Thrust F_T [m/s^2]	ϕ [rad]	t_{coast} [CRTBP]	t_{coast} [days]	Circ. Tranf.	a [km]	e	i [degrees]	t_{total} [days]	t_{thrust} [days]
0.04	$8.0{\cdot}10^{-5}$	1.190	4.420	257	0	7771	0.050619	3.11	1201	944
	$9.0{\cdot}10^{-5}$	1.185	4.440	258	1	7615	0.031179	3.11	1106	848
	$1.0{\cdot}10^{-4}$	1.180	4.460	259	1	7641	0.034461	3.12	1021	762
	$1.5{\cdot}10^{-4}$	1.165	4.515	262	0	8178	0.098091	3.12	751	489
	$2.0{\cdot}10^{-4}$	1.150	4.560	265	1	7756	0.048833	3.15	641	376
	$2.5{\cdot}10^{-4}$	1.140	4.590	267	0	7830	0.057967	3.17	566	299
	$3.0{\cdot}10^{-4}$	1.130	4.620	269	0	8086	0.087731	3.20	513	244
	$3.5{\cdot}10^{-4}$	1.125	4.635	269	1	7635	0.033762	3.22	485	216
0.08	$8.0{\cdot}10^{-5}$	1.190	4.450	259	0	7876	0.063220	6.24	1196	938
	$9.0{\cdot}10^{-5}$	1.185	4.470	260	0	7991	0.076754	6.24	1087	827
	$1.0{\cdot}10^{-4}$	1.185	4.475	260	0	8047	0.083240	6.23	1001	741
	$1.5{\cdot}10^{-4}$	1.165	4.545	264	0	7830	0.057829	6.28	765	500
	$2.0{\cdot}10^{-4}$	1.155	4.580	266	0	8011	0.079297	6.31	636	370
	$2.5{\cdot}10^{-4}$	1.145	4.610	268	0	8033	0.081744	6.35	563	295
	$3.0{\cdot}10^{-4}$	1.135	4.640	270	0	7861	0.061790	6.42	518	248
	$3.5{\cdot}10^{-4}$	1.130	4.655	271	0	7864	0.062011	6.45	483	213
0.12	$8.0{\cdot}10^{-5}$	1.195	4.485	261	1	7676	0.038812	9.38	1212	951
	$9.0{\cdot}10^{-5}$	1.190	4.505	262	0	7939	0.070807	9.39	1092	830
	$1.0{\cdot}10^{-4}$	1.190	4.510	262	0	8159	0.096026	9.36	998	736
	$1.5{\cdot}10^{-4}$	1.170	4.585	267	0	8106	0.089930	9.46	758	491
	$2.0{\cdot}10^{-4}$	1.160	4.620	269	1	7742	0.047135	9.51	646	377
	$2.5{\cdot}10^{-4}$	1.150	4.655	271	0	7967	0.074378	9.60	567	296
	$3.0{\cdot}10^{-4}$	1.145	4.670	271	0	8180	0.098298	9.64	515	243
	$3.5{\cdot}10^{-4}$	1.135	4.700	273	0	8614	0.144020	9.77	476	202
0.16	$8.0{\cdot}10^{-5}$	1.200	4.545	264	0	8165	0.096437	12.57	1185	921
	$9.0{\cdot}10^{-5}$	1.200	4.550	265	0	7902	0.066459	12.54	1097	833
	$1.0{\cdot}10^{-4}$	1.195	4.575	266	1	7743	0.047222	12.57	1023	757
	$1.5{\cdot}10^{-4}$	1.180	4.635	269	1	7660	0.036816	12.66	776	507
	$2.0{\cdot}10^{-4}$	1.170	4.675	272	1	7746	0.047620	12.75	649	377
	$2.5{\cdot}10^{-4}$	1.160	4.705	274	0	8164	0.096552	12.89	566	293
	$3.0{\cdot}10^{-4}$	1.155	4.725	275	1	7704	0.042381	12.97	526	251
	$3.5{\cdot}10^{-4}$	1.150	4.745	276	0	8272	0.108612	13.06	483	207

G Near-Earth Perturbations

In both, two-body and restricted three-body problems, all bodies involved are considered in the equations as point masses located at their center of mass. It can be proved that this assumption is only valid if the density of the bodies only depends on the distance from its center of mass, i.e., if they have spherical symmetry in density [15].

Nevertheless, the Earth and other celestial bodies are not perfect spheres. Moreover, other forces, different from the gravitational from the Earth and Sun (in the case of the CRTBP), act in a spacecraft.

All the set of forces different from the main gravitational attraction are called *perturbation forces*. The magnitude of each one depend on different parameters, thus depending on the spacecraft position, velocity and characteristics, one of them can have a considerable order of magnitude to affect the main motion of the spacecraft.

In the situation studied in this work, the satellite develops a spiral trajectory around Earth due to the low-thrust characteristics. Therefore, it may be affected by the strongest perturbation forces in Earth-vicinity. Figure G.1 presents the order of magnitude of several perturbations forces that act in a spacecraft near the Earth.

The plots were made with reference to the two-body problem, therefore the sun is one of the perturbation forces presented. In the case of the CRTBP its contribution is already counted in the main model.

Observing the figure the most important perturbation forces are:

1. Earth gravity harmonics (represented by the curves labeled $J_{2,0}$, $J_{2,2}$ and $J_{6,6}$);
2. Atmospheric drag;
3. Solar radiation pressure.

The moon gravitational attraction is also a major perturbation, but its influence is not going to be in the account in this part of the work. This will be true only when the full ephemerides data will be used, as explained in section 6.

The objective of this section is to present a quick introduction as well as how these perturbation forces are modeled. These perturbations have been applied to the CRTBP model and imple-

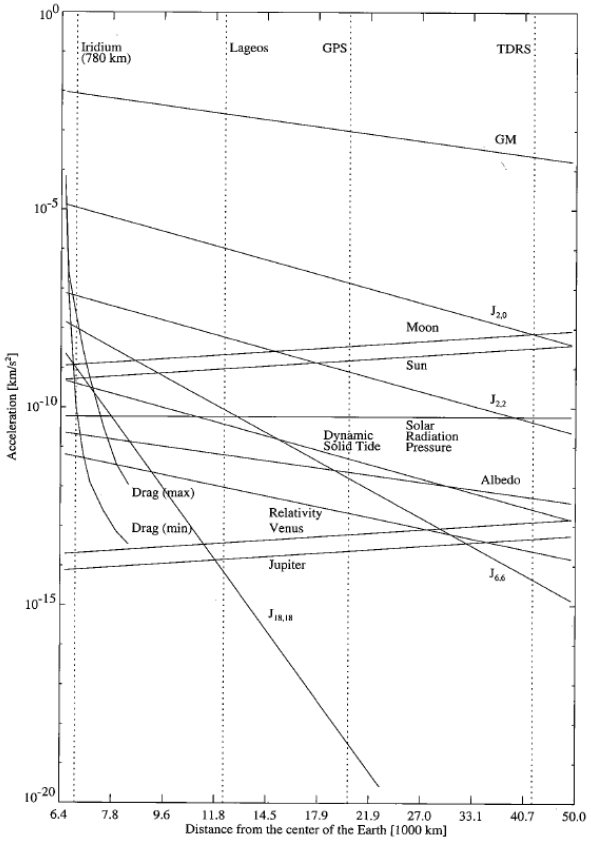

Figure G.1: Order of magnitude of various perturbations of a spacecraft near Earth, copied from reference [15]

mented in the second vectorfield camp experienced in this work, as will be presented in the next section.

There are several models for each perturbation force in the literature. In this work we compare some of the models and explain our choices. The basic references used has been:

Montenbruck's book [15] which present a great introduction to each of the perturbation forces and models for each one of them. Moreover, it provide a series of routines written in C++ to model each of them.

ESA Stardard ECSS-E-10-04A [6] which is the ESA standards to model the space environment conditions. It also contains good introduction to the main perturbation force and defines the models to be applied.

NASA ModelWeb [20] which contain links to various models and routines available for public use.

G.1 Gravity Harmonics

G.1.1 Introduction

As explained above, the assumption of point mass to formulate the gravitational attraction that the Earth exert in a spacecraft is not valid since it does not have a spherically symmetric density distribution.

In order to express mathematically the effect of its irregular shape, the gravitational potential is expressed as a series. The constants of this series are the so called *gravity harmonics*. Like in other mathematical series, the magnitude of the terms decrease with its order, therefore the more terms we use in the gravity acceleration calculation, the most precise is the model.

G.1.2 Mathematical Development

In the case of a point mass, the force acting in second body can be expressed as the gradient of the gravity potential

$$\ddot{\mathbf{r}} = \nabla U \qquad\qquad U = GM_{\oplus}\frac{1}{r} \tag{G.1}$$

where $\mathbf{r}$ is the vector from the main body (Earth) to the spacecraft position.

In order to find the Earth's real potential, the idea is to use a spheroid that can closely represent the shape and the mass distribution of the Earth. The gravity potential exerted by any body can be expressed by the sum of the contributions of each individual elemental mass of the body:

$$U = G\int \frac{\rho\,(\mathbf{r})\,d^3\mathbf{s}}{|\mathbf{r}-\mathbf{s}|} \tag{G.2}$$

where $\mathbf{s}$ and $\mathbf{r}$ are the distances from the origin to the mass particle and to the second body (spacecraft), respectively.

After some lengthy mathematical integrations, its is possible to write this potential as

$$U = \frac{GM_{\oplus}}{r}\sum_{n=0}^{\infty}\sum_{m=0}^{n}\left(\frac{R_{\oplus}}{r}\right)^2 P_{n,m}\,(sin\phi)\,(C_{n,m}cos(m\lambda)+S_{n,m}sin(m\lambda)) \tag{G.3}$$

where ϕ is the geocentric latitude of the body, and λ is its longitute counted positively towards the East.

$P_{n,m}$ is the associated Lagendre polynomial of degree n and order m, defined as

$$P_{n,m} = (1-u^2)\frac{d^m}{du^m}P_n(u) \tag{G.4}$$

$C_{n,m}$ and $S_{n,m}$ are called the *gravity harmonics*, and are dependent of the body's internal density distribution. They are used grouped in three different sets:

Zonal coefficients it can be observed from equation G.3 that if $m = 0$, then the dependency on the longitude (λ) vanishes, as well as the term containing $S_{n,m}$. Thus, the terms $C_{n,0}$ form one set and receive this designation. It is common to use the symbols: $J_n = -C_{n,0}$;

Sectorial coefficients terms with $n = m$.;

Tesseral coefficients all other terms, that is, those with $m < n$.

Some of these coefficients are special and it is interesting to point out,

$\mathbf{C_{0,0}}$ is always equal to 1. Thus, the first term of the gravity series is equal to the potential of a point mass;

$\mathbf{S_{n,0}}$ are not important since all terms of the series with these coefficients vanishes;

$\mathbf{C_{1,0}}$ **,** $\mathbf{C_{1,1}}$ **,** $\mathbf{S_{1,1}}$ it can be proved that they are equal to the coordinates of the body center of mass adimensionalized by the body radius. Therefore, if the origin is chosen to be at the body's center of mass, they all vanish;

$\mathbf{C_{2,1}}$ **and** $\mathbf{S_{1,2}}$ it can be proved that they vanish if the z-axis is aligned with the Earth's main axis of inertia.

$\mathbf{C_{2,0} = -J_2}$ is the bigger harmonic coefficient after the $C_{0,0}$, and it is three orders of magnitude bigger than the next one. Thus, some models of perturbations are restricted to it. It is related to the Earth equatorial oblateness, i.e., the difference between the equatorial and polar radius that is estimated in 22km.

Usually the Earth gravity models present the normalized coefficients to avoid their wide range in order of magnitude. They are defined as:

$$\left\{ \begin{array}{c} \bar{C}_{n,m} \\ \bar{S}_{n,m} \end{array} \right\} = \sqrt{\frac{(n-m)!}{(2-\delta_{0,m})(2n+1)(n-m)!}} \left\{ \begin{array}{c} C_{n,m} \\ S_{n,m} \end{array} \right\} \tag{G.5}$$

where $\delta_{0,m}$ the Kronecker's delta: $\delta_{0,m} = \left\{ \begin{array}{l} 1 \text{ if } m = 0 \\ 0 \text{ if } m \neq 0 \end{array} \right.$.

G.1.3 Earth Gravity Models

The mathematical developments present above apply to any body. In this work, however, only the Earth harmonics will be used, since it is the only celestial body from which the spacecraft gets closer enough to the gravity harmonic perturbations be noted.

As stated above, the gravity harmonics depends on the Earth internal mass distribution and shape, which cannot be known directly. Nevertheless, their value can be determined by indirect methods such as satellite geodesy, surface gravimetry and altimetry data.

Besides the harmonic coefficients, each model have its own mandarory set of parameters with the values for $GM_\oplus$ and for the Earth equatorial radius $R_\oplus$.

The first models were developed after the launch of Sputnick and numerous are public available. ESA recommends, in its latest report about standardization of space engineering [6], the use of the JGM2 model. However, in this report from the year 2000, it is already mentioned that the EGM96 could be its successor. NASA makes available the EGM96 coefficients at its models home page [20]. Montenbruck sugests the use of JGM3 [15].

All these and numerous other models can be found in the International Center for Global Gravity Field Models (ICGEM) web page [24]. Considering that EGM96 is the most used nowadays, it has been the model chosen to be used in this work.

G.1.4 Computation of Gravitational Perturbative Accelerations

Although the model coefficients are widely available in internet, the algorithms to calculate the resulting gravity acceleration in a spacecraft located at a point in the space are not. The potential presented in equation G.3 must be differentiated to provide the accelerations, which is not an easy task.

Montenbruck presents in his book [15] a method created by Cunningham in 1970 to accomplish it. It is very useful for numerical integrations since it is based in simple recursion formulas that can be easily programmed.

However, the method needs a rotation matrix to transform the coordinates of a point from a geocentric Earth-fixed reference frame to a geocentric ”quasi-inertial” reference frame. In a low accuracy calculation, only the Earth rotation can be taken into account in this matrix.

In order to calculate the gravitaty harmanic perturbations, a set of routines in C code were written, tested and used. This procedure was followed since the available set of routines had problems that difficult their use.

The Montenbruck routines are written in C++ code, that would take more time to be analyzed and integrated with the main program. The other set of routines were written in Fortran but used a unknown procedure for acceleration calculation and a uncommon normalization for the harmonic coefficients, which makes difficult the use of other set of coefficients, for example of another planet.

Two procedures were used to validate the written set of functions. The first one was based in comparing its results (gravity accelerations at a given point) with the ones calculated used the availableFortran set of subroutines.

As the information of this set of subroutines explains that the coefficients used were based in the GEM6 model, we used the same model with the function developed to make a proper comparison of results.

The comparison was made comparing the values of accelerations for different rotation matrices (that is, for different Greenwich sidereal angles), different positions of the spacecraft and different orders of zonal and tesseral terms.

An example of this comparisons is shown in figure G.2. It can be seen that the differences found are in order of magnitude of $10^{-8}m/s^2$ where the gravity perturbations (without the $C_{0,0}$ term) for the coordinates used have order of magnitude of $10^{-2}m/s^2$. Therefore, the two results agree very closely.

Another way of validating the set of functions developed is to use it in the numerical integration of an orbit during a period of time and comparing the results with analytical known ones.

The effects of the Earth's oblateness, represented by the $J_2 = -C_{2,0}$ harmonic term, in satellite orbit theory are well known. The main ones are the secular motions of the ascending node Ω and of the argument of perigee ω.

The Earth's equatorial bulge introduces a force component towards the equator that results in a gyroscopic precession of the orbit using a linear truncation. The resulting ascending node rate can be approximated by [5]

$$\dot{\Omega} = \frac{-9.9639}{(1-e^2)^2}\left(\frac{R}{R+\bar{h}}\right)^{3.5}\cos i \quad \text{[degrees/mean solar day]} \tag{G.6}$$

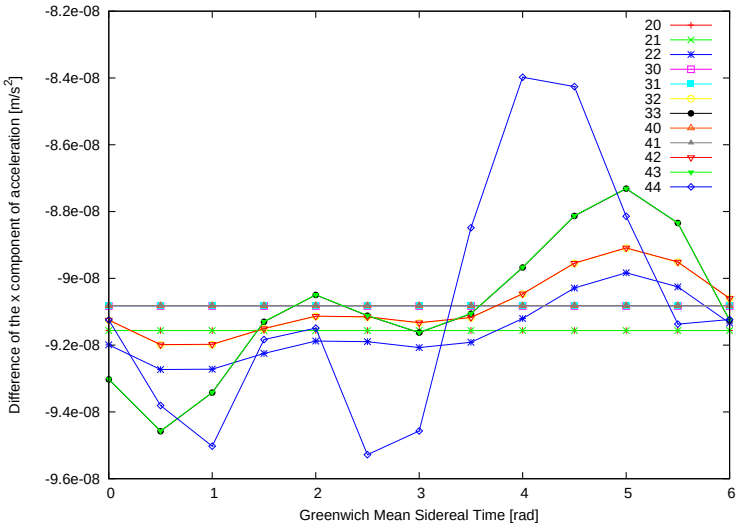

Figure G.2: Comparation of results of the two set of function

where $\bar{h}$ is the mean altitude of perigee and apogee.

In a similar way, since the gravitational force is no longer proportional to the square of the distance, the orbit is no longer a closed ellipse. The consequence is a motion of the perigee that can be approximated by [5]

$$\dot{\omega} = \frac{-9.9639}{(1-e^2)^2}\left(\frac{R}{R+\bar{h}}\right)^{3.5}\left(2-\frac{5}{2}\sin i\right) \quad \text{[degrees/mean solar day]} \tag{G.7}$$

The determination of these rates from the results of the numerical integration were done using a minimum squares method and plotting the results with GNUPLOT. During the evaluation of the analytical equations, it must be noted that not only Ω and ω are not fixed as a result of the Earth's oblateness, but all orbital elements experience variations. Thus, the mean values of the orbital elements obtained by the numerical integration were used.

Table G.1 presents the results of this comparisons. As it can be seen, the difference in both cases have an order of magnitude of 10^{-2} degrees by mean solar day, which is small enough to approve the use of this set of functions.

Table G.1: Values of calculated osculating orbital parameters' rate in degrees / day. The orbit used is a typical ISS orbit, with $a = 6714.8[km]$ $e = 0.001$ and $i = 51.6°$

Method	Ascending Node	Argument of Perigee
Integration	5.1549	3.8541
Analytical	5.1464	3.8319

G.2 Atmospheric Drag

G.2.1 Introduction

Although the Earth atmosphere present a very low density even at normal Low-Earth Orbit (LEO) altitudes, the resulting force of its interaction with the spacecraft's surface is the largest non-gravitational perturbation acting in this kind of orbits. It is considered that the Earth atmosphere has a thickness of 480km, but 80% of its density is located at the first 16km. However, usually the altitude of 1000km is set as the limit of atmospheric influence in spacecraft.

Different from the gravitational harmonics, the atmosphere perturbation is extremely difficult to be modeled from three points of view [15]: the physical properties of atmosphere, particularly its density at high altitudes, is still unknown; the modeling of the forces requires detailed knowledge of the interaction of the air particles with the spacecraft surface; and the varying altitude for non-spherical orbits must be taken into account.

The dominant atmospheric force is the *drag* which is the component of the force that is parallel to the spacecraft's velocity vector. The other components (lift and binormal) in most cases can be safely neglected [15].

One important characteristic of the drag perturbation is that it is a non-conservative force. Therefore, it continuously takes out energy from the spacecraft. Thus its main effect is to reduce the semi-major axis value. In eccentric orbits, the drag action is stronger at the perigee, thus another of its effects is to reduce the eccentricity of the orbits. If the spacecraft does not make any maneuver, after some time it will not have enough energy to maintain itself and orbit and will start an spiral fall. Thus, the drag usually determines the spacecraft's life.

G.2.2 Mathematical Formulation

The spacecraft acceleration due to drag can be expressed by (see [15])

$$\ddot{\mathbf{r}} = -\frac{1}{2} C_D \frac{A}{m} \rho v_r^2 \hat{\mathbf{e}}_v \tag{G.8}$$

where: ρ is the atmospheric density, A, m and v_r are the sparcraft's coss sectional area, mass and velocity relative to the incident flow. The unit vector $\hat{\mathbf{e}}_v$ parallel to the velocity of the incident flow.

It is also usual to rewrite equation G.8 as

$$\ddot{\mathbf{r}} = -\frac{1}{2}\frac{g_0}{B}\rho v_r^2 \hat{\mathbf{e}}_v \tag{G.9}$$

where g_0 is the mean gravity acceleration at sea-level and $B = \frac{W}{C_D A}$ is called the *ballistic coefficient*, with W being the weight of the satellite at sea level.

G.2.3 Discussion about the Parameters

In both equations G.8 and G.9, various parameters are presented. It is important, therefore, to explain their definitions and a basic introduction of how to measure them. The values of these parameters used in this work are given in the section 5 where the results are presented.

The parameter C_D is called the *drag coefficient*. It depends on the shape of the spacecraft, its attitude with respect to the velocity vector and whether it is spinning, tumbling or stabilized [15]. It also depends on the flow conditions which are determined by the Mach (M_α) and Reynolds (R_e) numbers. For the cases studied in this work, the spacecraft never reaches very low altitudes and it not excessively big, thus the flow condition can be considered always a *free molecular flow* which corresponds to $M_\alpha/R_e > 3$ [6].

In this kind of flow, the incident flow is undisturbed by the body moving inside it, and the particles which hit the satellite are re-emitted [19]. Theory provides closed form solutions for simple bodies inside this kind of flow [6], particular for a sphere $C_D = 2.2$ and for a cylinder $C_D = 3.0$ [5]. For simplified analysis usually one value between these ones are used. Precise determinations are usually only obtained by means of flight tests.

The value of A, spacecraft's cross sectional area, depends on its attitude. For Earth satellites, it can be assumed constant with the satellite's main axis of inertia being permanently aligned with the radial direction vector [15].

The relative velocity v_r also depends on the complex atmospheric dynamics. There are some wind models for high altitudes such as the HWM-93 which is recommended by ESA [6] and available at NASA model webpage [20]. However, a reasonable approximation is to assume that the atmosphere co-rotates with the Earth [15]. Thus

$$\mathbf{v_r} = \mathbf{v} - \omega_\oplus \times \mathbf{r} \tag{G.10}$$

where $\mathbf{v}$ and $\mathbf{r}$ are the inertial satellite's velocity and position respectively.

The use of the ballistic coefficient B provides a way of representing all satellite dependent parameters in only one. The greater is in its value, the lesser the object will be slowed by the atmosphere [5].

G.2.4 Density Variation

Although the equation G.8 presents several terms like A and C_D that are difficult to estimate accurately, the most difficult part is to estimate the value of the atmospheric density ρ at a specific point. Modeling the Earth's atmosphere, particular at high altitudes is a challenging task for precise orbit determination.

The difficult arises from the several factors that modifies the atmosphere characteristics. The most important of them are listed below [15]:

Distribuition of chemical constituents at low altitudes (below 100km), the air is a turbulent mixing of gases (homosphere). However, for high altitudes the constituents proportions change widely and diffusion leads to an inhomogeneous species distribution in heterosphere. Therefore, this must be taken into account.

Model of the temperature the atmosphere is divided in several regions according to the temperature profile in them. At small altitudes there are three regions: *troposphere*, *stratosphere* and *mesosphere* where the temperature starts at sea level with a value of $290K$ and first decreases with increasing height. A local minimum of $218K$ is reached at the tropopause at 17km and then the temperature increases with altitude until $50km$ where it reaches a local maximum due to the ozone layer. From there it decreases again with altitude reaching $180K$ at $90km$ in the transition to the *thermosphere*. In this region the temperature suffers a rapid increase and attains an asymptotic limit T_∞ (*thermopheric temperature*) at altitudes between 450 and 600km, where the *exosphere* begins. There on, the temperature does not depend on the altitude but of several other factors. T_∞ values can vary from $600K$ to $2000K$ [6].

Solar radiation the sun is responsible for three main effects in atmosphere. The *day-night effect* is due to solar ultra-violet heating at the day regions of the Earth and depends on the latitude. The second effect comes from the extreme ultra-violet radiation which varies with the sun rotation with a period of 27 days. Finally the third effect is due to the corposcular sun wind. Usually the solar flux is measured by the $10.7cm$ radio flux ($F_{10,7}$) which have units of $[Wm^{-2}Hz^{-1}$.

Geomagnetic storms usually affects the thermosphere by promoting chemical composition changes on a timescale of one or two days. The basic physical processes associated are still not known. They are modeled by two parameters: the *three-hourly planetary geomagnetic index* K_p and the *three-hourly planetary index* a_p. Both are related and are measured with magnetometers.

Semi-annual variations which are characterized by strong height dependence and periodic variations throughout the year, and which geophysical mechanisms are not known;

Latitude density variations which are observed in thermosphere and have a seasonal variation;

Seasonal latitude variations of the He density which are related to the helium migration towards the poles.

G.2.5 Atmospheric Models

Numerous models for the atmosphere have been developed since late 1950s [5]. Maybe the most popular are the ones developed by L.G.Jacchia in the years 1965, 1970, 1971, 1977 and 1981 [15].

Montenbruck present in his book [15] the coefficients of the Jacchia 1971 model, and the Harris-Priester model, which is a simpler one that neglects the temporal and spatial variations of the atmosphere.

ESA standard recommend the use of the MSISE90 model due to ”the large underlying set of supporting measurement data, the large temporal and spatial distribution of these data, the good fit of these data, and the flexible mathematical formulation of the model” [6]. The same model is available at NASA model web page [20].

Due to the easiness of using the subroutine provided by NASA with the MSISE90 model, it was chosen to be used in this work.

G.2.6 Implementation and Validation

As explained in section G.2.5, NASA makes available in its models web page [20] a complete subroutine written in Fortran code that evaluates the MSISE90 atmospheric model. Although

numerous options and outputs are available in this routine, it was decided to execute it with the default options and using only the atmospheric density output.

In order to drive the subroutine and integrate it with the other functions, a C-code function was written. It is able to receive the position of the spacecraft in a ”quasi-inertial” geocentric reference frame, calculate all necessary parameters for the NASA subroutine, call this subroutine, and, with its outputs, calculate the atmospheric drag acceleration of the spacecraft.

The relative velocity calculation is made using the hypotesis of atmosphere stopped in relation to the ground, i.e., the hypotesis considered by Montenbruck's as explained in section G.2.5. This decision was made since the use of a complex wind model was not considered necessary in the case of this work.

The solar and geomagnetic flux indexes used by the NASA subroutine were set, in the driver function, to be the average ones for an average sun activity, as NASA recommends in the commentaries of the subroutine.

In order to validate the atmospheric model, several tests were made. The first had the objective of testing if the calculation of the geodetic longitude, latitude and altitude, which is done inside the driver function was correct. This was made using the GDB debugger program to watch the value of variables meanwhile the program was running and comparing the results with the ones provided in exercise 5.3 of reference [15].

The second test was done comparing the results of density calculated with the driver function with other ones. To compare the data, it was used the table 14 of reference [6] which provide the atmospheric density for mean sun activity. As explained in the reference, the data of this table was calculated with an average of latitude and daily density variations.

Another function was written to call the atmospheric driver function and test its results. This function was set to calculate the atmospheric density profile near Barcelona ($41^o18'$ N $2^o06'$ E [25]) and in three different UT1 hours. Since Barcelona longitude is very near to the Greenwich Meridian, it's local sun hour is close to the UT1 hour.

The result of this comparison is presented in figure G.3. It can be observed that the data closely agrees when the ESA's results are averaged by latitude and daily variations.

The last test was to compare the main decrease of the semi-major axis of a circular orbit obtained by the integration of functions against the known analytical results. According to

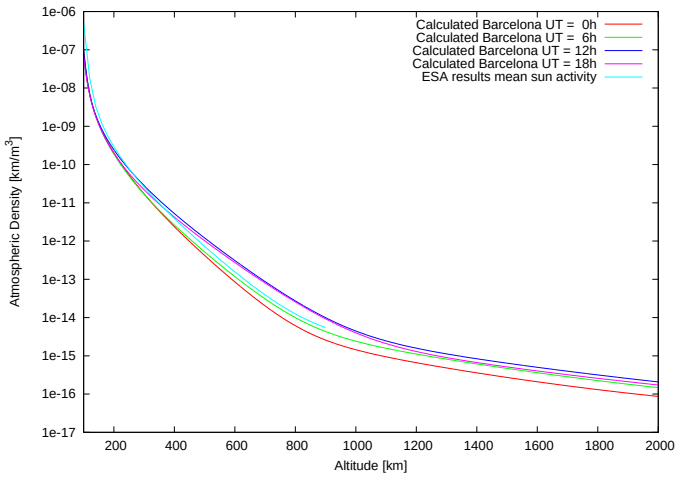

Figure G.3: Comparison between the results of atmospheric density of the written function and the ESA results from reference [6].

reference [5] it can be approximated by

$$\frac{da}{dt} = -\sqrt{GM_{\oplus}}\left(\frac{\rho g_0}{B}\right) \tag{G.11}$$

This equation, however, considers that the satellite relative velocity with respect to the atmosphere is equal to its velocity with respect to an inertial frame. This is not the hypotesis assumed to write the driver function. Nevertheless, the results were compared to check if any big difference would be noted. Table G.2 present the results of this comparison for the same ISS LEO orbit whose parameters are given in table G.1 and a ballistic coefficient of value $1Nm^{-2}$. No great difference between the values was observed.

Table G.2: Values of semi-major axis decreasing rate in meters / day.

Integration	Analytical
-217.447	-225.556

G.3 Solar Radiation Pressure

G.3.1 Introduction

The sun continuously emits light which is a form of radiation. The effects of this radiation has been studied for many years being the first studies conducted by Poynting in 1920 [5]. Robertson lately refined this study including relativistic corrections.

Physically, the photons emitted by the sun collide with the spacecraft surface changing its momentum. Nowadays, the influence of this impinging photon momentum or radiation pressure on a space vehicle is known as Poyting-Robertson force.

G.3.2 Mathematical Formulation

The solar flux Φ is defined as the energy ΔE that passes through an area A in a time interval Δt. Mathematically,

$$\Delta\Phi = \frac{\Delta E}{A\Delta t} \tag{G.12}$$

A single photon impulse p_ν can be expressed by

$$p_\nu = \frac{E_\nu}{c} \tag{G.13}$$

where E_ν is its energy and c is the velocity of light.

Thus, the total impulse change of an absorbing body that is illuminated by the Sun, and the equivalent force F experienced by it, can be expressed as

$$\Delta p = \frac{\Delta E}{c} = \frac{\Phi}{c} A\Delta t \Rightarrow F = \frac{\Delta p}{\Delta t} = \frac{\Phi}{c} A \tag{G.14}$$

From this expression comes the concept of solar radiation pressure P

$$P = \frac{F}{A} = \frac{\Phi}{c}. \tag{G.15}$$

It can be noted that its value does not depend on any spacecraft parameter if we assumes that it absorbs all photons. In a distance of $1AU$ from the sun, i.e., near the Earth, it assumes an average value of: $P_\odot \approx 4.56 \cdot 10^{-6}[Nm^{-2}]$.

It should be kept in mind that this pressure is derived for an area perpendicular to the solar radiation. If this is not the case, the area in equation G.14 should be replaced by $A\cos\theta$, where θ is the angle between the area normal vector $\hat{n}$ and the radiation incidence vector $\hat{e}_\odot$, i.e., $\cos\theta = \hat{n}^T \cdot \hat{e}_\odot$.

Moreover, considering now a more general case, in which the body absorbs only a fraction ε of the energy, the resulting force can be expressed by [15]

$$\mathbf{F} = -AP_\odot \cos\theta \left[(1-\varepsilon)\hat{e}_\odot + 2\varepsilon\cos\theta\hat{n}\right] \tag{G.16}$$

Taking into account the Earth-Sun distance variation due to the eccentricity of the Earth orbit, the resulting spacecraft acceleration can be expressed by

$$\ddot{\mathbf{r}} = -P_{\odot}\frac{1A_U^2}{r_{\odot}^2}\frac{A^2}{m}\cos\theta\left[(1-\varepsilon)\hat{e}_{\odot} + 2\varepsilon\cos\theta\hat{n}\right] \tag{G.17}$$

where $r_{\odot}$ is the distance between the Earth and sun, and m is the mass of the spacecraft.

The determination of each spacecraft's surfaces at a given time is a difficult task. Moreover, another important factor has still not been taken into account: the occurrence of eclipses. Therefore, for many applications (e.g. spacecrafts with large solar arrays), the equation G.17 can be replaced by

$$\ddot{\mathbf{r}} = -\nu P_{\odot}C_R\frac{A}{m}\frac{\mathbf{r}_{\odot}}{r_{\odot}^3}A_U^2 \tag{G.18}$$

where $C_R = 1+\varepsilon$ is called the radiation pressure coefficient, and ν is a parameter that depends on the eclipse conditions and varies from 0 to 1.

G.3.3 Eclipse conditions

Most of near Earth spacecraft, when passing in the night side of the Earth, do not receive full solar illumination since the Sun light is blocked by the Earth, this is called eclipse condition. The eclipse can be partial, total or annular and can happens also when the spacecraft enters the Moon's shadow. Nevertheless, these are less frequent and happens in a "random" fashion [15].

The eclipse condition can be calculated by a simple method considering conical shadows and neglecting the atmosphere and the oblateness of the Earth. The method is presented in details in reference [15].

All the deduction will be based in the representation of figure G.4. We consider $\mathbf{r}_{\odot}$ and $\mathbf{r}$ the position of the Sun and the spacecraft with respect to the Earth respectively. Moreover, $s_{\odot} = ||\mathbf{r}_{\odot}||$ and $s = ||\mathbf{r}||$.

It can be seen in figure G.4 that two shadow cones are formatted, the external one will be referenced as cone 1 and the internal as cone 2. Both of them have the same axis which has the same direction as $\mathbf{r}_{\odot}$.

Defining the spacecraft plane as the plane normal to the vector $\mathbf{r}_{\odot}$, its distance from the the center of the Earth in an anti-Sun direction can be calculated by $s_0 = (\mathbf{s}\cdot\mathbf{s}_{\odot})/s_{\odot}$.

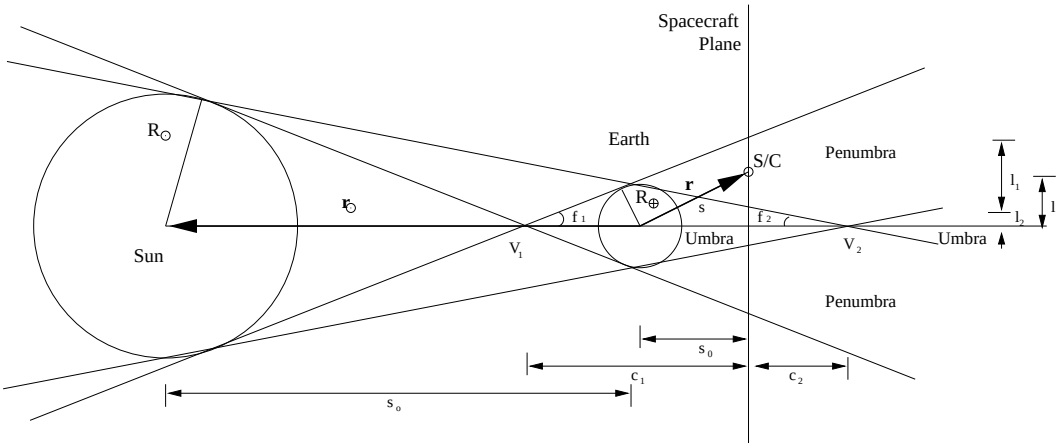

Figure G.4: Eclipse condition geometry

Also, the distance between the spacecraft and the shadow axis l can be expressed by:

$$l = \sqrt{s^2 - s_0^2} \tag{G.19}$$

The angle axis of the cones are calculated by

$$\sin f_1 = (R_\odot + R_\oplus)/s_\odot \approx 0.269^o \quad \text{and} \quad \sin f_2 = (R_\odot - R_\oplus)/s_\odot \approx 0.264^o \tag{G.20}$$

The distances of the fundamental plane to the vertices of the shadow cone V_1 and V_2, measured in an anti-sun direction, are given given by

$$c_1 = s_o + R_\odot/\sin f_1 \quad \text{and} \quad c_2 = s_o - R_\odot/\sin f_1 \tag{G.21}$$

Finally, the radii of the shadow cones in the spacecraft plane can be expressed by

$$l_1 = c_1 \tan f_1 \quad \text{and} \quad l_2 = c_2 \tan f_2 \tag{G.22}$$

The spacecraft can be in two different shadow zones

Penumbra the zone inside the cone 1 and outside the cone 2. In this position the spacecraft is in a partial eclipse condition, which will be discussed later;

Umbra the zone inside the cone 2. If the spacecraft is between the Earth and the vertex V_2 then it receives no solar illumination (total eclipse). Otherwise, it is in an annular condition of eclipse;

These regions, however, only appear after the contact of the cones with the Earth. More precisely, it can be deduced from figure G.4 that the Penumbra starts when $s_0 > -R_\oplus \sin f_1$ and the Umbra when $s_0 > R_\oplus$.

Considering all discussed until now, the table G.3 summarizes the eclipse conditions

Table G.3: Summary of the Eclipse Conditions

$s_0 < -R_\oplus \sin f_1$	$\forall l$	Full illumination (no eclipse)	$\nu = 1.0$
$s_0 > -R_\oplus \sin f_1$	$l > l_1$	Full illumination (no eclipse)	$\nu = 1.0$
$-R_\oplus \sin f_1 < s_0 < R_\oplus \sin f_2$	$l < l_1$	Penumbra (partial eclipse)	$0.0 < \nu < 1.0$
$s_0 > R_\oplus \sin f_2$	$l_1 < l < \lvert l_2 \rvert$	Penumbra (partial eclipse)	$0.0 < \nu < 1.0$
$s_0 > R_\oplus \sin f_2$	$l < \lvert l_2 \rvert$ and $l_2 < 0$	Umbra (total eclipse)	$\nu = 0.0$
$s_0 > R_\oplus \sin f_2$	$l < \lvert l_2 \rvert$ and $l_2 > 0$	Umbra (annular eclipse)	$0.0 < \nu < 1.0$

Thus, the value of ν in the cases of partial or annular eclipse must be determined. First we consider the case of a partial eclipse. The apparent diameter of the two main bodies for the spacecraft is illustrated in figure G.5.

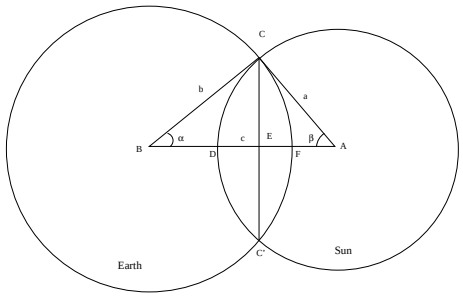

Figure G.5: Partial eclipse geometry

The apparent radii of the sun a and Earth b and given by

$$a = \arcsin \frac{R_\odot}{|\mathbf{r}_\odot - \mathbf{r}|} \quad \text{and} \quad b = \arcsin \frac{R_\oplus}{s} \tag{G.23}$$

and the apparent separation of their centers is expressed by

$$c = \arccos \frac{-\mathbf{s} \cdot (\mathbf{r}_\odot - \mathbf{r})}{s\,|\mathbf{r}_\odot - \mathbf{r}|} \tag{G.24}$$

Thus, the area of the occult segment A_o of the apparent solar disk is equal to the sum of the two section areas

$$A_o = A_{CFC'} + A_{CDC'} \tag{G.25}$$

After some mathematical development summarized in reference [15] this area can be ex-

pressed by

$$A_o = a^2 \arccos\frac{x}{a} + b^2 \arccos\frac{c-a}{b} - cy \tag{G.26}$$

where

$$x = \frac{c^2 + a^2 - b^2}{2c} \quad \text{and} \quad y = \sqrt{a^2 - x^2} \tag{G.27}$$

Finally, the fraction of the sun light in the case of a partial eclipse is given by

$$\nu = 1 - \frac{A_o}{\pi a^2} \tag{G.28}$$

G.3.4 Implementation and Validation

Different from the two other perturbing forces analyzed in this project, the solar radiation pressure does not need coefficients or a complex model, therefore the computer routine to calculate it was fully developed.

In order to determine the position of the Sun with respect to the Earth a small subroutine was written using the low precision method described by Montenbruck (see [15]), that have an accuracy to about 0.1-1%, more then enough for our work.

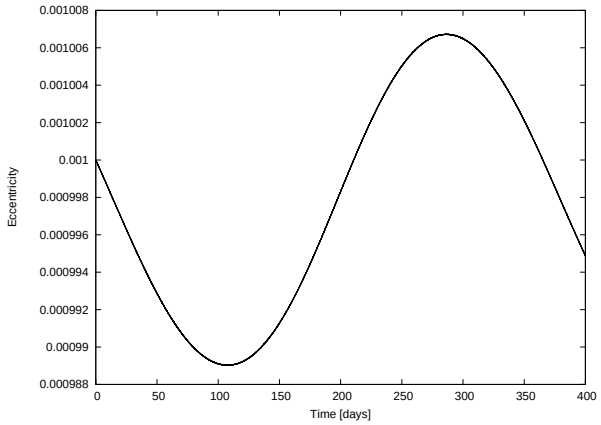

Figure G.6: Example of eccentricity oscillation due to the solar radiation pressure, computed with the written routine.

The main routine was written following exactly the previous discussions. Even the eclipse condition of penumbra was considered, even almost never used in the case of a near Earth orbiting spacecraft.

Validation of the routine was a little less precise as the others. First the eclipse conditions was tested calculating the value of its parameter for a large region around the Earth for different

dates in an year. Although there was no other data to compare, this was useful to determine if a strong mistake could have been done in the development of the routines.

After this step, some orbits LEO orbits were simulated only with the solar radiation pressure perturbation. The idea was to verify the long term oscillation in eccentricity of the orbit. This oscillation can even be compared with analytic previsions described in reference [5]. However, this was not done since the analytic procedures are somewhat complex and time spending.

Figure G.6 shows a result of this tests. As it can be seen, a long term oscillation, with a period of one year is observed, just like it was expected.

H Environment Impact and Project Costs

H.1 Environment Impact

The hole project deals with a mission which already starts in the orbit of the Earth and goes further. Thus, in a first analysis, it would have little or none influence in the Earth environment. However, some points may be discussed about it.

When talking of space mission, one of the major concerns about environment impact is the space debris. Each launch can represent hundreds of small size parts of the spacecraft released in the Earth orbit, and few big ones such as fuel tanks. This debris is potentially dangerous for other missions in case of a huge relative velocity between them. Thus, efforts aiming to minimize the space debris impact are always welcome.

Thinking about the thruster, the actual use of inert gases such as xenon as propellant represents a great advance in the environmental impact when compared with the mercury of the first generation of thrusters.

Finally, in the case of nuclear power generation, an important study must be conducted to determine the risks associated with a possible fail at the launch. Moreover, another study must be performed considering a fail during the mission that could make the spacecraft re-entry in the Earth atmosphere.

H.2 Costs of the Project

The costs of this project is basically composed of the work hours dedicated by the student. This is because the only equipment used was a personal computer with free-source software. Although some of the calculations were done with the help of the cluster of the Departament de Matematica Aplicada I, they were few and only used to save time.

This project was the main objective of the student in its practice time in the university, and it can be considered to be working with exclusive dedication, that is 8 hours of work per day.

The project was developed between January and July. Considering the holidays and few days exceptions without work, we can estimate the total of days in 125, i.e., 25 weeks. The cost of the work per hours was based in other PFC and averaged as 10€/hour. Thus, we have a total project cost of 10000€.